The Pennsylvania State University

The Graduate School

TEMPERATURE AND pH EFFECT ON THE CONTACT ANGLE IN QUARTZ/ WATER/N - DECANE SYSTEM

A Thesis in

Energy and Mineral Engineering

by

Jiaxi Li

Submitted in Partial Fulfillment
of the Requirements
for the Degree of

Master of Science

December 2021

The thesis of Jiaxi Li was reviewed and approved by the following:

Mort D. Webster

Professor of Energy Engineering
Co-Director Initiative for Sustainable Electric Power Systems
Associate Department Head for Graduate Education

Serguei N. Lvov

Professor of Energy and Mineral Engineering & Materials Science and Engineering
Thesis Advisor

Randy L. Vander Wal

Professor of Energy and Mineral Engineering, Materials Science and Engineering, and Mechanical Engineering

Arash Dahi Taleghani

Associate Professor of Petroleum and Natural Gas Engineering
Dr. Charles H. Bowman and Lynn A. Holleran Early Career Professorship in Petroleum and Natural Gas Engineering

ABSTRACT

We have developed a capillary-based system that is able to measure the contact angle in a quartz/water/n-decane system at different temperatures up to 200 ℃ in a pH range of 2-12 under elevated pressures up to 69 bar. Wettability of the reservoir rock is correlated to oil recovery and contact angle in a three-phase system, and the contact angle is an important scale of the system wettability. The obtained data indicate a strong temperature dependence of the contact angle from 25 ℃ to 200 ℃ at the neutral pH (increases 1.1° per +5 ℃). This positive linear trend cannot be sufficiently explained neither by the viscous force influencing the dynamic contact angle nor by the interfacial tension on the water/n-decane interface. Instead, the variation of the interfacial tension on the solid/liquid interfaces should be considered as well. With the increase of temperature, pH of the same solution decreases due to a significant change of the ionization constant of water. The contact angle shows a parabolic trend from the acidic pH to the basic pH at the same temperature, and the maximum contact angle was observed at the isoelectric point of quartz. The pH dependence of the contact angle can be explained via the Zeta potential of quartz, which indicates the degree of electrostatic repulsion between the quartz surface and n-decane. We used a general correlation to empirically describe the contact angle under different temperatures and pH. The isoelectric point obtained from the general equation is in good agreement with data reported in other literature based on the same solid material and method. To verify our experimental results, we employed the surface tension component (STC) method, which divides the surface energy into the polar part and the non-polar part, respectively. The calculated results based on the STC method show a good agreement with our experimentally-measured contact angle. The STC method suggests that the temperature influences both polar and non-polar interactions between quartz and water, while pH only changes the polar interaction.

TABLE OF CONTENTS

LIST OF FIGURES

LIST OF TABLES

Table 5-1-1 DI water/n-decane interfacial tension (γ_{ow}), quartz/DI water contact angle (θ), n-decane viscosity (η_o), and the calculated capillary number (λ_c) at different temperatures. 35

Table 5-2-1 Water properties at the experimental conditions. 39

ACKNOWLEDGEMENT

I sincerely appreciate my advisor, Dr. Serguei N. Lvov. For his consistent guidance, support, and patience during my entire master study. Over the past two years, the insightful feedback from Dr. Lvov stimulated me to sharpen my independent thinking and technical writing that brought my work and methodology to a higher and more organized level.

I must acknowledge Timothy S. Duffy (Tim). It is Tim who brought me to get familiar with the procedures in the lab and help me to deal with the problems in my work. From the font in the figure to the organization of the work, Tim's experiences and suggestions always reminding me to be brief and compelling.

I would like to thank my committee members, Dr. Randy L. Vander Wal and Dr. Arash Dahi Taleghani, for serving on my committee and improving this research.

I want to thank my parents, Yun Li and Fen He, for their unconditional love and wise counsel. Words cannot express how grateful I am. I dedicate this work to you.

I would also like to thank my girlfriend, Wanwei Li, without whom it must be a tough period for me during the pandemic. A decade burst into a blink and I love you as always.

At last, I thank my friend Kwok-Wing (Leslie) Cheung (1956-2003). 'To obsess or to die' always encourages me to get over those obstacles, depressions in lives, to keep self-motivating, and to be a better man.

Chapter 1 Introduction

1.1 Background on Wetting

The wetting phenomenon commonly occurs in daily life, such as when clothes are wetted by water, or when drops of water are standing on a leaf (Fig. 1-1-1). Wetting means that a liquid adheres to or is adsorbed into a solid when the liquid comes into contact with the solid. Wetting is due to the interactions between solid and liquid, which involves two main forces: adhesive force and cohesive force (Sato et al., 2010). Adhesive force is the attraction force between molecules of different substances (e.g. between solid molecules and liquid molecules), which causes a liquid to spread on a solid surface. In contrast, cohesive force is the attraction force between molecules of an identical substance (e.g., between the liquid molecules themselves). Therefore, it is the cohesive force that prevents a liquid from spreading on a solid (Martinez, 2009). Assuming there is a solid/liquid/vapor system (e.g., leaf/water/air system), the competition between the adhesive force and the cohesive force leads to three possible wetting states: completely wetting, partially wetting, and completely non-wetting (Fig. 1-1-2). Completely non-wetting indicates the intrusion of a macroscopic vapor layer between the solid and the liquid. By contrast, a completely wetting state is when there is a macroscopic liquid layer between the solid and the vapor, and the solid and vapor are completely separated. Partial wetting corresponds to drops, surrounded by a microscopically thin film adsorbed on the surface, and completely wetting to a macroscopically thick layer. In a partial wetting state the surface apart from the droplet is never completely non-wetting (Bonn et al., 2009). Given this information, we can use a scale to describe the degree of wetting or non-wetting. This scale is known as wettability.

Fig. 1-1-1. Water drops standing on a leaf (retrieved from fineartamerica.com).

Wettability can be regarded as the tendency of one fluid to spread on or adhere to a solid surface in the presence of other immiscible fluids. Wettability is an important property that relates to the surface free energy and geometric structures of a solid (Gao et al., 2010). The concept of wettability has been widely investigated and applied in different fields, such as electrical engineering (Park et al., 1995; Deng et al., 2019), electrochemical engineering (Xie et al., 2016; Jeon, 2019), biochemical engineering (Wang et al., 2018; Li et al., 2020), agricultural engineering (Stavi et al., 2016), mineral engineering (Faucher et al., 2020), petroleum engineering (Morrow, 1990; Rao et al., 1996).

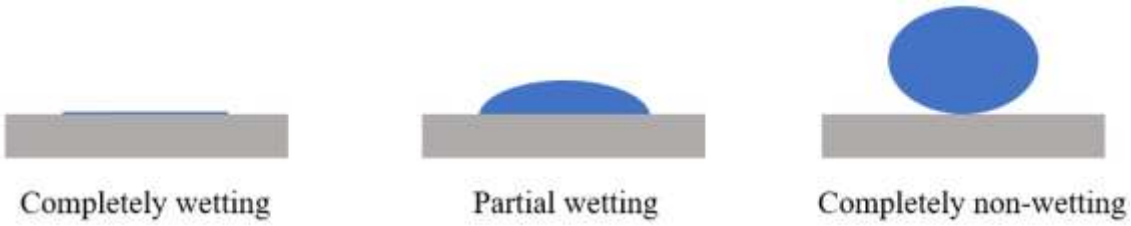

Fig. 1-1-2. Three different wetting states.

In accordance with the different wetting states previously introduced, the particular wettability of a solid material can be categorized as water-wet (hydrophilic), oil-wet (hydrophobic), or intermediate-wet. Over the past few decades, researchers have developed different techniques and methods for evaluating wettability, such as the Amott-Harvey method, the United States Bureau of Mines (USBM) method, the disjoining pressure method, and the surface group method.

In the Amott-Harvey method (Amott, 1959), an oil-saturated sample (e.g., coal) is prepared. Initially, the sample is in its irreducible water saturation. Then, the sample is submerged into the water, and the volume of water imbibed spontaneously, V_{WSI}, can be measured by the volume of oil displaced from the sample due to the spontaneous water imbibition process. When the sample cannot take the spontaneous water imbibition anymore, forced water imbibition is conducted on the sample by an external power. For instance, the sample may be centrifuged in the water. When the forced imbibition is not able to expel any more oil from the sample, the forced water imbibition volume, V_{WFI}, can be recorded. Consequently, the water-wet index (WWI) of the sample can be calculated as:

$$WWI = \frac{V_{WSI}}{V_{WSI}+V_{WFI}}. \quad (1\text{-}1\text{-}1)$$

By preparing the same sample in its irreducible oil saturation and then performing a similar process via oil imbibition, the oil-wet index (OWI) of the sample can be calculated as well. The higher the water-wet index, the more water-wet the system is, and vice versa. The difference between the water index and oil index is called the Amott-Harvey wetting index (AHWI), and the value of AHWI varies from +1 (strongly water-wet) to -1 (strongly oil-wet).

The USBM method was developed by Donaldson et al. (1969). Compared with the Amott-Harvey method, the experimental process is similar. However, a capillary pressure drive is employed for forced displacement in the USBM method. Rather than calculating the volume of the displacement fluid, in the USBM method, the researcher generates a capillary pressure vs. water saturation curve (Fig. 1-1-3). In Figure 1-1-3, the area enclosed by ABCDE in the figure, A_1, and the area enclosed by ABDEF, A_2, are related to wettability by the USBM wettability index:

$$W = \log\frac{A_1}{A_2}. \tag{1-1-2}$$

Similar to AHWI, USBM has a wettability index whose value ranges from +1 (strongly water-wet) to -1 (strongly oil-wet).

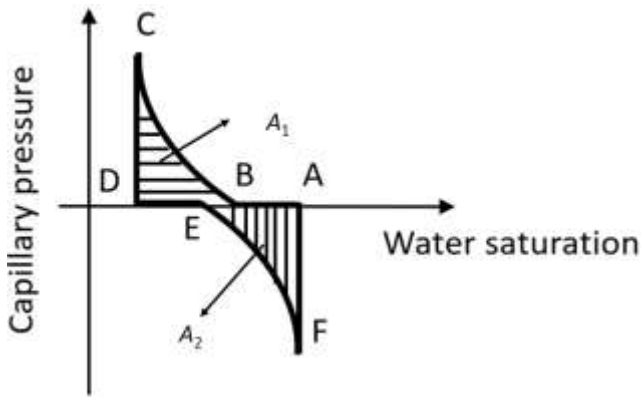

Fig. 1-1-3. Capillary pressure vs. water saturation curve in the USBM method: A-irreducible oil saturation, A→B-spontaneous oil imbibition, B→C-forced oil drive, D-irreducible water saturation, D→E-spontaneous water imbibition, E→F-forced water drive. A_1 is the area enclosed by ABCDE and A_2 is the area enclosed by ABDEF.

The concept of disjoining pressure (Π_{dis}) was introduced by Derjaguin in 1936 (Godin et al., 2012), and it is regarded as the result of Van der Waals forces, the electrostatic forces between the molecules in the system, and the structural forces due to the water molecules associating with the hydrophilic surfaces (Donaldson et al. 2008). As depicted in Fig. 1-1-4, there are 2 independent transition zones at the top and the bottom of the wetting film. If the transition zones do not overlap with each other, a change in the film thickness will not lead to a change in the system free energy. However, if the transition zones overlap, the free energy of the system increases. As a consequence, the equilibrium hydrostatic pressure in the wetting film is different from that in the bulk phase. Disjoining pressure is the difference between these two pressures. Some authors (Butt et al., 2003) have suggested that the disjoining pressure can be calculated as the change in the Gibbs free energy with respect to the film thickness (h) at a constant cross-section area (A), temperature (T), and volume (V), multiplied by -1/A:

$$\Pi_{dis} = -\frac{1}{A}\left(\frac{\partial G}{\partial h}\right)_{A,T,V}. \quad (1\text{-}1\text{-}3)$$

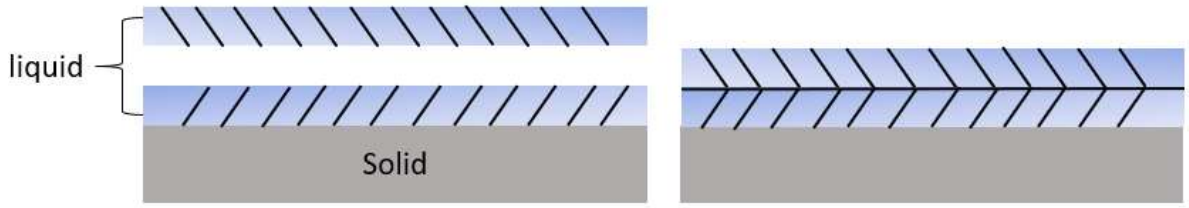

Fig. 1-1-4. The transition zones of the wetting film either do not (left) or do (right) overlap with each other. The hatched area represents the transition zone.

The physical meaning of the disjoining pressure is the force that tends to separate two interfaces (Hlrasakl, 1991). As shown in Fig. 1-1-5, it is believed that there exists a wetting film of liquid between solid material and the meniscus of the bulk phase, assuming the liquid film is the water phase and the bulk phase is the oil phase. Brady et al. (2016) defined such a circumstance as the indirect adsorption of the oil phase on the solid. Therefore, in this case, it is the disjoining pressure that spreads the solid/water interface and the water/oil interface. The Frumkin-Derjaguin equation is used to correlate the wettability and the disjoining pressure (Kondiparty et al., 2011):

$$\Pi_0(h_e)h_e + \int_{h_e}^{inf} \Pi_{dis}(h)dh = S, \quad (1\text{-}1\text{-}4)$$

where Π_0 is the sum of the capillary pressure and the hydrostatic pressure of the oil droplet, h_e is the thickness of the water film at equilibrium, and S is the spreading coefficient, which is related to the wettability of the solid. If S is greater than 0, the in-contact liquid is able to spread on the solid. However, if S is less than 0, the in-contact liquid is not able to spread on the solid.

The results obtained by Wasan et al. (2003) suggested that the thicker the water film, the more water-wet the solid substrate is, and vice versa.

The surface group (or surface complexation) method considers the chemical reactions between the active species in the bulk phase and the functional groups on the solid surface. The wettability of the surface is related to the species when the aforementioned reactions reach their equilibrium. For example, Brady et al. (2016) investigated the wettability alteration (i.e., the process whereby the wettability of a solid surface is changed) of calcite rock in a calcite/brine/oil system by changing the pH value. They studied the bond product of the ion pairs (e.g. $-COO^-$ groups from the oil and $-CaOH_2^+$ groups from the calcite) during pH variation. The bond product is a scale of the degree of electrostatic repulsion between the oil and the solid, and it is given by the summed products of the concentrations of oppositely charged species on oil and mineral surfaces (Brady et al., 2012). Generally speaking, the higher the bond product, the more oppositely charged the species in the system; therefore, the adhesion between the calcite rock and the oil becomes stronger.

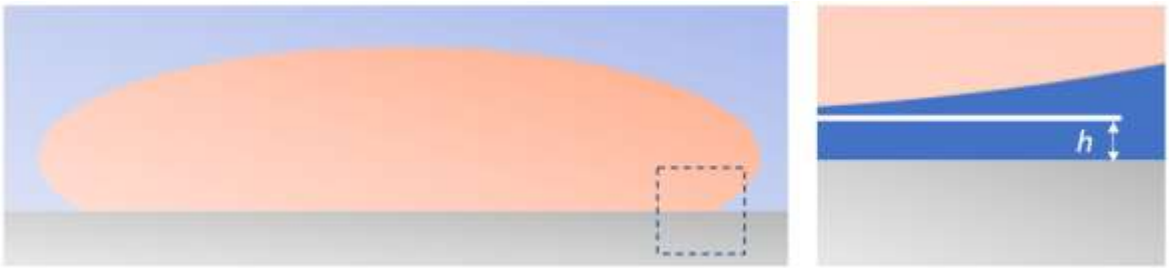

Fig. 1-1-5. The water (blue) film between the oil phase (orange) and the solid substrate (grey). The white line is used as a visual guide for the thickness of the water film.

The surface complexation model can also be employed to predict the alteration of oil recovery (Sanaei et al., 2019). Meanwhile, the impact of salt type (Lager et al. 2008), salt

concentration (Mahani et al., 2018), and pore size (Brady et al., 2016), among other characteristics. can be studied via the surface group method. This method is not limited to calcite surfaces only, however; it is also applicable to sandstone (Korrani et al. 2019), kaolinite (Brady et al. 2012), and silica surfaces (Marmier et al., 1999), to name a few.

1.2 Background on Contact Angle

Along with the evaluation methods introduced in the previous section, the famous Young's model introduced by Thomas Young in 1805 can be used to determine the wettability in a three-phase system. The schematic of Young's model is shown in Fig. 1-2-1. Unlike in the disjoining pressure method, in Young's method, there is no liquid film between the water drop and the solid substrate. Young's equation is given as:

$$\cos\theta_Y = \frac{\gamma_{so}-\gamma_{sw}}{\gamma_{ow}}, \tag{1-2-1}$$

where θ_Y is Young's contact angle (°). γ_{so}, γ_{sw}, and γ_{ow} are the interfacial tensions on the solid/oil, solid/water, and oil/water interfaces, respectively (mN/m).

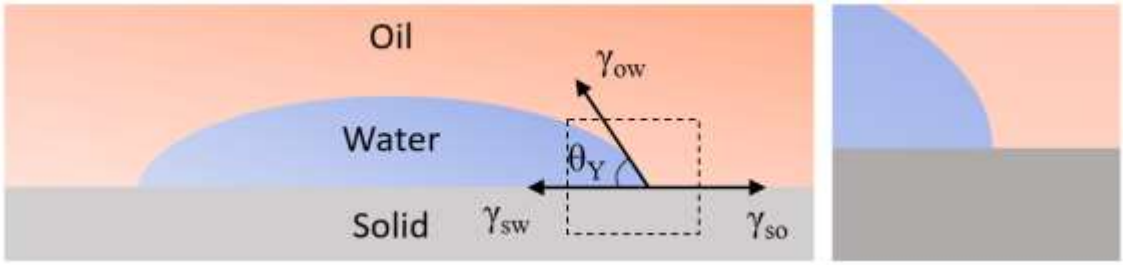

Fig. 1-2-1. Schematic of Young's model. Note the difference at the three-phase contact region with Fig. 1-1-5.

The contact angle is defined as the angle formed through the water (the denser liquid phase) where the water/oil interface meets the solid/water interface (Sonia et al., 2014). In Fig. 1-2-1, it is the angle between γ_{sw} (parallel to the substrate surface) and γ_{ow} (tangent to the contour of the water drop). The contact angle is a common way to describe the wettability of a solid material

(Dwivedi et al., 2017). When the contact angle is zero, the water drop spreads on the solid substrate completely and the solid surface is ultra-hydrophilic (water-wet); when the contact angle is 180°, the water drop is repelled by the solid surface completely and the solid surface is ultra-hydrophobic (oil-wet). According to Treiber et al. (1972), if the contact angle is between 0° and 75°, the surface is considered water-wet; if it is higher than 75° but less than 105°, the surface is regarded as intermediate-wet; when the contact angle is larger than 105°, the surface is oil-wet (Fig. 1-2-2).

The concepts of surface tension and interfacial tension are slightly different. Generally speaking, surface tension exists at the liquid/gas interface, while interfacial tension can exist at the liquid/liquid, solid/liquid, and solid/gas interfaces. At the phase interface, the molecules in the bulk of the phases are surrounded in all directions by the same molecules to which they have an equal attraction. However, those molecules existing at the phase interface are under the impact of adhesive forces from the molecules of the different phase. Meanwhile, they take larger cohesive forces from the molecules of the same phase that are located adjacent to them. Therefore, the molecules at the interface are taking a force that pulls them inward to the direction of their bulk, and surface tension and interfacial tension are the counter-force to maintain the equilibrium (Vander Wal, 2020). A concern regarding Eq. (1-2-1) is that unlike θ_Y and γ_{ow}, γ_{so} and γ_{sw} are not directly measurable (Young, 1805; Briggs et al., 1989). This concern is discussed in the next chapter.

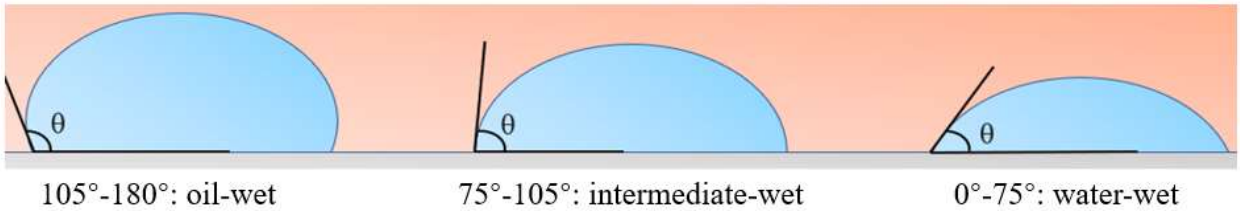

Fig. 1-2-2. Different contact angle values correspond to different wettability values of the solid substrate. The solid substrate is in grey, the water phase is in blue, and the oil phase is in orange.

1.3 Background on Enhanced Oil Recovery

Petroleum engineering became a worldwide significant industry following the oil discovery in 1859 at Oil Creek, PA. Later, the invention of the internal combustion engine and the diesel engine during the second Industrial Revolution expanded the demand for oil. Consequently, oil recovery technology was developed rapidly. In 2020, crude oil production in the United States reached 18.60 million barrels per day, which constituted approximately 20% of the total crude oil

production in the world (Energy Information Administration, 2020). Generally speaking, the crude oil recovery process can be divided into three stages: primary recovery, secondary recovery, and tertiary recovery, the last of which is also called enhanced oil recovery (EOR).

During the first stage of production, the pressure inside the reservoir is sufficient to drive the hydrocarbons out of the pores to the wellbore. Primary recovery is then accomplished by the natural rise of hydrocarbons to the ground surface due to the pressure difference (Thomas, 2007). As oil production progresses, the pressure in the reservoir decays drastically. For example, it has been reported that the pressure inside the Ekofisk oil reservoir in the North Sea dropped from 4,000 psi to near 2,200 psi when the cumulative production was less than 10% of the total original oil in place (OOIP; Lewis et al., 2003). Under such a circumstance, field technicians cannot continue the extraction via primary recovery. Secondary recovery thus begins. During secondary recovery, water is injected into the reservoir to maintain the reservoir pressure and act as a driving agent to displace the oil to the wellbore (Vishnyakov et al., 2020). However, only 30–50% of the total OOIP can be recovered via primary and secondary recovery (Office of Fossil Energy and Carbon Management, 2021) Much of the residual oil is still trapped in the porous media, and the trapped part is difficult to migrate to production wells under the conventional water drive pressure due to capillary force, adhesion effect on the rock surface, and the heterogeneity of reservoir permeability (Arsalan et al., 2015). Nowadays, since most of the easy-to-extract oil has already been recovered from the oil fields, EOR is greatly needed to boost production potential. In studying and applying EOR, scholars and field technicians do not focus on identifying another immiscible fluid to displace and drive the trapped oil. Instead, the wettability of the reservoir is one of the foci of EOR research and application.

In EOR, reservoir wettability can be altered by three different methods: chemical injection, thermal injection, and gas injection. In chemical injection, chemicals such as surfactants are injected into the reservoir. The surfactants are able to penetrate the rock and act as a solvent at the specific temperature and pressure (Pal et al., 2017). For example, sodium dodecyl sulfate (SDS) is a commonly used surfactant in EOR. It is regarded as amphiphilic due to its specific structure. SDS has a polar sulfate head group, which is its functional group, and a non-polar tail that consists of a hydrocarbon chain. As a result, the polar group is hydrophilic while the non-polar group is hydrophobic. Consequently, when SDS is injected into the reservoir, the non-polar groups sweep the oil trapped on the rock surface, and the polar groups ensure that SDS and the swept oil stay in the aqueous phase (i.e., forcing the oil to become the solute). Therefore, the oil recovery is enhanced by enforcing the mobility of the oil (Kamal et al., 2017). However, the usage of surfactants has some limitations: the high temperature and pressure inside the reservoir may hamper the stability of the surfactants (Belhaj et al., 2019), and extra costs might be incurred due

to the adsorption of the surfactants in the reservoir rock (Sandersen, 2012). In addition to surfactant flooding, alkane flooding and low-salinity water flooding (LSWF) are within the range of chemical injection. Chemical injections improve recovery with their high efficiency and causes very damage to the integrity of the recovery system. However, chemical injections are usually hampered by their high costs, environmental risks, and unpredictable effectiveness.

In thermal recovery, the temperature inside the reservoir is altered by the hot steam (such as natural gas) injection to change the wettability of the reservoir. Solar-generated hot steam is often used in thermal recovery, which reduces the energy costs and carbon footprint of the crude oil produced. The drawback of this method is that another hot steam injection well is needed and it is not always economic feasible.

Gas injection accounts for nearly 60% of the total EOR production in the United States (Enhanced Oil Recovery, Energy. gov). Gases such as carbon dioxide and nitrogen are injected into the reservoir; then the oil and the gas are mixed in a random proportion (Lou, 2019). The mixture is in a single phase (i.e., there is no interfacial tension). As a result, the oil saturation of the reservoir is minimized (Teletzke et al., 2005). The injection of gas can lower the viscosity of oil. However, the relative low density and viscosity of CO_2(g) compared to reservoir oil are responsible for gravity tonguing and viscous fingering (Masoud, 2015).

Chapter 2 Literature Review

2.1 Contact Angle Measurement Technique

2.1.1 Sessile Drop Method

The sessile drop method is the most commonly utilized method to measure the contact angle (Yuan et al., 2013). In the sessile drop method, a liquid (e.g., water or oil) drop is metered onto a solid substrate. The surface of such a substrate should be as smooth and homogeneous as possible to ensure the accuracy of the measured results. The sessile drop method can be divided into the drop-profile method, drop-dimension method, and axisymmetric drop shape analysis.

In the drop-profile method, the contact angle is measured by observing the profile (or shape) of the drop directly. Bigelow et al. (1946) projected a test drop on a screen, from which the outline of the drop could be shown. Then, they employed a telescope goniometer to complete the contact angle measurement. The development of the image and photographic technology provides an alternative for the aforementioned projection, the photo of the drop was taken as for the contact angle analysis. Compared with the projection, the accuracy of the measurement is enhanced significantly with the usage of high magnification (i.e. zooming in or out), and the solid/drop contact line and the three-phase contact point on the photograph can be repeatedly reviewed to ensure the reliability of the measurement. Hunter (2001) found that the accuracy of such measurements can be controlled within a ± 2° range for those contact angles greater than 20°. In this method, the contact angle can be measured conveniently using only small amounts of liquid and a small, flat solid surface. However, the measured results are significantly influenced by the impurities on the solid surface; preparing an absolutely clean surface is impossible. Another concern is that the camera focuses on the largest meridian section. In other words, the contact angle is measured on a single base line where the meridian plane meets the contact line. However, the contact line may not be perfectly horizontal due to the surface roughness (Chau, 2009). Therefore, the drop-profile method is regarded as the most convenient method when high accuracy is not needed.

Unlike in the drop-profile method, in the drop-dimension method, the contact angle is not directly measured. Instead, it is calculated from the dimension of the drop. For example, Spitze et al. (1947) measured the height of the drop at equilibrium h and the width of the drop at solid/liquid contact point d. Then they used the following equation to calculate the contact angle:

$$\tan\frac{\theta}{2} = \frac{2h}{d}. \quad (2\text{-}1\text{-}1)$$

While the aforementioned method considers the equilibrium height and width of the drop, another strategy of the drop-dimension method, the axisymmetric drop shape analysis-profile (ADSA-P), fits the famous Young-Laplace equation (Butt et al., 2006) to calculate the contact angle:

$$\gamma\left(\frac{1}{R_1} + \frac{1}{R_2}\right) = \Delta P, \quad (2\text{-}1\text{-}2)$$

where R_1 and R_2 are the principle radii of the curvature (in m), ΔP is the pressure difference between the two sides of the curvature (in Pa), and γ is the interfacial tension on the solid/water interface (in N/m).

2.1.2 Capillary Rise Method

Capillary rise (or capillarity action) is a phenomenon in which the liquid rises or falls spontaneously inside of a narrow path, such as a capillary tube or the pore throat inside of the rock. As shown in Fig. 2-1-1, a meniscus is formed because of the internal cohesion of the substance and the adhesion between the liquid and the solid (Kaliakin, 2017). The curvature of the meniscus can be either positive or negative depending on the properties of the solid and the liquid. Since the phase interface is curved, there must a contact angle between the solid and the liquid, and this is one of the output results of the capillary rise method.

In the capillary rise method, the contact angle can be calculated using the following equation:

$$\cos\theta = \frac{\rho g r}{2\gamma h}, \quad (2\text{-}1\text{-}1)$$

where h is the height of the liquid column at equilibrium (in m), γ is the interfacial tension at the meniscus (in N/m), ρ is the density of the liquid (in kg/m^3), g is the local gravitational acceleration, (in m/s^2), and r is the inner radius of the tube (in m).

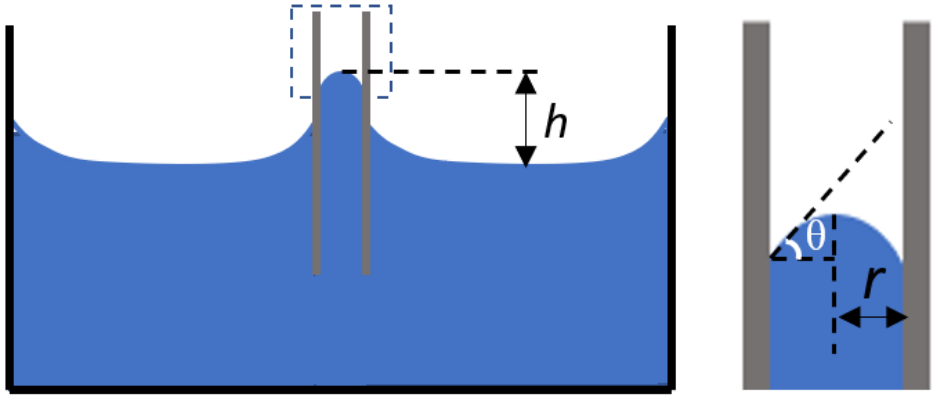

Fig. 2-1-1. Schematic of the capillary rise method. The materials comprising the container and the capillary wall are different.

The capillary-based system is more appropriate than other methods for representing the reservoir wettability (Wei et al., 2018). Compared with the sessile drop method, the capillary rise method outputs the dynamic contact angle, which better reflects the fact that the water/oil interface is advancing in the reservoir (i.e., a dynamic process). The effect of porosity can be studied by changing the dimension of the capillary (Li et al., 2014). The capillary rise method can be adapted to a smaller sample size for measurement since it is hard to deposit drops smaller than 1 mm in the sessile drop method. However, to the best of our knowledge, most of the capillary-based contact angle measurement experiments have been conducted under room conditions. It is necessary to simulate the high-temperature and high-pressure conditions inside the reservoir.

The drawback of the capillary rise method is that it requires a large vessel so that the meniscus formed in the vessel does not interfere with the one formed in the capillary, thereby ensuring the precision of the measured height. Therefore, a large amount of liquid is needed (Mulqueen et al., 2020). In addition, if the curvature of the meniscus is negative (convex), the weight of the liquid above the apex of the meniscus will be ignored in Eq. (2-1-1), while in theory this weight should be considered. Researchers have made some corrections to the method (Liu et al., 2014) to eliminate this flaw. These corrections have made the data treatment more complex.

In porous materials, the direction of the pores (capillaries) may not be solely vertical. The Washburn equation is another approach to calculate the contact angle inside porous media:

$$\cos\theta = \frac{2\eta L^2}{\gamma r t}, \tag{2-1-2}$$

where η is the viscosity of the liquid, and L is the penetration distance of the liquid in the capillary within time, t.

The Washburn equation is another convenient approach to calculate the contact angle inside the capillary. However, it was derived based on the assumption that there is a solid material containing idealized pores in the shape of parallel capillaries, which is a significant simplification compared with the real status of porous materials (Zaccardi et al., 2018). Moreover, the Washburn equation is not suitable for non-Newtonian fluids such as ink and blood.

2.1.3 Wilhelmy Plate Method

The Wilhelmy method, named after German chemist Ludwig Wilhelmy, is another indirect contact angle measurement approach. The schematic of this method is shown in Fig. 2-1-2. A thin plate (e.g., glass, platinum, paper) is vertically placed halfway into the liquid. In this method, both the vertical force that acts on the plate and the dimension of the plate itself need to be confirmed. Then, the contact angle can be calculated by the following equation:

$$\theta = \arccos\left(\frac{F}{l\gamma}\right), \tag{2-1-3}$$

where $l = 2(w + d)$ (in m), F is the vertical force, (in mN), and γ is the surface tension at the water/air interface (in mN/m).

In modern experiments, the movement of the plate is usually controlled by the computer (Tiab et al., 2012). As such, the instantaneous vertical force variation can be detected and the contact angle value can be updated quickly. The plate material does not impact the measured results as long as it can be wetted by the liquid (Butt et al., 2003). The drawback of this method is that a relatively large amount of liquid is needed.

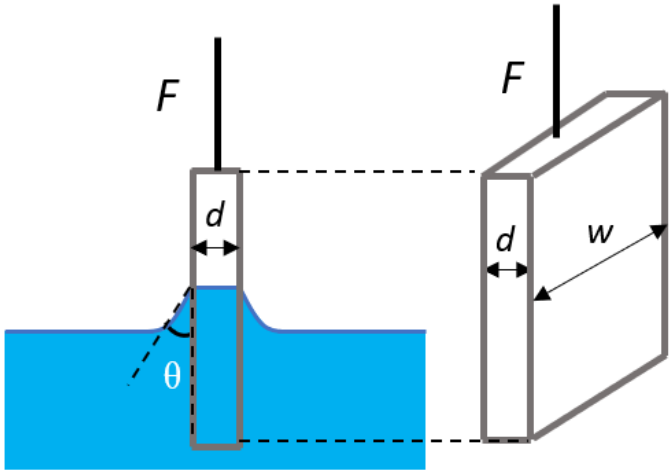

Fig. 2-1-2. Schematic of the Wilhelmy plate method. The external force *F* is acted on the bolded vertical line, and its direction can be either upward or downward.

2.1.4 Microscopy Methods

Some research has focused on determining the contact angle of a small particle (Ducker et al., 1994; Ralston et al., 1999), but the aforementioned methods are not good options for doing this. The development of advanced microscopy techniques such as atomic force microscopy (AFM) has provided solutions to this problem. The interaction forces between the particles and the aqueous solution can be determined with AFM. Then, the values of the contact angle can be obtained after a series of theoretical treatments.

Microscopy methods were not commonly employed for contact angle measurement for the following reasons: Compared with the methods discussed earlier, a complex calculation process was a part of the microscopy methods and there were several assumptions and ambiguities in the calculation and analysis as well as the experimental setup and calibration (Johnson et al., 2006). Nguyen et al. (2003) reported that the three-phase contact point relative to the particle was difficult to determine, and it was likewise hard to determine whether the obtained contact angle could be used as a standard by which to judge the wettability of the surface, as discussed in Section 1.2.

2.2 Contact Angle Theories

2.2.1 Young-Dupre Equation

As we mentioned earlier, γ_{so} and γ_{sw} cannot be directly measured. The Young-Dupre equation provides a solution to this problem. When the solid phase is wetted by the water phase,

the individual phase surfaces that existed previously disappear, and a new interface is formed to separate the two immiscible phases. This process is related to energy change. The work must be done to form the new interface is 'the work of adhesion' (Ebnesajjad et al., 2015). In a solid/water/oil system, the total work of adhesion, W_a, can be obtained using the following equation (Licari et al., 2011):

$$W_a = \gamma_{so} + \gamma_{ow} - \gamma_{sw}. \quad (2\text{-}2\text{-}1)$$

Combining Eq. (2-2-1) and Young's equation (Eq. 1-2-1), the following equation can be obtained:

$$W_a = \gamma_{ow}(1 + \cos\theta_Y). \quad (2\text{-}2\text{-}2)$$

Eq. (2-2-2) is known as the Young-Dupre equation. In this equation, W_a replaces the unmeasurable interfacial tensions. Therefore, the Young-Dupre equation makes it possible to determine the work of adhesion via the available θ_Y and γ_{ow} measurements. In some cases, the work of adhesion can be interpreted as the work required to separate one liquid into two parts.

2.2.2 Surface Tension Component Method

The surface tension component (STC) method is a significant reference in our work. This method was introduced by Oss et al. (2006). In the STC method, the surface tension of a single phase *i*, is divided into two parts:

$$\gamma_i = \gamma_i^{LW} + \gamma_i^{AB}, \quad (2\text{-}2\text{-}3)$$

where the superscript "LW" indicates the Lifshitz-Van der Waals component of the surface tension, which is due to non-polar interactions, including induction force, dipole-dipole force, and dispersion force (Chaudhury, 1984). The superscript "AB" indicates the Lewis acid-base

component of the surface tension, which is due to polar interactions such as hydrogen bonds. Similarly, for the phase interface, the following equation can be written:

$$\gamma_{12} = \gamma_{12}^{\mathrm{LW}} + \gamma_{12}^{\mathrm{AB}}, \tag{2-2-4}$$

where subscripts "1" and "2" are the immiscible phases 1 and 2, respectively.

The Lifshitz-Vander Waals component of surface tension is due entirely to non-polar interactions, which can be calculated by the following equation:

$$\gamma_{12}^{\mathrm{LW}} = (\sqrt{\gamma_1^{\mathrm{LW}}} - \sqrt{\gamma_2^{\mathrm{LW}}})^2 = \gamma_1^{\mathrm{LW}} - \gamma_2^{\mathrm{LW}} + 2\sqrt{\gamma_1^{\mathrm{LW}}\gamma_2^{\mathrm{LW}}}. \tag{2-2-5}$$

The Lewis acid-base component of surface tension is due entirely to polar interactions, which can be obtained with the following equation:

$$\gamma_{12}^{\mathrm{AB}} = 2(\sqrt{\gamma_1^+\gamma_1^-} + \sqrt{\gamma_2^+\gamma_2^-} + \sqrt{\gamma_1^+\gamma_2^-} + \sqrt{\gamma_1^-\gamma_2^+}), \tag{2-2-6}$$

where γ_i^+ is the electron-acceptor component of γ_i, and γ_i^- is the electron-donator component of γ_i. For non-polar substances, both γ_i^+ and γ_i^- are 0; for dipolar substances, both γ_i^+ and γ_i^- are not 0; and for monopolar substances, γ_i^+ or γ_i^- is 0 (Oss, 1993).

Generally speaking, γ_i^{LW} can be theoretically calculated. However, based on our literature review, no theory has been introduced to calculate γ_i^{AB}. As a result, it is treated like an empirical constant that depends on the solvent chemistry, temperature, pH, among other characteristics. A more detailed discussion of the STC method is provided in Chapter 7.

2.3 Effects of Surface Roughness and Heterogeneity on Contact Angle

Young's equation is based on the assumption that the surface is absolutely flat, smooth and homogeneous. However, this kind of ideal surface does not exist. The influences of surface

roughness and heterogeneity on the macroscopic contact angle measurement are addressed in this section (Hebbar et al., 2017). We introduce a phenomenon that occurs for the aforementioned reasons and present two contact angle models considering the effects of surface roughness and heterogeneity.

2.3.1 Contact Angle Hysteresis

If we take a look at raindrops on a window on a rainy day, we may find that they stick to the window surface despite the fact that the window is oriented vertically. Meanwhile, the shape of the raindrops is inclined to the ground. This is due to contact angle hysteresis (CAH), which keeps the droplets in place even as gravity pulls the droplets downward (Eral et al., 2013). Fig. 2-3-1 shows CAH on a titling surface. CAH refers to the phenomenon in which there is a difference between the advancing contact angle (θ_A) and the receding contact angle (θ_R). CAH can be attributed to surface defects (i.e., the surface not ideally smooth and flat) and a possible difference in the surface chemical composition. Butt et al. (2006) reported that this possible difference is usually from 5° to 20°. From the point of view of thermodynamics, CAH reflects the activation energy required for shifting a drop from one metastable state to another (Gao et al., 2006). In recent years, CAH has played a role in different industrial applications such as ink-jet printing (Krainer et al., 2020).

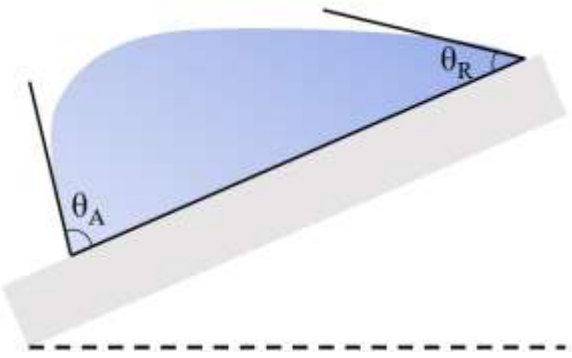

Fig. 2-3-1. Schematic of contact angle hysteresis on a titling surface.

2.3.2 Wenzel Contact Angle

To account for the effect of surface defects, Wenzel (1936) proposed the concept of the 'roughness factor' to modify Young's equation. He assumed that the actual surface area of a solid

surface is increased because of surface roughness, and surface roughness increases the actual solid-liquid contact area. As a result, the interfacial tension at the solid/liquid and solid/oil interfaces is changed. Consequently, a different apparent contact angle (i.e., the contact angle obtained based on a real surface) can be observed.

As shown in Fig. 2-3-2, one important assumption of Wenzel's model is that the liquid can penetrate the roughness grooves completely. Then, the Wenzel equation can be written as:

$$\gamma_{ow} \cos \theta_W = \Upsilon(\gamma_{so} - \gamma_{sw}), \tag{2-3-1}$$

where θ_W is the Wenzel contact angle and Υ is the roughness factor of the solid surface, which refers to the ratio of the actual solid-liquid contact area and the apparent (geometric) solid-liquid contact area of the surface.

Combining Young's equation and the Wenzel equation, we have:

$$\cos \theta_W = \Upsilon \frac{(\gamma_{so} - \gamma_{sw})}{\gamma_{ow}} = \Upsilon \cos \theta_Y. \tag{2-3-2}$$

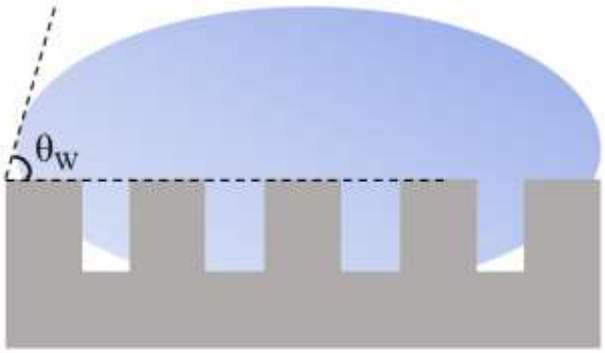

Fig. 2-3-2. Schematic of Wenzel contact angle. The white part represents air.

The preceding equation indicates that the value of $\cos \theta_W$ is positively related to roughness (Υ) when the intrinsic contact angle, which is obtained based on an ideal surface, θ_Y, is less than 90°. In other words, an increase in the surface roughness will cause the water-wet surface to become more water-wet. Similarly, when θ_Y is greater than 90°, the surface roughness increases,

and the oil-wet surface becomes more oil-wet. However, there are some inconsistencies between this predictive trend and the experimental results reported in the literature (Morrow, 1975). In addition, according to Eq. (2-3-2) there is only a single apparent contact angle value that corresponds to a roughness factor. If the surface is composed of different kinds of materials and different roughness structures, such as grains of sand with different amounts of space between them, it might be hard to determine the value of Υ, and the 1-1 map between Υ and θ_W may not be guaranteed.

2.3.3 Cassie-Baxter Contact Angle

As we mentioned earlier, the Wenzel model is not applicable to chemical-heterogeneous surfaces. To solve this problem, Cassie and Baxter (1944) developed a new approach. They came up with the concept of 'complex contact' to describe the wetting condition of a drop on a heterogeneous surface. As shown in Fig. 2-3-3, the Cassie-Baxter contact angle is obtained based on the assumption that the liquid will not leak into the grooves and some air exists in the grooves. Therefore, most of the liquid will be directly in contact with the solid surface while the other parts will be in contact with the air. The Cassie-Baxter (CB) equation for this condition is given as:

$$\cos\theta_{CB} = f_s \cos\theta_s + f_a \cos\theta_a, \tag{2-3-3}$$

where θ_{CB} is the Cassie-Baxter contact angle, θ_s and θ_a are the intrinsic contact angle for the solid-liquid-air and liquid-air-air interface, respectively, and f_s and f_a are the fractions of the liquid-solid interface and the liquid-air interfaces, respectively (f_s+f_a=1).

If θ_a is taken to be 180° by assuming the liquid is a perfect sphere when the air is in contact with the liquid, then the CB equation can be rewritten as:

$$\cos\theta_{CB} = f_s(\cos\theta_s + 1) - 1. \tag{2-3-4}$$

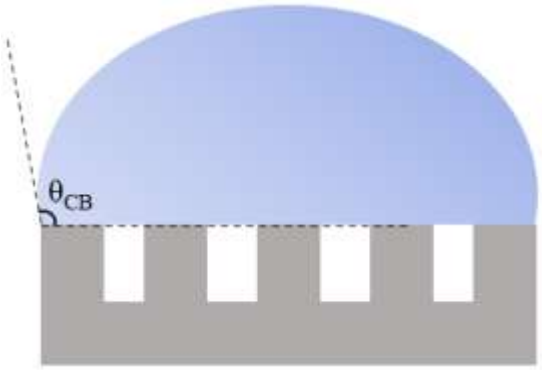

Fig. 2-3-3. Schematic of Cassie-Baxter contact angle. The white part represents air.

It can be predicted from Eq. (2-3-4) that with the increase of the solid-liquid surface area fration (f_s), a higher $\cos\theta_C$ value can be obtained. Hence a smaller θ_C value can be calculated, and the surface becomes more water-wet. If so, the apparent contact angle should be increased with the increase of the water/solid contact area. However, a direct challenge to the CB equation has been presented by Gao et al. (2007). In their experiments, they prepared different materials in various topographies. Then, they experimentally measured the contact angle by setting f_a in Eq. (2-3-3) to 0. The obtained θ_{CB} was used for theoretical calculation according to CB's model by changing the values of f_s and f_a. Simultaneously, they measured the contact angle under different f_s and f_a by changing the dimensions of the solid material. Unfortunately, they found significant discrepancies between the experimental results and the calculated results when using the same f_s and f_a values. Therefore, they argued that the contact angle is not determined by the solid-liquid surface area. Instead, the interactions on the three-phase contact line beneath the droplet and the structure of the contact line are essential for determining the contact angle. This point of view has been supported by other papers (McHale, 2007; Seo et al., 2015). In addition, it was suggested that the CB equation is only applicable to those liquid droplets that are sufficiently large compared with the surface roughness (i.e., grooves on the surface); the size of the drops should be around 3 orders greater than the dimensions of the roughness (Carmeliet et al., 2017).

2.4 Effect of Wettability on Oil Recovery

The wettability of a reservoir is described by complex interactions between the solid (i.e., reservoir rock) and the liquids (i.e., water, brine, crude oil) within the pore scale of porous media. These interactions determine the efficiency of displacement of the oil in the reservoir (Morrow, 1990). As a result, wettability impacts oil recovery.

It might seem intuitive that a strong water-wet reservoir is associated with strong capillary imbibition forces, which give the most efficient oil displacement (Agbalaka, 2008). Kulinič (2015) assumed that a much greater oil recovery is reached in a hydrophilic reservoir than in a hydrophobic reservoir when water is injected into the reservoir to displace the oil. For hydrophilic rocks, oil is displaced as the front of the waterfloods. For hydrophobic rocks, waterfloods can only penetrate a narrow path for themselves, while a significant amount of oil is not displaced (Fig. 2-4-1). However, Falode et al. (2014) tested the oil permeability of a sample that contained quartz and carbonate under different wettability. Their results showed that the relative permeability of the crude oil increased from 0.29 to 0.56 when the sample changed from water-wet to oil-wet. Tje higher the relative permeability of oil, the better the conditions for oil recovery. Therefore, understanding the correlation between reservoir wettability and oil recovery is significant for altering reservoir wettability in the right direction for optimal recovery that saves time and money.

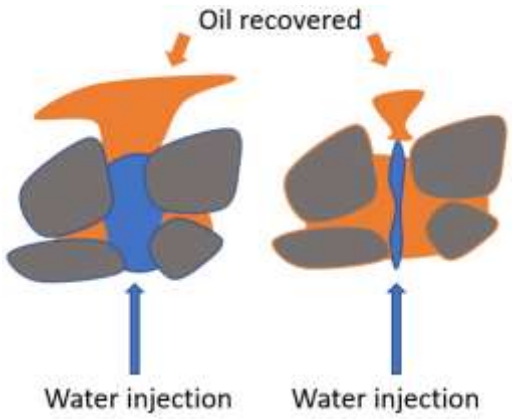

Fig. 2-4-1. Water injection of the hydrophilic rock (left) and hydrophobic rock (right) during secondary recovery. Reproduced based on the opinion of Kulinič (2015).

In recent years, there has been an increasing number of reports suggesting that better oil recovery rate is reached when the reservoir changes from strongly water-wet to intermediate-wet (Agbalaka, 2008). Jadhunandan et al. (1991) conducted several advanced core analyses for wettability (ACAW) based on a sandstone/brine/crude oil system. Their results showed that oil recovery rate by waterflooding is better increased by altering the system from strongly water-wet to weak intermediate-wet, and they reported the optimum recovery at a 0.2 Amott-Harvey wettability index. This point of view is supported by other researchers who conducted their experiments based on various solid materials such as chalk (Graue et al., 1999) and carbonate rock (Skauge et al., 2006).

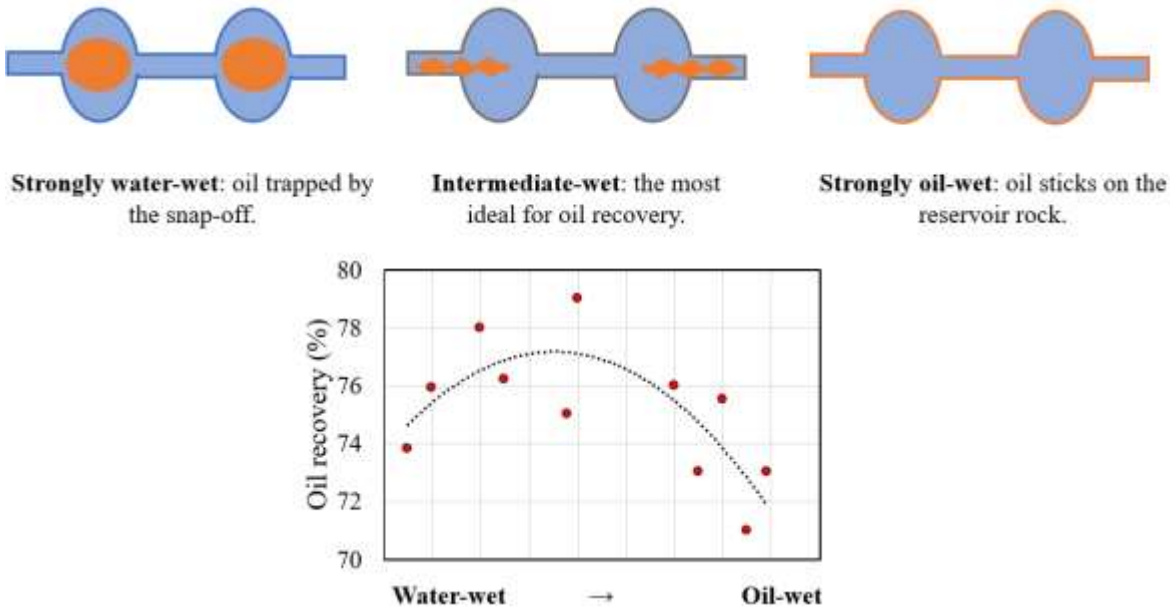

Fig. 2-4-2. Distribution of water and oil in different wetting behaviors of the rock. The oil recovery vs. wettability plot was reproduced based on Fig. 6 from Wang et al. (2011).

The intermediate-wet reservoir is the most preferred for oil recovery. The relationship between oil recovery percentage and reservoir wettability is shown in Fig. 2-4-2. If the system is strongly oil-wet, the oil will be trapped in the small pores on the wall of the reservoir rock, making it difficult for water to drive the oil in these small pores. If the reservoir is strongly water-wet, the water phase forms collars in the pore throat. Then the migration of the oil will be blocked, and the oil will be trapped in the large pores. This phenomenon is called snap-off (Singh et al., 2017). However, if the reservoir is intermediate-wet, no capillary pressure exists on the intermediate-wet surface strata (Jiang, 2018). Therefore, the advancing of the water/oil interface is free from the impact of capillary forces and the non-ideal conditions in strongly water-wet and oil-wet reservoirs. Injected water will flow evenly through both the large and small pores in the reservoir, increasing the sweep efficiency and oil recovery rate.

2.5 Temperature and pH Effect on Wettability

Temperature and pH change reservoir wettability. They are in the range of thermal recovery and chemical injection recovery, respectively. Jadhunandan et al. (1995) reported that the wettability of sandstone changed from strongly water-wet to intermediate-wet when the temperature increased from 26 to 80 °C. The same trend has been reported by other authors

(Sharma et al., 1985; Nasralla et al., 2013). An increase in temperature may improve the mobility of oil by reducing the surface energy at the water/oil interface and lowering the viscosity of the crude oil. However, a reverse wettability alteration trend as the temperature increases has been reported as well (Hjelmeland et al., 1986; Hamouda et al., 2006). The thermal energy may not influence not only the fluid properties and fluid-fluid interactions but also the solid-fluid interactions.

The investigation of the pH effect on reservoir wettability is often conducted via the surface complexation method (Chapter 1). For example, Xie et al. (2018) reported that a calcite rock surface changed from weakly water-wet to strongly oil-wet when the pH was increased from 3 to 8. This shift occurred because the shift in pH causes a corresponding shift in the number and type of functional groups on the phase boundaries (interfaces). The sum of the bond product (Chapter 1) is also varied. Hence, the degree of repulsion between the solid surface and oil surface changes. Al-Rossies et al. (2010) suggested that in addition to affecting functional groups, the increase in pH lowers the interfacial tension at the water/oil interface, thereby improving oil recovery.

A better understanding of the independent effects of temperature and pH is needed. Based on our study, the range of experimental temperatures employed was limited (usually less than 100 ℃). Compared with the available reservoir conditions (Table 2-1), the 100 ℃ limitation prevents us from simulating the actual conditions in a reservoir. Meanwhile, pressure should not be restricted to atmospheric pressure only. There might be some room for investigating how the mechanism of wettability alteration is affected by these external conditions. For example, a more detailed understanding of temperature and pH effects on the solid/fluid, fluid/fluid interactions (e.g. Van der Waals forces, hydrogen bonds) is necessary. In addition, researchers should study the coeffect of temperature and pH so they can provide more practical suggestions to EOR.

The contact angle is the most universal measure of the wettability of surfaces (Morrow, 1990). We can better understand how the wettability of a particular surface is altered if we determine the contact angle dependence based on temperature, pH, and pressure.

Table 2-1 Available reservoir temperature data.

Reservoir	Depth (m)	Temperature (°C)	Reference
Teapot Dome field, US	2130	120	Gong et al. (2011)
Maverick basin, US	3960	160	Erdlac et al. (2007)
Maverick basin, US	5182	224	Erdlac et al. (2007)
Delaware-Val Verde basin, US	7600	220	Erdlac et al. (2007)
Utica play, US	2130–3660	100–200	U.S. Energy Information Administration (2017)
Changji oilfield, China	3000	140	Qin et al. (2018)
Golden Eagle oilfield, UK	2255	170	Pinnock et al. (2020)

Chapter 3 Research Objectives

Based on the previous discussion of the contact angle, wettability, and oil recovery we identify the following main objectives of this study:

1. Conduct experimental studies on contact angle measurement under different external conditions, such as temperature and pH.

In the previous chapters, we have noted that the wettability of the reservoir is related to oil recovery. The reservoir wettability changes the external conditions due to the variation in the interactions at the surface. This process is known as 'wettability alteration.' The contact angle is an experimentally measurable parameter that reflects the wettability of the system. As mentioned in Chapter 2, there is a very limited capillary-based study that investigated contact angle variation under high temperature, high pressure, varied pH values, and a combination of these important parameters. Therefore, the first purpose of the present study is to develop a capillary-based system that is able to measure the contact angle at high temperature and pressure values. The experimental design should likewise be capable of elucidating a window to learn the influence of other changeable parameters (e.g., pH, salt concentration, salt type) on the contact angle. Note that in the experimental system, all these aforementioned parameters can be utilized as a single variable or combined at random.

2. Understand the impact of temperature and pH on quartz wettability.

As mentioned in Chapter 2, the effects of temperature and pH on wettability alteration require more investigation. In this study, we focus on contact angle variation in a quartz capillary/water/n-decane system. The wettability alteration results of the quartz at different temperatures (from 25 to 200 ℃) and pH (from 2–12) can be deduced based on the experimental results. Broader experimental temperature and pH ranges would allow us better replicate actual reservoir and EOR conditions.

3. Compare the available numerical models for estimating the contact angle at different temperature and pH values.

Chapter 2 introduced some of the available theories and methods for contact angle prediction, such as the surface tension component (STC) method. However, we are not sure if these models are suitable for our experimental data and if the accuracy of the models will hold

with the experimental temperature and pH ranges. Therefore, in this study, we will verify if the available models are applicable to our experimental system and results. If they are not, we will discuss the reasons. We will also make corrections to identify whether there is a suitable model to describe the temperature and pH dependence of the contact angle obtained in our study.

Chapter 4 Experiment

4.1 Experimental Apparatus

The schematic of our experimental system for contact angle measurement is shown in Fig. 4-1. The core part of the system is a large steel cell with a quartz capillary inserted inside. Two fluid inlets are connected with a Masterflex Single Head Piston Pump from Cole-Parmer (which can adjust the flow rate from 10 to 300 mL/min), combined with 1/16-inch steel tubing controlled by the inlet valve. Different fluids (e.g., water, n-decane) can be injected into the capillary separately. The temperature of the system is controlled by eight heating cartridges (four per side) and a pre-heater at the fluid inlets. Pressure seals are installed at six different locations on the system to keep the system pressure constant, and a pressure gauge is employed to monitor the pressure variation. The system pressure can be adjusted using the pressure relief valve located at the top of the cell. The illumination of the system is carried out by inserting a fiber-optic light probe into the cell from the side opposite of inlets. This illumination allows us to see the phase interface and the three-phase contact point more clearly. A sapphire window is installed at the center of each side of the cell to provide a visual for monitoring and recording. The system illumination can be boosted by allowing ambient laboratory light to enter the system from the windows. The advancing interface is monitored and recorded using a Lumenera Infinity2 Microscopy Camera and computer software.

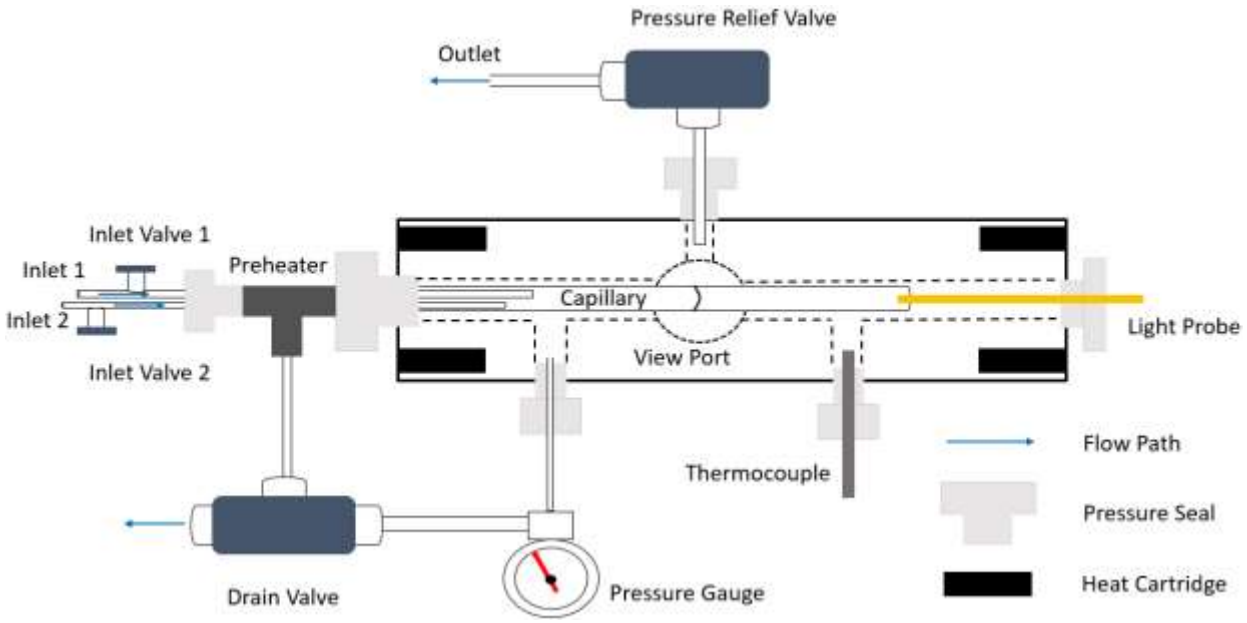

Fig. 4-1. Schematic of the experimental system.

Capillary-based systems have been used in previous studies to investigate the contact angle (e.g., Barajas et al., 1993; Al-Zaidi et al., 2018) under room conditions. Some non-capillary-based experimental systems have been developed to investigate the contact angle at high temperatures (e.g., Plevachuk et al., 2010; Sarmadivaleh et al., 2015; Blake et al., 2019). Our experimental system is the first capillary-based high-temperature contact angle device. Rather than allowing us merely to investigate the temperature dependence of the contact angle, our design enables us to study the effects of pH, flow rate, salt type, salinity and other parameters on the dynamic contact angle. In addition, three-phase contact point movement can be recorded continuously (about 5 mm) during the advancement of the fluids along the capillary tube.

4.2 Materials

In our experiments we studied the influence of temperature and pH on the contact angle. In the experiments in which temperature was the only variable, distilled water (DI water) and normal decane (nC_{10} or n-decane, >99%) from Sigma Aldrich were used as the experimental fluids. Isopropanol (70% in water) from Sigma Aldrich was utilized to flush the system frequently and eliminate impurities. The contact angle measurements were taken inside a fused quartz capillary with a 3 mm inner diameter manufactured by Technical Glass Products, Inc. In the experiments in which both temperature and pH were varied, hydrochloric acid (1.0 N standardized solution) from Alfa Aesar and sodium hydroxide pellets (>99 %) from Mallinckrodt Baker, Inc. were used for pH adjustment.

4.3 Methods

The silica surface is covered by a high density (4.6 groups/100 $Å^2$) of hydroxyl groups (Si-OH; Armistead et al., 1969). A Si-OH group is formed when siloxane (Si-O-Si) and water react. This process is called the surface hydroxylation of silica (Morel et al., 2009). The silica surface shows different hydroxylation states based on different dry pretreatment temperatures, different hydroxylation states impact the contact angle (Muster et al., 2001). In our experiments, to rehydroxylate the silica surface site, the quartz capillary was treated in 80 ℃ DI water for a week. Before the test, was performed the quartz capillary was flushed and filled with DI water. In the experiments studying the pH effect on the contact angle, HCl(aq) or NaOH(aq) was flushed and filled. The experiments were performed from 25 to 200 ℃ under a constant pressure of 1000 psi (69 bar). When the system was heated to a new experimental temperature, two days were given for the system to reach thermal stability (±0.3 ℃). Then, small amounts of fluid were injected into

the system to introduce the water/n-decane interface. In our experiments the roughness of the quartz capillary was assumed to be 1. The test of the roughness and homogeneity of the quartz surface is introduced in the next chapter.

During the experiments, the pump flow rate was set to 0.15 mL/min, and the flow velocity of the contact line was maintained at 0.71 mm/s. According to the dynamic contact angle theory, a more significant capillary number, λ_c, leads to a larger contact angle (Hilpert, 2009), while λ_c increases with an increase in the flow rate:

$$\lambda_c = \frac{\mu v}{\gamma_{ow}}, \tag{4-1}$$

where μ is the dynamic viscosity of the advancing fluid, v is the flow rate, and γ_{ow} is the interfacial tension on the fluid/fluid interface.

In our experiments, the flow rate variation did not impact the contact angle significantly. The measured contact angle decreased by around 0.6° when the flow rate was reduced from 0.71 to 0.09 mm/s at 25 °C. The contact angle measurements were carried out when the non-wetting phase, n-decane, was injected as the advancing phase. When the wetting phase, DI water, was the advancing phase, the advancing interface moved back and forth within a short section (0.05 mm to 0.2 mm) along the capillary and suddenly jumped a distance (0.5 mm to 1 mm) away, making image analysis difficult. The effects of pressure and the capillary diameter were also taken into consideration. To the best of our knowledge, the contact angle changes significantly under very high pressure; for instance, the contact angle in a mica/water/n-decane system increases around 8° when the pressure changes from atmospheric pressure to 30 MPa (Hansen et al., 2000). Nevertheless, in other studies, the contact angle variation due to pressure changes has been negligible (Siemons et al., 2006; Li et al., 2007; Song et al., 2020) within an approximate 0–100 bar pressure range. In our experiments, the system pressure was controlled at 1000 psi (69 bar). Recent studies have shown that the contact angle decreases as the larger capillary diameter increases capillary/brine/oil (Li et al., 2014) and capillary/brine/air systems (Al-Zaidi et al., 2018). Therefore, the inner diameter of the quartz capillary was held constant at 3 mm during our investigation.

The density (ρ) and viscosity (η) of water and n-decane, the solubility of water in n-decane, andthe water-decane interfacial tension (γ_{ow}) at each experimental temperature are presented in Table 4-1. Since the quartz capillary was positioned horizontally during the tests, the impact of

gravity on the DI water/n-decane interface must be considered when the capillary length, l_c, is greater than the capillary radius. l_c is defined as:

$$l_c = \sqrt{\frac{\gamma_{ow}}{\Delta\rho g}}, \tag{4-2}$$

where γ_{ow} is in mN/m, $\Delta\rho$ is the fluid density difference in g/mL; and g is the gravitational acceleration (9.81 m/s^2).

The calculated l_c decreases linearly from 4.4 mm at 25 °C to at 3.2 mm at 200 °C (Table 4-1); however, it is consistently higher than the diameter of the capillary (3 mm). Therefore, the influence of gravity on the shape of the interface appears to be negligible.

Table 4-1 Some properties of DI water and n-decane at different temperatures according to the literature.

t (°C)	ρ_w (kg/m^3) [1]	η_w (μPa s)[1]	ρ_o (kg/m^3) [2]	η_o (μPa s) [1]	Solubility of water in n-decane (mol %)[1]	γ_{ow} (mN/m) [3]	l_c (mm)
25	1000	891	737	919	0.04	50.25	4.4
50	991	547	718	661	0.14	47.24	4.2
75	978	378	698	502	0.35	44.23	4.0
100	961	282	678	396	0.82	41.21	3.9
125	942	222	656	322	1.73	38.20	3.7
150	919	183	633	267	3.45	35.19	3.5
175	895	155	608	224	6.65	32.18	3.4
200	868	134	580	191	12.81	29.16	3.2

[1] Calculated by OLI Studio v10; OLI systems, Inc.

[2] From webbook.nist.gov

[3] Extrapolated from Jennings (1967).

4.4 Image Analysis

The focus, contrast ratio and brightness of the videos documenting each experimental condition were adjusted and optimized at each experimental condition before they were taken. In

order to determine the impact of surface roughness, videos for each advancing interface (drainage process) were divided into snapshots at three consistent locations inside the capillary that were spaced 1.0 mm and 1.6 mm apart. ImageJ software (1.53a) with the Contact Angle plugin by Marco Brugnara was then used to interpret all contact angles. The schematic of the ImageJ analysis is shown in Fig. 4-2. The image was rotated 90° clockwise before the following analytical procedure was performed. First, the base line was generated by selecting the three-phase contact point and using the point as one end of the horizontal line perpendicular to the capillary wall (the white lines). Next, the contour line was formed by clicking points along the contour of the DI water/n-decane interface. Then, the contact angle θ was calculated based on an ellipse approximation.

During our experiments, the bottom contact points (left-hand side in Fig. 4-2) were slightly in front of the top contact points in each video. In other words, the other end of the base line was not the three-phase contact point. Therefore, we analyzed θ on each side. When comparing ImageJ with hand calculated θ results generated by Auto CAD, ImageJ gave 0.5° smaller contact angles than the hand calculations on average. In each temperature and pH condition, the measurement taken by ImageJ 36 times (18 times for each side of the capillary). In all our experiments, ImageJ's calculated θ gave a 1.2° average and 2.5° maximum of the standard deviation.

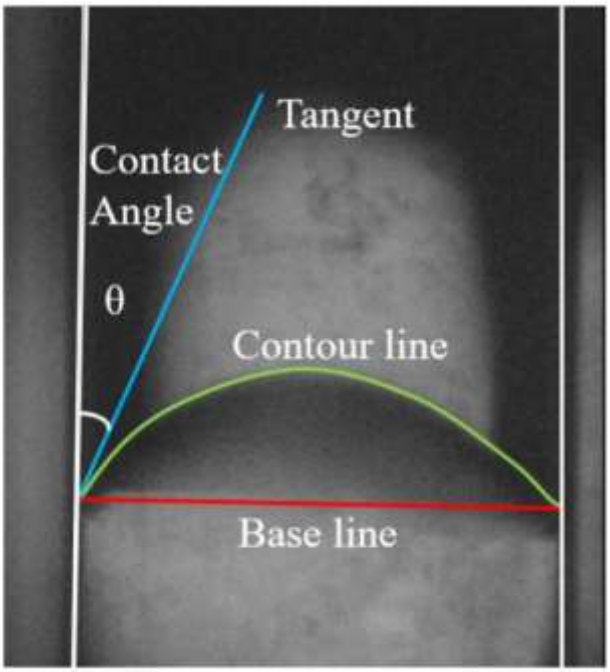

Fig. 4-2. ImageJ analysis of the contact angle at the quartz/distilled water/n-decane interface. The image of the capillary was rotated 90° clockwise for the ImageJ analysis. The inner quartz surface is outlined in white.

Chapter 5 Results and Discussion

5.1 Temperature Effect on Contact Angle (25-200 ℃) at Neutral pH

Temperature is one of the significant parameters that influence wettability and the contact angle. Previous studies showed that the temperature dependence of the contact angle is highly specific to the composition of the three-phase system. In our review, we found that a very limited number of relevant experiments based on a quartz/brine/n-decane system have been carried out.

Rao (1996) investigated the temperature dependence of the contact angle in a quartz/brine/crude oil system under 4.4 MPa. Their results showed that the contact angle remained nearly constant at 20° at the temperature range of 20 to 162 °C. The contact angle linearly increased from 20° at 162 °C to 180° at 196 °C. The data obtained by Kakati et al. (2018) in a quartz/1 M NaCl(aq)/n-decane system showed a linearly increasing trend from 25 to 55 ℃ for the contact angle. Zhang et al. (2018) measured the contact angle in a solid/brine/crude oil system at elevated temperatures (35 to 110 ℃) from 10 to 70 MPa. Nine different solid materials were tested. For quartz, the contact angle dropped to 8°; however, it was hard to see the contact angle changes on the carbonate and calcite surfaces as temperature increased. The contact angle measured by Haagh et al. (2018) in a quartz/diluted seawater/oil+0.1 mM stearic acid system decreased as the temperature increased to 40 ℃; it then began to increase until 60 ℃.

Recognizing that most studies involving quartz are limited within 100 ℃, we expanded the temperature range to 200 ℃. Our new experimental results contribute to scholars' understanding of wettability alteration in quartz/DI water/n-decane systems and help to elucidate the change in interactions between different phases across a wide range of temperatures.

5.1.1 Results

Our experimental results regarding the temperature dependence of contact angle from 25–200 ℃ are compared to those available in other literature in Fig. 5-1-1. The measured contact angles in our experimental systems show a strong linear temperature dependence, which increases 1.1° for every 5 ℃ and follows the $\theta=0.22T$ (℃) +14.28 trend ($R^2=0.988$). The standard deviation of the measured results at each temperature is less than 1.2°, which indicates a level of precision that is comparable to that of the ImageJ analysis mentioned in Section 4.4. Our experimentally obtained contact angle at 25 ℃ (18.9 °) is consistent with other available literature data (22° to 26°). Discrepancies between studies can be found in Fig. 5-1-1, which suggests that the contact

angle is highly specific to fluid composition and the contact angle measurement technique. Also, the dynamic contact angles were treated as 'equilibrium contact angle' during our experiments.

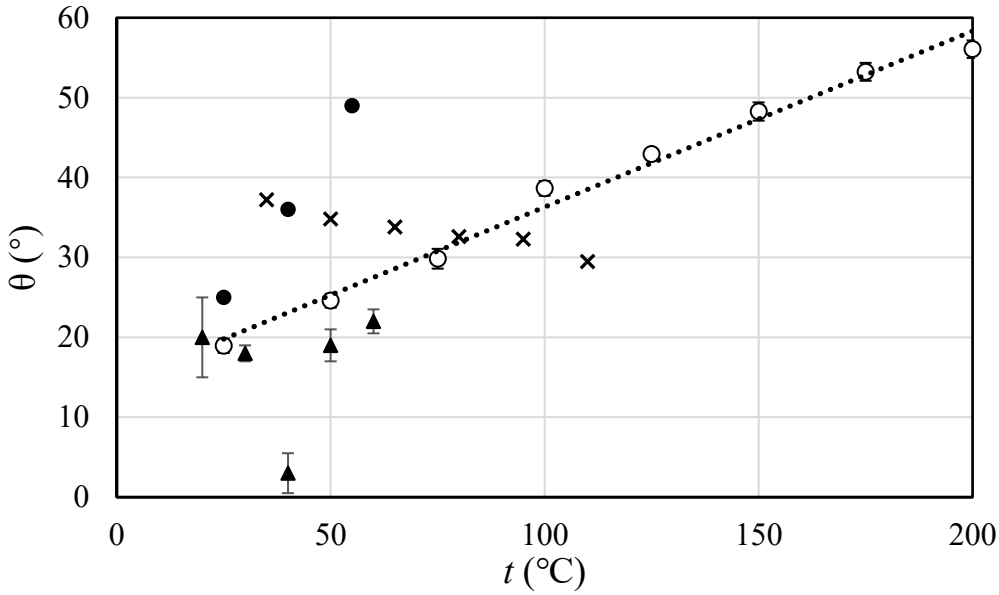

Fig. 5-1-1. Contact angle vs. temperature in quartz/liquid/liquid systems. "○"-This work (quartz/DI water/decane, 69 bar); "●" (Kakati et al., 2018), quartz/1 M NaCl(aq)/decane; "▲" (Haagh et al., 2018), quartz/diluted seawater/oil+0.1 mM stearic acid; "×" (Zhang et al., 2018) quartz/synthetic brine/crude oil, 100 bar.

Three representative images taken at 25, 125, and 200 ℃ during our experiments are shown in Fig. 5-1-2. These images indicate that the wettability of the system shifted from strong water-wet at 25 ℃ to intermediate-wet at 200 ℃. The same linear trend is found in studies by Kakati et al. (2018) and Rao (1999; not shown in Fig 5-1-1). However, the slope in our work (+1.1° per 5 ℃) is lower than the slopes calculated based on their results (+2.2° per 5 ℃ by Rao [1999], and +4° per 5 ℃ by Kakati et al., [2018]). This difference might be attributed to the presence of the salt composition such as NaCl(aq) in their studies, which may have changed the thickness of the electric double layer (EDL) and then increased the complexity of the temperature dependence of the contact angle. Furthermore, our investigation showed that only Haagh et al. (2018) conducted repeated measurements in their work (i.e., measured the contact angle from several water drops), making it difficult to determine whether other inconsistencies or sources of error are prevalent in the published data.

The same quartz capillary was used during all the tests. To ensure that the quartz surface's roughness and heterogeneity did not influence the measured contact angle results, the contact angle measurements were taken at three different locations along the capillary (Section 4.4). The measured results are shown in Fig. 5-1-3. The consistency along the length of the capillary distance at our experimental temperature range suggests that the contact angles were not significantly influenced by the surface roughness or heterogeneity during our experiments. Therefore, the surface roughness of the quartz capillary was assumed to be 1 in our work.

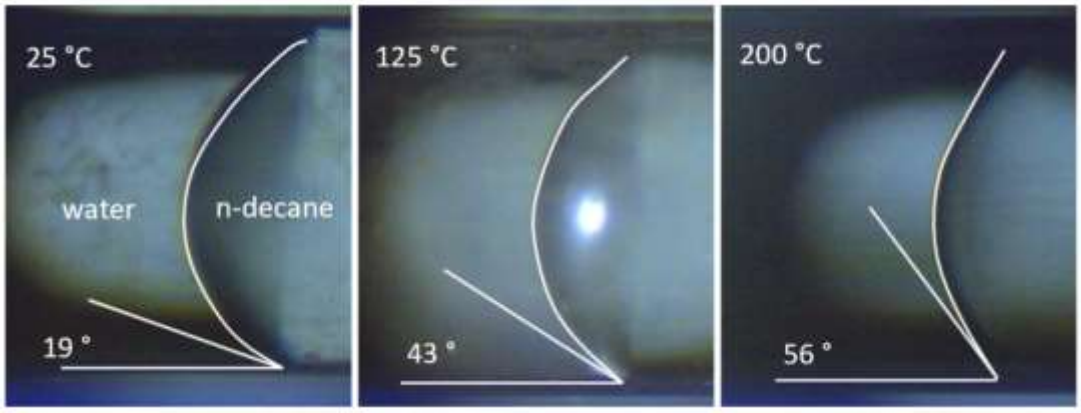

Fig. 5-1-2. Images of contact angles for the quartz/DI water/n-decane system at 25 °C, 125 °C, and 150 °C, showing contour and tangent lines and approximate θ as a visual guide.

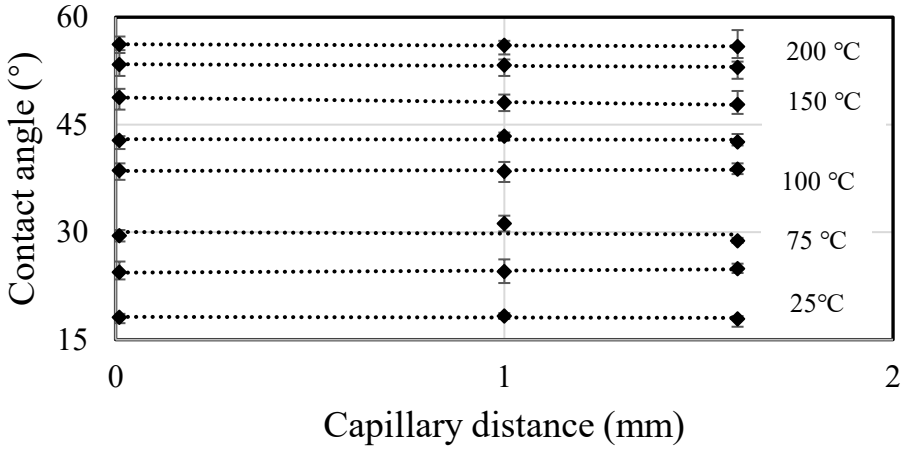

Fig. 5-1-3. Change in dynamic contact angle for the quartz/DI water/n-decane system corresponding to different locations inside the capillary at different temperatures (69 bar); each error bar represents the maximum error in the measurement.

5.1.2 Discussion

The variation in contact angle θ should be attributed to the change of chemical properties of the material surface and/or the forces acting on the interfaces. According to Young's equation, if γ_{so} and γ_{sw} are independent of temperature, the term $\gamma_{ow}\cos\theta$ must be independent of temperature as well. The calculated γ_{ow} value at the water/n-decane interface are listed in Table 5-1-1, combining with our experimental obtained θ, the values of $\gamma_{ow}\cos\theta$ at different temperatures are listed in Table 5-1-1. According to the calculated results, the value of $\gamma_{ow}\cos\theta$ decreases linearly from 25 to 200 ℃ by around three times; therefore, γ_{so} and γ_{sw} should not be regarded as temperature-independent. Unfortunately, while there is a substantial research on γ_{ow}, there is a limited amount of research on γ_{so} and γ_{ow}.

According to the dynamic contact angle theory, the capillary forces (e.g. flow rate and viscous forces) should be taken into consideration to describe the change of contact angle since our experimental system is a dynamic system (Schaffer et al., 2000). The following equation was suggested to correlate the equilibrium contact angle, θ_{eq}, and the dynamic contact angle, θ (Mumley et al., 1986):

$$\cos\theta_{eq} - \cos\theta = \alpha\lambda_c{}^{\beta}, \tag{5-1-1}$$

where α and β are positive model parameters and λ_c is the capillary number (Eq. 4-1). If v is taken as 0.71 mm/s in Eq. (4-1) then λ_c can be calculated and are listed in Table 5-1-1.

Table 5-1-1 DI water/n-decane interfacial tension (γ_{ow}), quartz/DI water contact angle (θ), n-decane viscosity ($\boldsymbol{\eta_o}$), and the calculated capillary number ($\boldsymbol{\lambda_c}$) at different temperatures.

t (℃)	γ_{ow} (mN/m) [1]	θ (°)	$\gamma_{ow}\cos\theta$	η_o (μPa s) [2]	λ_c
25	50.25	18.9	47.54	919	13.00
50	47.24	24.6	42.95	661	9.95
75	44.23	29.8	38.38	502	8.07
100	41.21	38.6	32.21	396	6.83
125	38.20	42.9	27.98	322	5.99
150	35.19	48.3	23.41	267	5.39
175	32.18	53.2	19.28	224	4.95
200	29.16	56.1	16.26	191	4.66

[1] Extrapolated from Jennings (1967).

[2] Calculated by OLI Studio v10, OLI systems Inc.

According to Eq. (5-1-1), assuming θ_{eq} remains constant with the temperature change, a decrease in λ_c will lead to a smaller θ. In Table 5-1-1, both η_o and λ_c show a linear negative temperature dependence, while we observed greater θ values at higher temperatures despite the deduction of λ_c. The calculated λ_c and the experimentally-measured contact angle conflict with the assumption we made previously based on a constant θ_{eq}. In other words, temperature-dependent viscous forces are not responsible for the observed shifts in θ as well as the wetting behavior of quartz. The aforementioned discussion convinces us that temperature-dependent wettability models must take adhesion changes at solid/liquid interfaces such as the quartz/DI water and quartz/n-decane interfaces in our work (i.e., γ_{sw} and γ_{so}) into account to have any predictive power. As noted in the previous chapter, the change in interfacial tension may be due to the change in the non-polar Van der Waals interactions and the polar acid-base interactions at the phase interface corresponding to the temperature change, and both polar and non-polar interactions take place at the solid/water and solid/oil interfaces. In the next chapter, we will discuss how the temperature influences these interactions.

During our experiments utilizing immiscible water/decane as the fluid components, it can be found that the solubility of water in n-decane (in mol%) increases from 0.04 % at 25 ℃ to 12.81% at 200 ℃ (Table 4-1). Different from our experimental system, regarding the more complex system during the oil recovery, the partitioning of the components between the fluid should be considered. The volatilization of lighter components (e.g., as carbon dioxide, methane, lighter alkanes) from crude oil may partition into the aqueous phase depending on the temperature, pressure, and composition of the system. This will in turn impact the oil-water interfacial tension due to the variation in the surface free energy (Fu et al., 1986) and may have implications for γ_{sw} and γ_{so} also. Returning to Young's equation, the denominator, γ_{ow}, decreases when the solubility of one fluid phase in another one increases, causing $\cos\theta$ to approach either -1 or +1, depending on the sign of the numerator. Meanwhile, when the two fluid phases become more 'similar,' the values of γ_{sw} and γ_{so} approach each other. Then, the numerator of Young's equation ($\gamma_{sw} - \gamma_{so}$) approach 0, causing $\cos\theta$ to approach 0 as well. Consequently, the change in the numerator and denominator in Young's equation in regard to the solubility change leads the value of $\cos\theta$ in contrasting directions, which increases the uncertainty for analysis.

5.2 pH (2–12) Effect on Contact Angle at Different Temperatures (25–200 °C)

Compared with the temperature dependence, the pH dependence of the contact angle in the available literature has a more consistent parabolic trend. No relevant literature based on quartz/water/n-decane was found. For those similar three-phase systems, Barranco et al. (1997) measured the contact angle in a quartz/0.4 M NaClO4(aq)/trichloroethylene system. They found that the contact angle increased by 4° from pH 0.5 to 1.5, and then the contact angle decreased by 13° from pH 1.5 to 10. Carré et al. (2003) conducted their experiments based on a bare glass/water/air system. The contact angle almost remained constant at 10° from pH 0 to 2, and it increased to 20° at pH 3. Finally, it decreased to 6° from pH 3 to 6. The results by Cuddy et al. (2013) in a silica/water/air system show that the contact angle changed from 7° at pH 2 to 8.5° at pH 3.9, then decreased to 3° at pH 13.

Such a concave parabolic variation trend can be explained from the view of Zeta potential, ζ. In colloidal science, ζ is used to describe the stability of particle suspension and investigate colloid-electrolyte interactions (Gaikwad et al., 2019). A higher magnitude of ζ (|ζ|>40 mV) (Kumar et al., 2017) indicates a more significant repulsion between the surface and particles in the bulk phase. Consequently, the system becomes more stable. Previous studies suggested that the silica surface is hydrophilic due to the presence of the polar O-H groups in silanols (Rallini et al., 2017). In other words, the oil-phase, (i.e., n-decane in our experiments) is the bulk phase, or the phase that will be repelled by the quartz surface. The Zeta potential of quartz indicates the degree of electrostatic repulsion between the quartz surface and n-decane. The stronger the repulsion, the more hydrophilic the quartz is, and a smaller contact angle can be observed. In contrast, when ζ falls to 0, the weakest repulsion between the quartz surface and n-decane leads to the maximum contact angle. Correspondingly, the pH value correlated with the maximum contact angle (i.e., the aforementioned critical pH value), which is called the isoelectric point (pH_{iep}), corresponds to 0 the Zeta potential of the solid material. The reactions taking place at the silica surface can be written as (Sabia et al., 2000):

$$-\mathrm{SiOH} + \mathrm{H^+(aq)} \leftrightarrow -\mathrm{SiOH_2^+}\ (\mathrm{pH}<\mathrm{pH_{iep}}), \tag{5-2-1}$$

$$-\mathrm{SiOH} \leftrightarrow -\mathrm{SiO^-} + \mathrm{H^+(aq)}\ (\mathrm{pH}>\mathrm{pH_{iep}}). \tag{5-2-2}$$

According to these reactions, when pH is lower than pH_{iep}, the quartz surface is positively charged due to the $-SiOH_2^+$ group (protonation of the surface). An increase in pH moves the reaction (5-2-1) to the left (Le Chatelier's principle), which makes the quartz surface less positively charged (deprotonation). Then, ζ of quartz becomes less positive, the electrostatic repulsion between the quartz surface and n-decane decreases, the system shifts to less-water wet, and the observed contact angle increases until the pH is equal to pH_{iep}. When pH is higher than pH_{iep}, the quartz surface is negatively charged with the $-SiO^-$ group (surface deprotonation). The reaction (5-2-2) will move right-wards with the increase in pH, and there will be more negative charges on the quartz surface. Then, ζ of quartz becomes more negative, the system becomes more stable by repelling n-decane farther away from the quartz surface, the system changes to more water-wet, and the observed contact angle drops.

Although the variation trend in the contact angle with respect to pH is similar, the value of pH_{iep} and the maximum contact angle are specific to the three-phase composition. In addition, most of these pH dependence experiments were carried out under room conditions. In this section, the pH effect on the contact angle in a quartz/DI water/n-decane system is investigated at different temperatures (25–200 °C). These experiments show whether a similar parabolic trend is found at these temperatures and how pH alters the interactions in the three-phase system.

Compared with Section 5.1, which featured an aqueous phase with neutral-pH DI water, this section relies on an aqueous phase with 10^{-2} mol/kg and 10^{-4} mol/kg HCl(aq) and NaOH(aq) to investigate the impact of pH on contact angle. The other experimental conditions were kept constant. Thus, there are be four different pH values at the same temperature.

5.2.1 Temperature Effect on pH Values

The pH value of a liquid can be written as:

$$\mathrm{pH} = -\log\left[\gamma_{b,\mathrm{H^+(aq)}} * b_{\mathrm{H^+(aq)}}\right], \tag{5-2-3}$$

$$\mathrm{pH} = K_\mathrm{w} - \mathrm{pOH} = \mathrm{p}K_\mathrm{w} + \log\left[\gamma_{b,\mathrm{OH^-(aq)}} * b_{\mathrm{OH^-(aq)}}\right], \tag{5-2-4}$$

$$\mathrm{pH} = \frac{\mathrm{p}K_\mathrm{w}}{2}, \tag{5-2-5}$$

where $\gamma_{b,i}$ is the activity coefficient of the ion i on the molal concentration scale, b_i is the molality of the ion i, and pK_w is the negative decimal logarithm of the ionization constant of water. Eq. (5-2-3) and (5-2-4) are for the aqueous solution in which H^+(aq) and OH^-(aq) can be produced by the dissociation of the electrolyte, respectively. Eq. (5-2-5) is for pure water in which H^+(aq) and OH^-(aq) can be produced solely by its ionization.

The molality of the pH-determined ions, H^+(aq) and OH^-(aq), depends on the dissociation of the acid and base in the aqueous solution, which can be reflected by the association constant, K_A (Lvov et al., 2018). K_A is a function of temperature and pressure. The activity coefficients of HCl(aq) and NaOH(aq) can be obtained based on the Debye–Hückel theory (Lvov, 2014). The Debye–Hückel theory relies on water density (ρ_w) and the relative permittivity of water (ε_w), in need, and these two parameters are functions of temperature and pressure. The relative water properties at the experimental conditions are listed in Table 5-2-1.

Table 5-2-1 Water properties at the experimental conditions.

t (°C)	P (bar)	ρ_w (kg/m^3)[1]	pK_w[1]	ε_w
25	69	1000	13.97	78.7
50	69	991	13.24	70.2
100	69	962	12.23	55.8
125	69	942	11.88	49.7
150	69	921	11.61	44.3
200	69	869	11.28	35.0

[1] From www.energy.psu.edu/tools/ionization0730/index.php

With the obtained water properties, the activity coefficient in dilute aqueous solutions can be calculated. Then, combining the association constant, charge balance equation, and mass balance equation, the molalities of the pH-determined ions can be calculated. Plugging the calculated γ_b and b into Eq. (5-2-3) to (5-2-5), the pH values of the aqueous solutions at different temperatures can be obtained (Table 5-2-2) as described in Lvov (2021). The detailed calculation process is shown in Appendix A. From Table 5-2-2 we can see that the pH values fall as the temperature increases; for instance, the pH of DI water drops from 6.99 at 25 °C to 5.64 at 200 °C. However, this does not indicate that the DI water has become more acidic. A solution is regarded as acidic when and only when the concentration of H^+(aq) exceeds that of OH^-(aq). In the case of pure water, this will not happen due to the self-ionization reaction of water. pH 7 is usually

considered the scale of the neutral pH. Nevertheless, this scale decreases when the temperature increases. As a result, lower pH values at higher temperatures when there is the same concentration of acid or base can be observed in Table 5-2-2.

Table 5-2-2 Calculated pH values for DI water and different concentrations of the aqueous solution at the experimental conditions.

t (°C)	P (bar)	10^{-2} mol/kg HCl(aq)	10^{-4} mol/kg HCl(aq)	DI water	10^{-4} mol/kg NaOH(aq)	10^{-2} mol/kg NaOH(aq)
25	69	2.05	4.01	6.99	9.96	11.93
50	69	2.05	4.01	6.62	9.23	11.19
100	69	2.05	4.01	6.12	8.22	10.18
125	69	2.06	4.01	5.94	7.87	9.82
150	69	2.06	4.01	5.81	7.60	9.55
200	69	2.07	4.01	5.64	7.27	9.21

5.2.2 Results

The measured contact angles in the quartz/water/n-decane system at different pH values and temperatures are shown in Fig. 5-2-1. It can be observed that the temperature dependence of the contact angle is consistent with the results in Section 5.1. In addition, starting from the acidic pH, the system becomes less water-wet (the contact angle decreases) with the increase in pH. However, our experiments show that this trend will be reversed when a critical pH value is reached, and the critical pH value is different at each temperature. Then, beginning from the critical pH, the measured θ decreases when the pH increases to a more basic pH, indicating the system becomes more water-wet. At the same temperature, the minimum contact angle is consistently observed at the most basic pH, suggesting that the quartz capillary is more water-wet at the highly-basic region than the highly acidic region. The average and the maximum standard deviation of the measured contact angles are 1.1° and 2.5°, respectively.

Due to the lack of available technical reports, we were unable to compare our experimental results to results found at other temperatures. Fig. 5-2-2 shows a comparison of our experimentally obtained contact angle at different pH values with the data from the available literature at 25 °C. A similar contact angle variation trend regarding the pH change can be observed. Our measured contact angle at pH=2 is very close to the one reported by Barranco et al. (1997), while at pH=4 the difference between our data and Carré et al. (2003) reaches 7.9°. Meanwhile, discrepancies in the pH value at which the contact angle reaches its maximum can be found. These differences in

the reported contact angle may be attributed to the differences in fluid composition, solid material, and measurement technique.

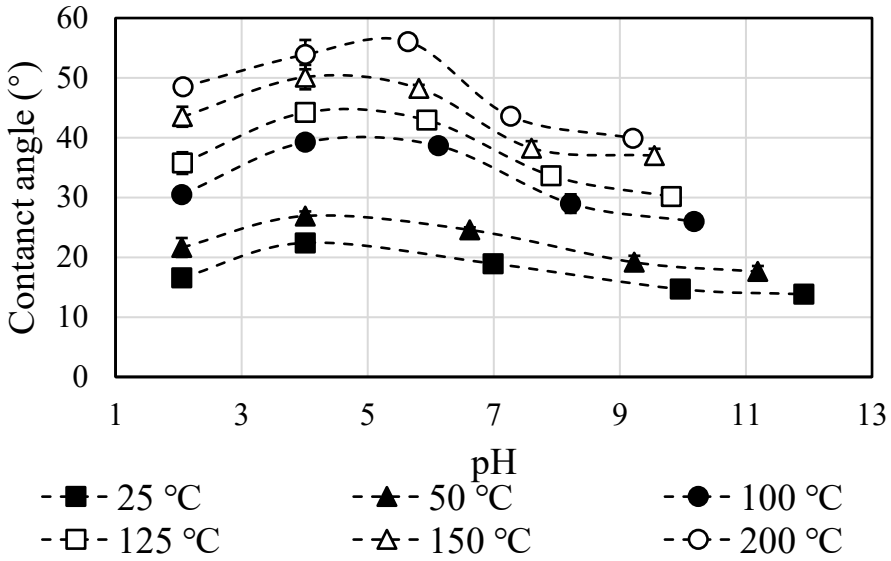

Fig. 5-2-1. Contact angle vs. pH at different temperatures and 69 bar. The error bars represent standard deviation.

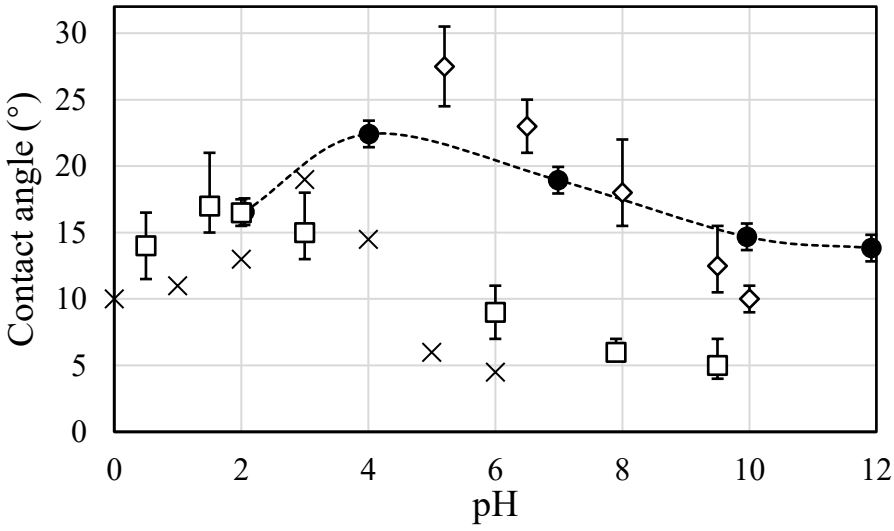

Fig. 5-2-2. Contact angle vs. pH in quartz/liquid/liquid systems at 25 °C. "●" This work, quartz/DI water/decane, 69 bar; "□" (Barranco et al., 2018), quartz/0.4 M $NaClO_4$(aq)/

trichloroethylene; "◊" (Barranco et al., 2018), quartz/0.1 M $NaClO_4$(aq)/ trichloroethylene; "×" (Carré et al., 2003), bare glass/water/octane.

5.2.3 Discussion

As the previous sections shows, the pH dependence of the contact angle in our experiments agrees with the aforementioned concave parabolic trend, and a change in temperature does not influence the trend. The effect of pH on the Zeta potential of quartz has been investigated in many previous studies (Salopek et al., 2017; Liu et al., 2017; Yang et al., 2018). In these studies, ζ of quartz decreases linearly from a slightly positive value (+5 mV to +10 mV) at the acidic pH to a strongly negative value (-60 to -80 mV) at the basic pH. Therefore, the variation in the electrostatic repulsion between the quartz surface and n-decane at different pH values accounts for the wettability alteration in our experimental system.

Amadu et al. (2019) derived the following equation to qualitatively capture the pH dependence of the contact angle in a solid/liquid/liquid system:

$$\cos\theta = \left(\cos\theta_{\mathrm{iep}} + 0.5\xi\ \mathrm{pH}_{\mathrm{iep}}^2\right) - \xi \mathrm{pH}_{\mathrm{iep}}\ \mathrm{pH} + 0.5\xi\ \mathrm{pH}^2, \tag{5-2-6}$$

where θ_{iep} is the contact angle corresponding to $\mathrm{pH}_{\mathrm{iep}}$. Both $\mathrm{pH}_{\mathrm{iep}}$ and θ_{iep} were obtained based on the experimental data from other literature (i.e., they were not theoretically derived or calculated). The parameter ξ can be written as:

$$\xi = \frac{e}{k_B T \gamma_{\mathrm{ow}}}\left[\frac{\varepsilon n k_B T}{2\pi}\right]^{0.5}\left(\frac{2.303 k_B T}{e}\right)^2, \tag{5-2-7}$$

where e is the elementary charge (1.602×10^{-19} C), k_B is the Boltzmann constant (1.381×10^{-23} J/K), γ_{ow} is oil-water interfacial tension (mN/m), n is the number density of the ions in the bulk solution (m^{-3}), and ε is the relative permittivity of the background electrolyte solution, when the concentration of the solution is less than 1.5 mol/L. In this equation ε can be calculated based on the relative permittivity of water (Gavish et al., 2016):

$$\varepsilon = \varepsilon_w - \alpha c, \tag{5-2-8}$$

where α is a phenomenological ion-specific parameter, known as the total excess polarization of the ionic species ($Å^{-3}$). c is the molarity of the background electrolyte solution (mol/L).

We attempted to calculate the contact angle based on our experimental system and the numerical model by Amadu et al. (2019). However, an inferior agreement was found between the calculated and the experimental values (see Appendix B). Both γ_{so} and γ_{ow} were assumed to be pH-independent in their model. The reasons for such a significant discrepancy may be due to the lack of a background electrolyte solution such as $MgCl_2$(aq) utilized by Amadu et al. (2019), or the high specificity of pH_{iep} and θ_{iep} in different three-phase systems. More importantly, based on our discussion of Zeta potential, at least γ_{so} is pH-dependent. Alkaline flooding is a common technique employed in EOR. In alkaline flooding, chemicals such as NaOH(aq), Na_2CO_3(aq), or Na_4SiO_4(aq) are injected to the wellbore to react with certain types of species in oil to reduce the interfacial tension at the water/oil interface (γ_{ow}; Sheng, 2013). Neumann (1974) derived the following equation for the interfacial tension terms in Young's equation:

$$\gamma_{sw} = \frac{\gamma_{so}+\gamma_{ow}-2\beta\sqrt{\gamma_{so}\gamma_{ow}}}{1-2\alpha\sqrt{\gamma_{so}\gamma_{ow}}}, \tag{5-2-9}$$

where α and β are model parameters.

From Eq. (5-2-9), the denominator will decrease if γ_{ow} decreases by turning the system more basic with alkane flooding, while the change of the numerator will be decided by the value of β and γ_{so}, the change of numerator and denominator increases the uncertainty of predicting the change of γ_{sw}. The contact angle in a quartz/brine/crude oil system increased from 24° to 165° with the presence of 0.5 wt. % NaOH(aq) (Gong et al., 2016) suggesting that the changes in γ_{so} and γ_{sw} at different pH values are why cos θ shifted from a positive value to a negative value. Therefore, similar to the temperature effect, the interactions on the quartz/water, quartz/n-decane, and water/n-decane interfaces must be considered to create a wettability/contact angle model with some predictive capability.

5.2.4 Different Approaches to Fitting the Experimental Results

In addition to the equation derived by Amadu et al. (2019, Eq. 5-2-6), a second-order polynomial relation between θ (or cos θ) and pH has been reported by some other researchers (Carré et al., 2003; McCafferty et al., 1999; Virga et al., 2018). Based on this quadratic trend, the extreme point of the θ (or cos θ) vs. pH curve was determined to be the pH_{iep} of the solid material. Therefore, the quadratic equation was used to fit our experimental results at different temperatures. Fig. 5-2-3 shows the quadratic fitting results at 25 ℃. The fitted results suggest that the predictive power of the quadratic equation can be described as near-substantial (Henseler et al., 2009). The obtained R^2 values are 0.769, 0.778, 0.801, 0.724 and 0.774 for 50, 100, 125, 150 and 200 ℃, respectively. Comparing the experimental and the fitted results, the pH_{iep} is 4 based on the experimental results, while the pH_{iep} observed from the quadratic fit is between 5 and 7. Moreover, there is around a 2.5° difference between the θ_{iep} values obtained by the quadratic equation and the highest experimentally measured contact angle. According to our investigation, if we use the quadratic equation to fit the reported θ (or cos θ) vs. pH results in other literature, the R^2 value of the quadratic fits will vary from 0.38 (Abdel-Khalek et al., 2015) to 1 (Hurwitz et al., 2010). These comparisons suggest there might be a different equation to be used.

The cubic equation is also used to fit the experimental results. Fig. 5-2-4 shows the Zeta potential of quartz at different pH values reported in other literature. Due to the continuous adsorption of the OH^-(aq) ion, the double layer will be compacted if the concentration of the hydroxide ion on the silica surface is too high (Ruan et al., 2018). As a consequence, the electrostatic repulsion between the surface and the bulk phase will be hampered. The stability of the system will then drop, and the magnitude of the Zeta potential of quartz will stop increasing and start to decrease at a specific pH. In the previous quadratic fitting, we found that the magnitude of the Zeta potential increases monotonically with pH at the basic region. Therefore, the cubic equation was employed, and Fig. 5-2-5 shows the cubic fitting results at 25 ℃. Compared with the results of the quadratic fit, the obtained R^2 increased from 0.697 to 0.971, and the obtained R^2 values were 1, 0.981, 0.987, 0.967 and 0.887 for 50, 100, 125, 150, and 200 ℃, respectively. Meanwhile, the θ_{iep} and pH_{iep} obtained using the cubic equation suggest a smaller discrepancy with the experimental and the fitted results than that seen with the quadratic fit.

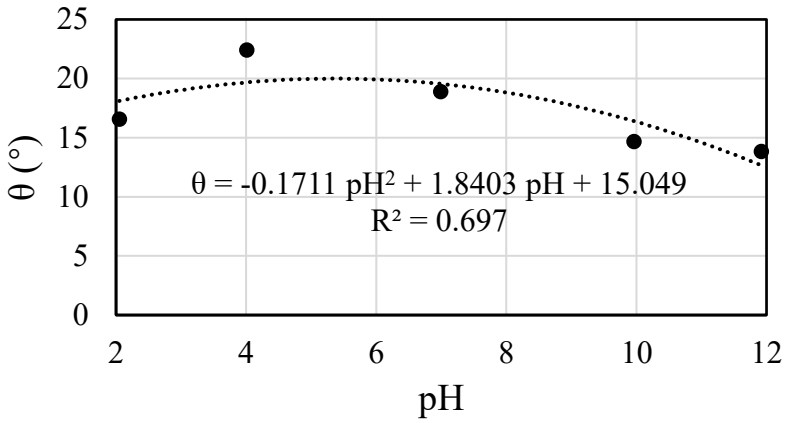

Fig. 5-2-3. Quadratic fitting results at 25 ℃. The dots represent the experimental results, and the dashed line represents the second-order polynomial curve.

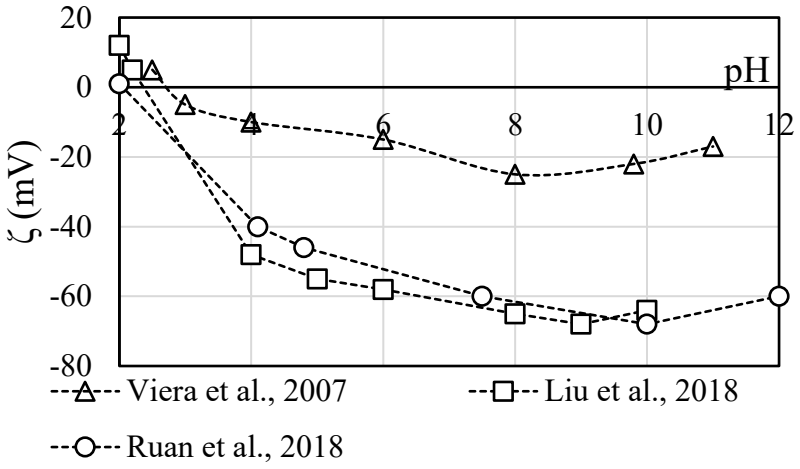

Fig. 5-2-4. Zeta potential of quartz vs. pH reported in literature.

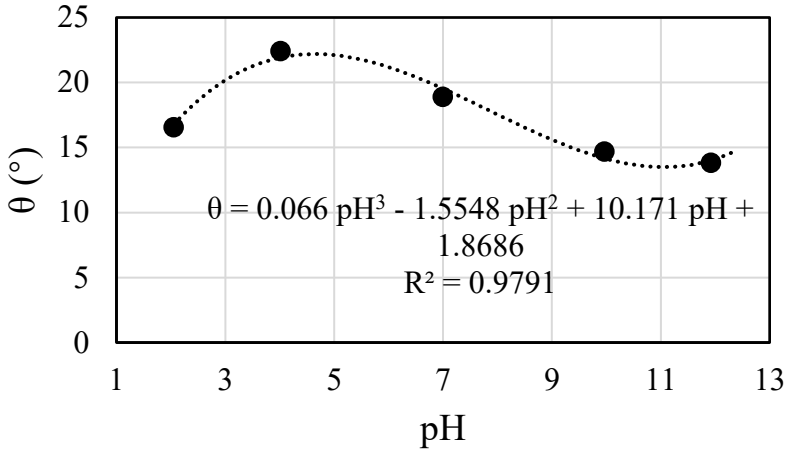

Fig. 5-2-5. Cubic fitting results at 25 ℃. The dots represent the experimental results, and the dashed line represents the second-order polynomial curve.

To the best of our knowledge, there are no existing theoretical or empirical equations that describe the correlation among contact angle, pH, and temperature simultaneously. Therefore, we utilized the curve fitting tool in MATLAB to identify an analytical correlation that depicts contact angle as a function of pH and temperature via different mathematical combinations (e.g. log(pH), T^2). After fitting a number of times, the empirical equation with the highest accuracy (R^2=0.98) was found to be:

$$\theta = -0.0004432\,T^2 + 0.6192\,T - 54.95\log(T) + 0.6497\,\mathrm{pH}^2 - 17.77\,\mathrm{pH} + 139\log(\mathrm{pH}) - 0.00732\,(T\,\mathrm{pH}). \quad (5\text{-}2\text{-}10)$$

We call Eq. (5-2-10) the 'general correlation.' The calculated and the experimentally-obtained contact angles are shown in Fig. 5-2-6.

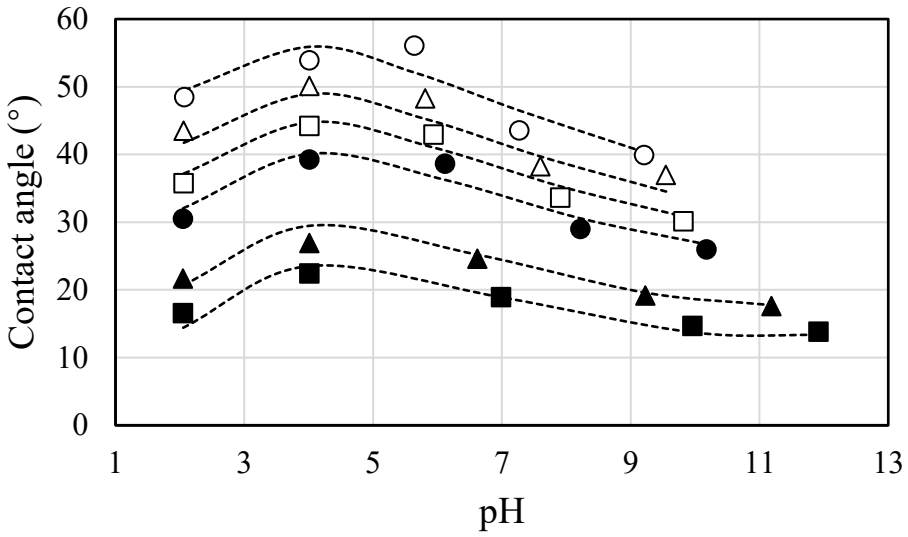

Fig. 5-2-6. Calculated θ vs. experimentally obtained θ. The dotted lines represent the results calculated using Eq. (5-2-10), and the shapes represent the experimental results ("■"-25 ℃; "▲"-50 ℃; "■"-100 ℃; "□"-125 ℃; "Δ"-150 ℃; "○"-200 ℃).

Fig. 5-2-7 shows the generated tornado plots based on the general correlation. Tornado plots were used to test the sensitivity of each term in the general correlation. For example, the blue bar in Fig. 5-2-7 corresponds to the term 'T^2', indicating that the value of the temperature was decreased to 80% of its original value (from 298.15 K to 238.52 K). Then, the changed value was plugged back into the first term on the right-hand side of Eq. (5-2-10), while the other terms remained unchanged. The calculated θ value is at the right end of the blue bar. The orange bars indicate the corresponding values rose to 120% of their original value. The bold horizontal line is the y-axis, which is the calculated θ value via the original values. The longer the bar, the more sensitive the term in the general correlation is.

The tornado plots generated at three representative temperatures and pH values show that in the general correlation, the 'T' term is the most sensitive, while the 'T*pH' term is the least sensitive.

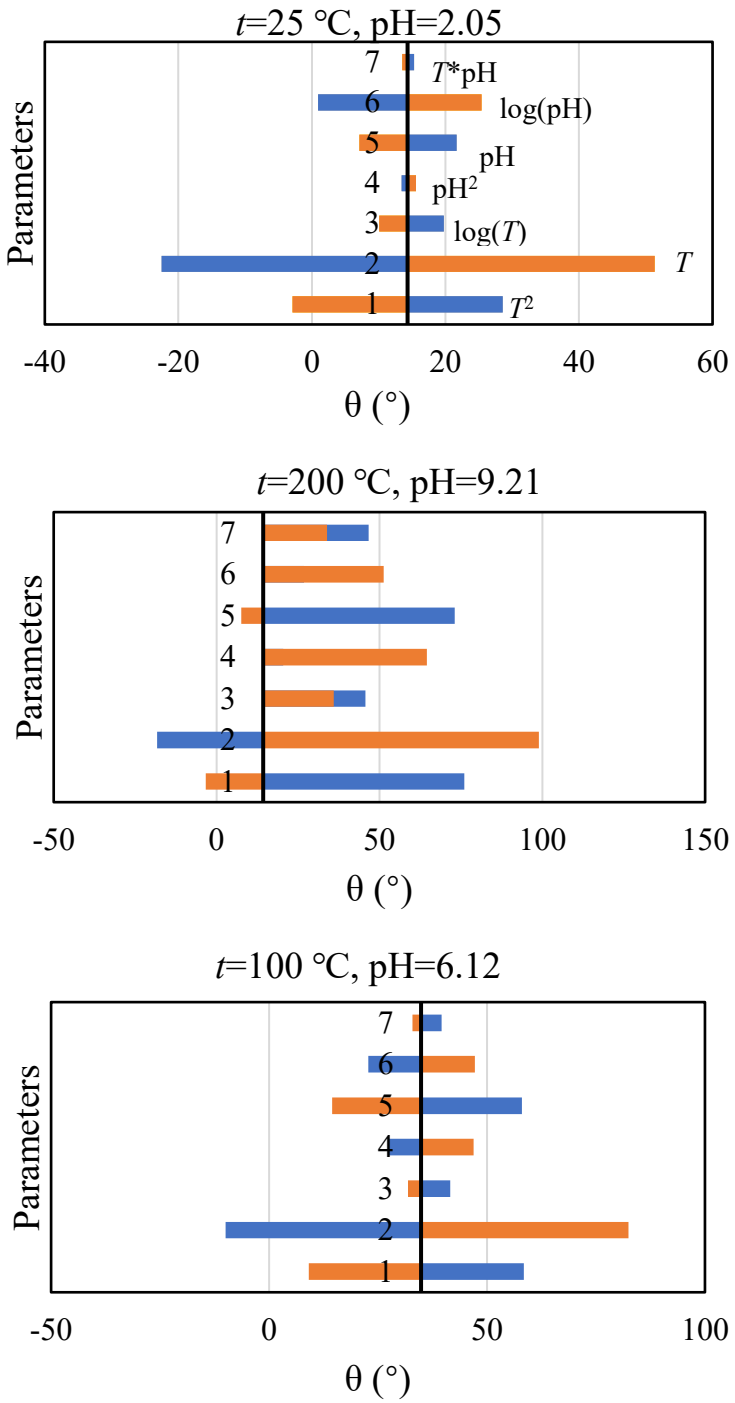

Fig. 5-2-7. Tornado plots generated based on different experimental conditions. The blue bars represent the contact angles calculated by changing the corresponding term to 80% of its original value. The orange bars represent the contact angles calculated by changing the corresponding term to 120 % of its original value.

Chapter 6 Isoelectric Point of Silica

By definition, the isoelectric point (iep) corresponds to the zero Zeta potential. An illustration of Zeta potential is shown in Fig. 6-1. According to the electric double layer (EDL) theory, the region near the charged surface is divided into the stationary layer and the diffuse layer. Assuming the surface is negatively charged, the near-surface stationary layer consists of immobile ions. The Stern layer is within the range of the stationary layer, and it is a layer of counterions attracted on the surface due to the Coulomb force. The diffuse layer, which can be regarded as the bulk phase far from the surface, consists of mobile ions that obey Poisson-Boltzmann statistics (Butt et al., 2006). Zeta potential is the electric potential at the slipping plane, which is the boundary between the stationary layer and the diffuse layer. The isoelectric point is an important property for a solid material in the aqueous dispersions. It defines the surface excess of ions, stability against coagulation, and rheological properties of dispersions, anong other aspects (Kosmulski, 2016).

The point of zero charge (pH_{pzc}) is another commonly investigated property of a solid. pH_{pzc} is related to a zero net surface charge. Miller (2020) suggested that the velocity of the particles subjected to an external electric field and the net charge at the slipping plane is zero at pH_{iep}, though that does not necessarily mean the net surface charge is zero at pH_{iep}.

The terms pH_{iep} and pH_{pzc} are often used interchangeably. For example, the pH_{iep} of solid materials can be determined via the maximum contact angle (McCafferty et al., 1999; Trevino et al., 2011), while the same method has been applied to decide the pH_{pzc} (Cuddy et al., 2013; Virga et al., 2018). Zhou and Lvov et al. (2003) suggested that pH_{pzc} and pH_{iep} are the same in the absence of specifically adsorbed ions. The specific adsorption can be interpreted as the adsorption of ions other than $H^+(aq)$ and $OH^-(aq)$ within the Stern layer. In Chapter 5 we introduced protonation and deprotonation on the silica surface (Eq. 5-2-1 and 5-2-2), in which the adsorption of non pH-determined ions was not considered. Therefore, we took pH_{iep}, as the topic to be discussed in this chapter.

In addition to the contact angle measurement, electrophoresis and electroosmosis can be used to determine Zeta potential. Most of the modern Zeta potential analyzers work based on electrophoresis (Schwarz et al., 2000; Simonsson et al., 2018). However, most of the pH_{iep} values are determined at room temperature. Rodriguez et al. (2006) reported that the pH_{iep} of quartz dropped from 2.3 at 20 ℃ to 2.0 at 45 ℃. In Wiśniewska (2010), the pH_{iep} of silica decreased from 2.2 at 15 ℃ to 1.95 at 35 ℃. Most of the temperature dependence experiments have been

conducted at temperatures under 100 ℃. In this chapter, we investigate the temperature dependence of the isoelectric point of silica at elevated temperatures up to 200 ℃.

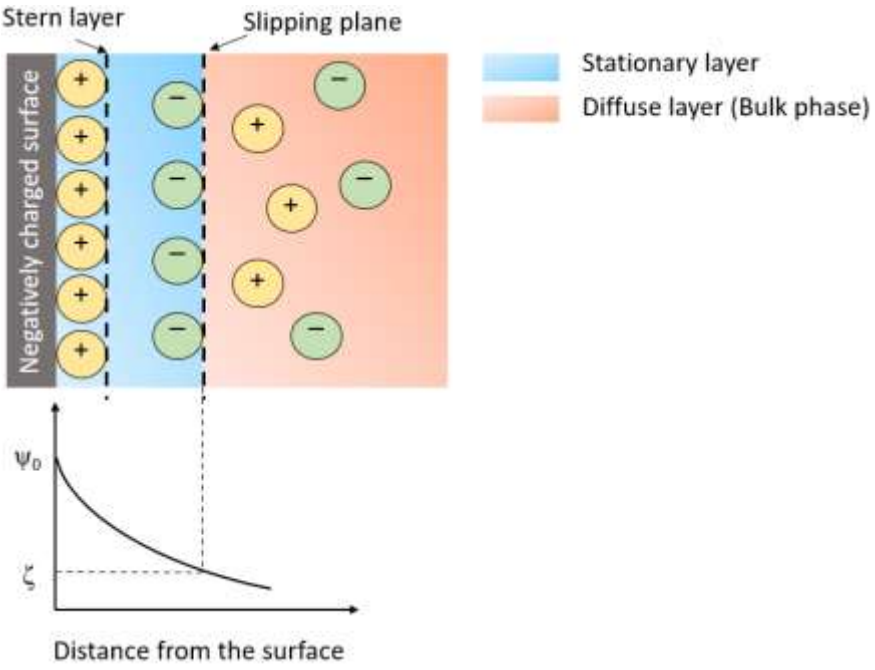

Fig. 6-1. An illustration of the double layer and Zeta potential.

6.1 Isoelectric Point of Silica in This Work

In the previous chapter, we explored different approaches to describing the relation between pH and contact angle at different temperatures: the quadratic equation, the cubic equation, and the empirical 'general correlation' which includes temperature, pH, and contact angle in a single equation. From the figures drawn based on these approaches, different isoelectric points, pH_{iep}, can be observed (Fig. 5-2-3 to Fig. 5-2-6). To determine the exact value of the pH_{iep}, we need to solve the first-order derivative of the quadratic and cubic equations. For the quadratic equations, there is only one extreme point, and the extreme point is pH_{iep}. This is the same treatment that appears in the literature (Carré et al., 2003; McCafferty et al., 1999). In the cubic equations, however, two extreme points are observed in the cubic equations, and the pH value corresponding to the higher contact angle is taken to be the value of pH_{iep}. The first-order partial derivative of the general correlation with respect to pH was derived as:

$$g(\mathrm{pH},T)=\left[\frac{\partial f(\mathrm{pH},T)}{\partial \mathrm{pH}}\right]_T=1.2994\,\mathrm{pH}-0.00732\,T+\frac{60.3669}{\mathrm{pH}}-17.77. \quad (6\text{-}1\text{-}1)$$

The second-order partial derivative of the general correlation with respect to pH was derived as:

$$k(\mathrm{pH})=\left[\frac{\partial^2 f(\mathrm{pH},T)}{\partial \mathrm{pH}^2}\right]_T=1.2994-\frac{60.37}{\mathrm{pH}^2}. \quad (6\text{-}1\text{-}2)$$

The graphs of the first-order and second-order partial derivatives of the general correlation with respect to pH are shown in Fig. 6-1-1. Fig. 6-1-1 (a) suggests that there are two possible pH_{iep} values within the 0 to 15 pH range. From Fig. 6-1-1 (b), the second-order derivative indicates the general equation is concave at the acidic region, and it changes to convex as the pH increases. Therefore, the pH_{iep} at the basic region should be discarded.

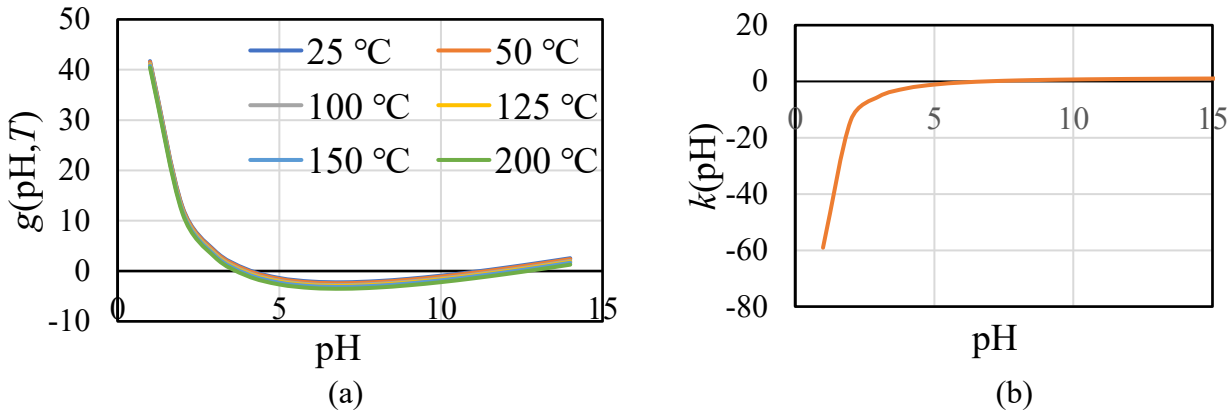

Fig. 6-1-1. (a) First-order partial derivative of the general correlation with respect to pH, *g*(pH, *T*). (b) Second-order partial derivative of the general correlation with respect to pH, *k*(pH).

Based on this discussion, only one pH_{iep} value should be regarded as reasonable. The pH_{iep} values obtained using the different approaches at different temperatures are shown in Fig. 6-1-2. The white circle, triangle, and square represent the pH_{iep} values that result from the quadratic fit, cubic fit, and the general correlation, respectively. From 25 °C to 200 °C, the quadratic fit suggests the highest pH_{iep} values, the general correlation suggests the lowest pH_{iep} values, and the cubic fit

suggests the intermediate pH_{iep} values. The θ_{iep} predicted by these three methods is shown in Fig. 6-1-3, and the predicted θ_{iep} of the cubic equation is always lower than the maximum experimeanlly measured contact angle. In contrast, the θ_{iep} calculated by the cubic equation and the general correlation are both in good agreement with the experimental maximum.

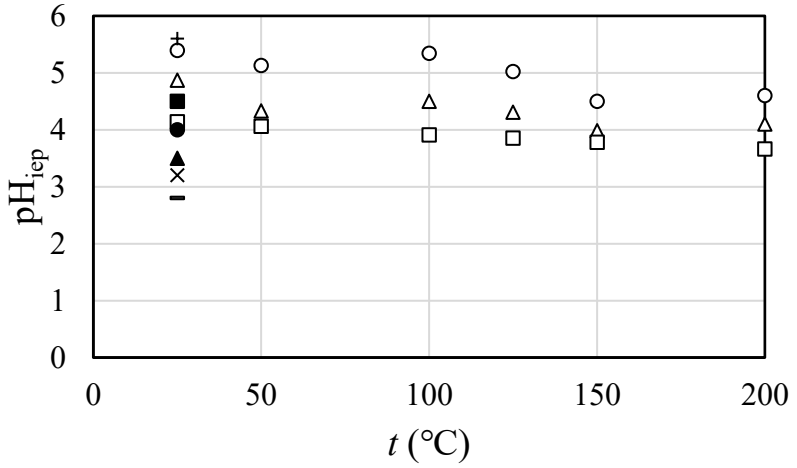

Fig. 6-1-2. pH_{iep} of silica determined using three different approaches from 25 to 200 ℃, in addition to the data from the available literature at 25 ℃. "○" This work, fused silica capillary, quadratic fit. "Δ" This work, cubic fit. "□" This work, general equation. "+" (Trevino et al., 2011), SiO_2 film treated with plasma vapor. "■" (Schwarz et al., 2000), Sikron from Quartzwerke. "●" (Gusev et al., 2002), fused silica capillary. "▲" (Sabia et al., 2000), fused SiO_2. "×" (Noh et al., 1989), Cabot L90 SiO_2. "-" (Zhou et al., 2015), quartz from China.

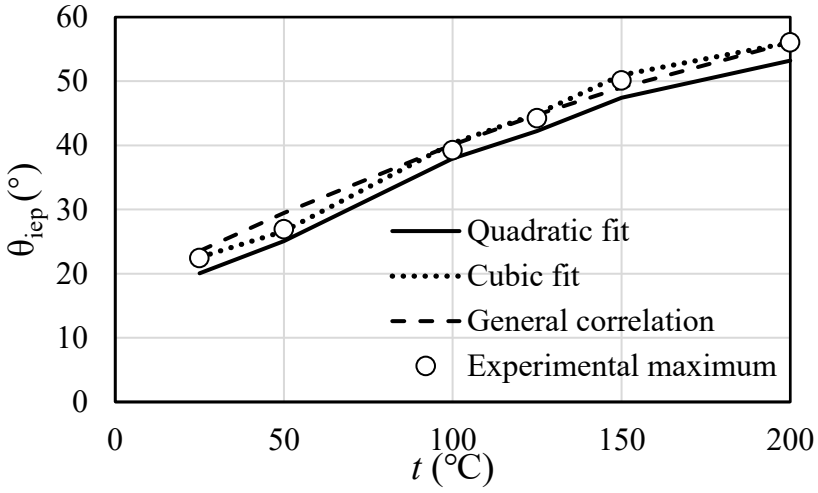

Fig. 6-1-3. θ_{iep} of silica determined using three different approaches from 25 ℃ to 200 ℃, plotted against the experimentally measured maximum contact angle.

Due to the lack of available pH_{iep} at elevated temperatures, only the pH_{iep} of silica at 25 ℃ can be compared. As Fig. 6-1-2 shows, the reported silica pH_{iep} varies from 2.8 to 5.6. We believe this discrepancy may be due to the difference in the solid material, such as quartz plate, quartz powder, or silica nanoparticles. In addition, the techniques utilized to estimate pH_{iep} are varied. Furthermore, the discrepancies in the electrolyte compositions and the pH adjustment chemicals may influence pH_{iep} values. In Appendix D we present a comprehensive review of the pH_{iep} reported in literature, which includes information on conditions that may cause a difference in the obtained pH_{iep} of silica and other similar materials.

The pH_{iep} determined by the general correlation is in good agreement with the results obtained by Gusev et al. (2002), who used a similar solid material. Cuddy et al. (2013) (not shown in Fig. 6-1-2) used the same method as we did (determined the pH_{iep} via contact angle measurement), and they reported $pH_{iep}=3.9 \pm 0.5$ for a SiO_2 film on the quartz crystal microbalance (QCM) sensor.

6.2 Temperature Dependence of the Isoelectric Point

The obtained pH_{iep} via the general correlation shows a slight temperature dependence, decreasing linearly from 4.14 at 25 ℃ to 3.66 at 200 ℃. The negative temperature dependence of quartz has been reported by other researchers (Rodriguez et al., 2006; Wiśniewska, 2010). However, the slope of our results (-0.029 pH units per 10 ℃) is lower than other reported results. The slope was found to be -0.0125 pH units per 10 ℃ from 15 ℃ to 35 ℃ by Wiśniewska (2010) and -0.124 pH units per 10 ℃ from 20 ℃ to 45 ℃ by Rodriguez et al. (2006).

Bérubé et al. (1968) derived the following thermodynamic relation for oxide surfaces in which the isoelectric point depends on temperature:

$$4.6R\left[0.5\, pK_{\mathrm{w}} - \mathrm{pH_{iep}}\right] = \frac{\Delta H^*}{T} - \Delta S^*, \qquad (6\text{-}2\text{-}1)$$

where R is the molar gas constant (8.314 J mol^{-1} K^{-1}), K_{w} is the water ionization constant, and ΔH^* and ΔS^* are the standard enthalpy change and entropy change for transferring the potential-

determined ions from the bulk solution to the interfacial region at the isoelectric point, respectively, J mol^{-1}.

Bérubé et al. (1968) calculated the values of temperature-independent terms ΔH^* and ΔS^* from the slope and the intercept of the $1/T$ vs. $0.5\ (pK_w - \mathrm{pH_{iep}})$ curve. In their work, the isoelectric point of the solid material, was experimentally obtained. Therefore, to determine the values of ΔH^* and ΔS^* for silica, the $\mathrm{pH_{iep}}$ at a temperature different from that of room temperature was needed. The calculated ΔH^* and ΔS^* are 9580.32 J/mol and -76.67 J/mol, respectively (Appendix C).

A comparison of the silica $\mathrm{pH_{iep}}$ obtained by the general correlation and by the method suggested by Bérubé et al. (1968) is shown in Fig. 6-2-1. It can be seen that the $\mathrm{pH_{iep}}$ resulting from the general correlation shows a weaker temperature dependence. This difference may be due to the applicable temperature range and the oxide type to be used for Eq. (6-2-1). In addition, it has been reported that for some solid materials, the slope of the $\mathrm{pH_{iep}}$ vs. *t* curve decreases when the temperature is higher than 100 ℃ and even reverses (i.e., $\mathrm{pH_{iep}}$ shows a positive temperature dependence) when the temperature is around 300 ℃ (Schoonen, 1994). In addition, by referring to the phase diagram of quartz (Aasly et al., 2007; Kayama et al., 2018), we can observe that the phase of silica was in a stable region (*a*-quartz phase). In other words, our experimental quartz is free from the impact of phase transformation. Therefore, the high pressure (1000 psi) in our experiment could only change the suspension ordering at the quartz/aqueous phase interface, and such a change is in a monotonic direction (Rodriguez et al., 2006). Fig. 6-2-2 shows the experimental results from Rodriguez et al. (2006). These results show that the isoelectric point of quartz beomes larger in relation to pH values as the pressure rises. Therefore, the high pressure may have led to the slighter temperature dependence of silica $\mathrm{pH_{iep}}$ in our experiments, More investigation is needed to understand the mechanism by which pressure influences temperature dependence of $\mathrm{pH_{iep}}$.

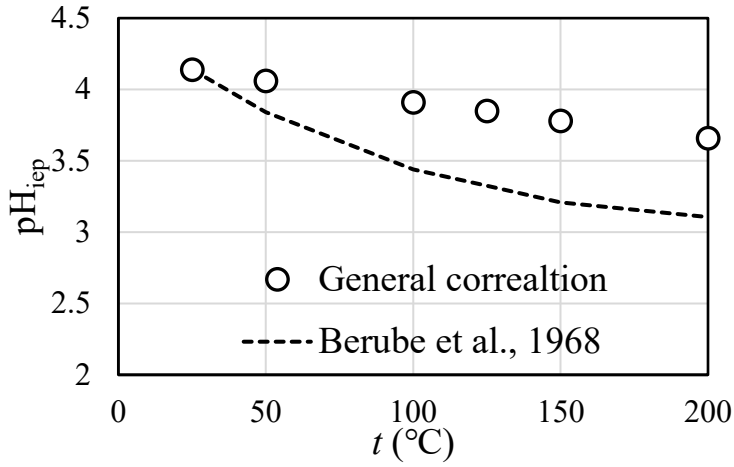

Fig. 6-2-1. pH_{iep} obtained from different approaches at different temperatures.

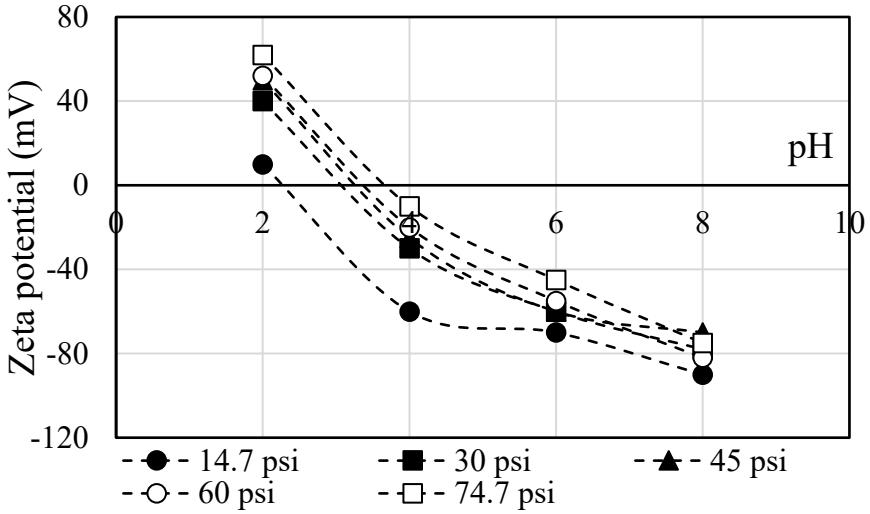

Fig. 6-2-2. Zeta potential of quartz at 20 °C and different pressures (quartz from Brazil/0.01 M NaCl(aq)/air), reproduced from Fig. 3 by Rodriguez et al. (2006).

Chapter 7 Verification of the Experimental Results

In this chapter, we discuss in more detail the surface tension component (STC) method that we briefly introduced in Chapter 2. Then, we compare our experimental results with the results theoretically calculated results using the STC method.

The STC method divides the surface energy into two different parts, the non-polar Lifshitz-Van der Waals (LW) contribution and the polar Lewis acid-base (AB) one:

$$\gamma = \gamma^{\mathrm{LW}} + \gamma^{\mathrm{AB}}. \tag{7-1}$$

In Eq. (7-1), the Lifshitz-Van der Waals component, γ^{LW}, is the result of non-polar interactions such as dispersion forces. For example, the Lifshitz-Van der Waals contribution to the interfacial tension at the quartz/water interface can be written as:

$$\gamma_{\mathrm{q-w}}^{\mathrm{LW}} = (\sqrt{\gamma_{\mathrm{q}}^{\mathrm{LW}}} - \sqrt{\gamma_{\mathrm{w}}^{\mathrm{LW}}})^2 = \gamma_{\mathrm{q}}^{\mathrm{LW}} - \gamma_{\mathrm{w}}^{\mathrm{LW}} + 2\sqrt{\gamma_{\mathrm{q}}^{\mathrm{LW}}\gamma_{\mathrm{w}}^{\mathrm{LW}}}, \tag{7-2}$$

where $\gamma_{\mathrm{q}}^{\mathrm{LW}}$ and $\gamma_{\mathrm{w}}^{\mathrm{LW}}$ are the LW components of the surface tension on the quartz surface and the water surface, respectively.

Based on Eq. (7-1), if the value of $\gamma_{\mathrm{q}}^{\mathrm{LW}}$ and $\gamma_{\mathrm{w}}^{\mathrm{LW}}$ can be obtained, we can calculate $\gamma_{\mathrm{qw}}^{\mathrm{LW}}$. Israelachvili (1985) suggested using the following equation to calculate the LW component of the surface tension for a single phase *i*:

$$\gamma_i^{\mathrm{LW}} = \frac{A_H}{24\pi d_0^2}, \tag{7-3}$$

where A_H is the Hamaker constant (in J), which can be defined for the Van der Waals interaction between two materials. d_0 represents the separation distance between the two nearest molecules of the same phase, which is usually in the order of 10^{-10} m (Duffy et al., 2021).

The Lewis acid-based component γ^{AB} is not theoretically derived according to the basic properties of different materials. Instead, it is treated more like empirical parameters. Oss et al. (2006) believed that the single phase has electron-accepting (γ_i^+) and electron-donating strength (γ_i^-) and that these two strengths determine γ^{AB} of the single phase by the following equation:

$$\gamma_i^{AB} = 2\sqrt{\gamma_i^+ \gamma_i^-}. \tag{7-4}$$

With the acid-base component of the single phase obtained, the acid-base component of the interfacial tension (e.g., quartz/water interfacial tension) can be calculated as follows:

$$\gamma_{q-w}^{AB} = 2\left(\sqrt{\gamma_q^+ \gamma_q^-} + \sqrt{\gamma_w^+ \gamma_w^-} - \sqrt{\gamma_q^+ \gamma_w^-} - \sqrt{\gamma_w^+ \gamma_q^-}\right). \tag{7-5}$$

7.1 Temperature Effect on γ^{LW} and γ^{AB} at Neutral pH

According to Eq. (7-1), to calculate the LW component of a single phase, A_H and d_0 are needed. Duffy et al. (2021) reported the values of A_H and d_0 for quartz, water, and n-decane (Table 7-1-1). By substituting the calculated A_H and d_0 into Eq. (7-3), we can obtain the value of γ_i^{LW} for the single phase. In this way, the LW component of the interfacial tension can be calculated. The calculated results are listed in Table 7-1-2.

For the non-polar n-decane, both $\gamma_{nC_{10}}^+$ and $\gamma_{nC_{10}}^-$ are zero. Duffy et al. (2021) fitted the temperature dependence of γ_q^+, γ_q^-, γ_w^+, and γ_w^- by different quadratic equations. According to their fitted results, the value of the AB components of the interfacial tension on the interfaces are listed in Table 7-1-2.

Once all the LW and AB components have been obtained at different temperatures and neutral pH, the contact angle can be calculated based on Young's equation. A comparison between the contact angle calculated via the STC method and the experimentally measured contact angle is shown in Fig. 7-1-1. A good agreement between the calculated results and the experimental results can be observed, which demonstrates the applicability of the STC method to our experimental system.

Table 7-1-1 A_H and d_0 of different phases from 25 ℃ to 200 ℃. q denotes quartz, w denotes water, and nC_{10} denotes n-decane. Reproduced based on the results by Duffy et al. (2021).

t (℃)	$A_{H,\mathrm{q}}$ (10^{-21} J)	$A_{H,\mathrm{w}}$ (10^{-21} J)	$A_{H,\mathrm{nC_{10}}}$ (10^{-21} J)	$d_{0,\mathrm{q}}$ (10^{-10} m)	$d_{0,\mathrm{w}}$ (10^{-10} m)	$d_{0,\mathrm{nC_{10}}}$ (10^{-10} m)
25	65.5	39.3	48.2	1.65	1.57	1.65
50	65.5	38.2	46.0	1.65	1.57	1.70
75	65.6	37.1	43.8	1.65	1.59	1.76
100	65.7	36.0	41.6	1.65	1.62	1.83
125	65.7	34.8	39.5	1.65	1.66	1.92
150	65.8	33.6	37.4	1.65	1.71	2.01
175	65.8	32.4	35.4	1.65	1.77	2.12
200	65.9	31.2	33.5	1.65	1.85	2.25

Table 7-1-2 Liftshitz-Van der Waals component of the interfacial tension at different interfaces. Reproduced based on the results by Duffy et al. (2021).

t (℃)	$\gamma^{\mathrm{LW}}_{\mathrm{q-w}}$ (mN/m)	$\gamma^{\mathrm{LW}}_{\mathrm{q-nC_{10}}}$ (mN/m)	$\gamma^{\mathrm{LW}}_{\mathrm{w-nC_{10}}}$ (mN/m)	$\gamma^{\mathrm{AB}}_{\mathrm{q-w}}$ (mN/m)	$\gamma^{\mathrm{AB}}_{\mathrm{q-nC_{10}}}$ (mN/m)	$\gamma^{\mathrm{AB}}_{\mathrm{w-nC_{10}}}$ (mN/m)
25	1.11	0.63	0.07	-15.90	31.85	49.96
50	1.27	1.10	0.01	-14.41	28.54	47.66
75	1.53	1.74	0.01	-12.80	24.95	44.73
100	1.91	2.56	0.05	-11.08	21.21	41.31
125	2.42	3.55	0.11	-9.25	17.45	37.54
150	3.07	4.68	0.17	-7.29	13.80	33.54
175	3.86	5.93	0.22	-5.18	10.43	29.41
200	4.79	7.27	0.26	-2.88	7.54	25.28

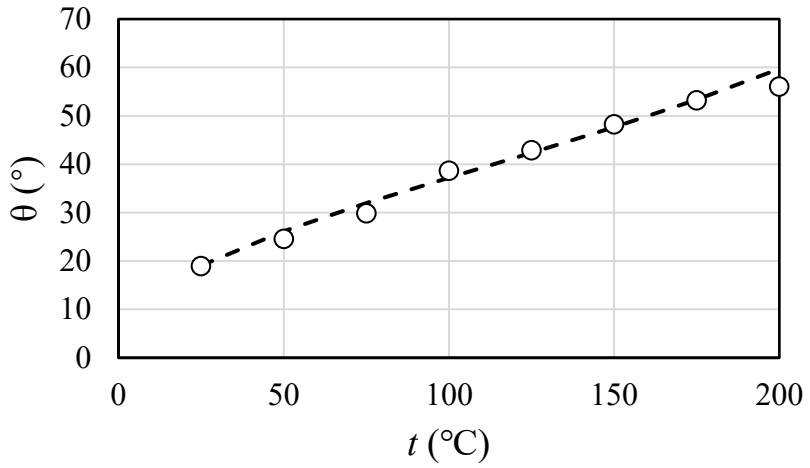

Fig. 7-1-1. Contact angle obtained via the STC method (dashed line) and our experiments (white dots) at different temperatures.

Both γ^{LW} and γ^{AB} are functions of temperature. The temperature dependence of the surface tension components of water and quartz is shown in Fig. 7-1-2. In each of plots, the AB components change significantly with temperature, while the LW components vary only slightly (there is almost no change for quartz). The variation trend in γ_w^{AB} suggests that the number and strength of hydrogen bonds in water decrease as the temperature increases.

We observed negative γ_{q-w}^{AB} values in Table. 7-1-2, a negative surface energy value suggested that adsorption on a solid surface is typically an exothermic process (Mathur et al., 2005), and the exothermic process decreases the surface energy. A negative surface energy value will be observed if the adsorption is strong enough. Therefore, the negative value of γ_{q-w}^{AB} indicates a strengthened interaction between water and quartz via the hydrogen bonds. This kind of interaction is weakened as the temperature rises, and the quartz surface becomes less water-wet.

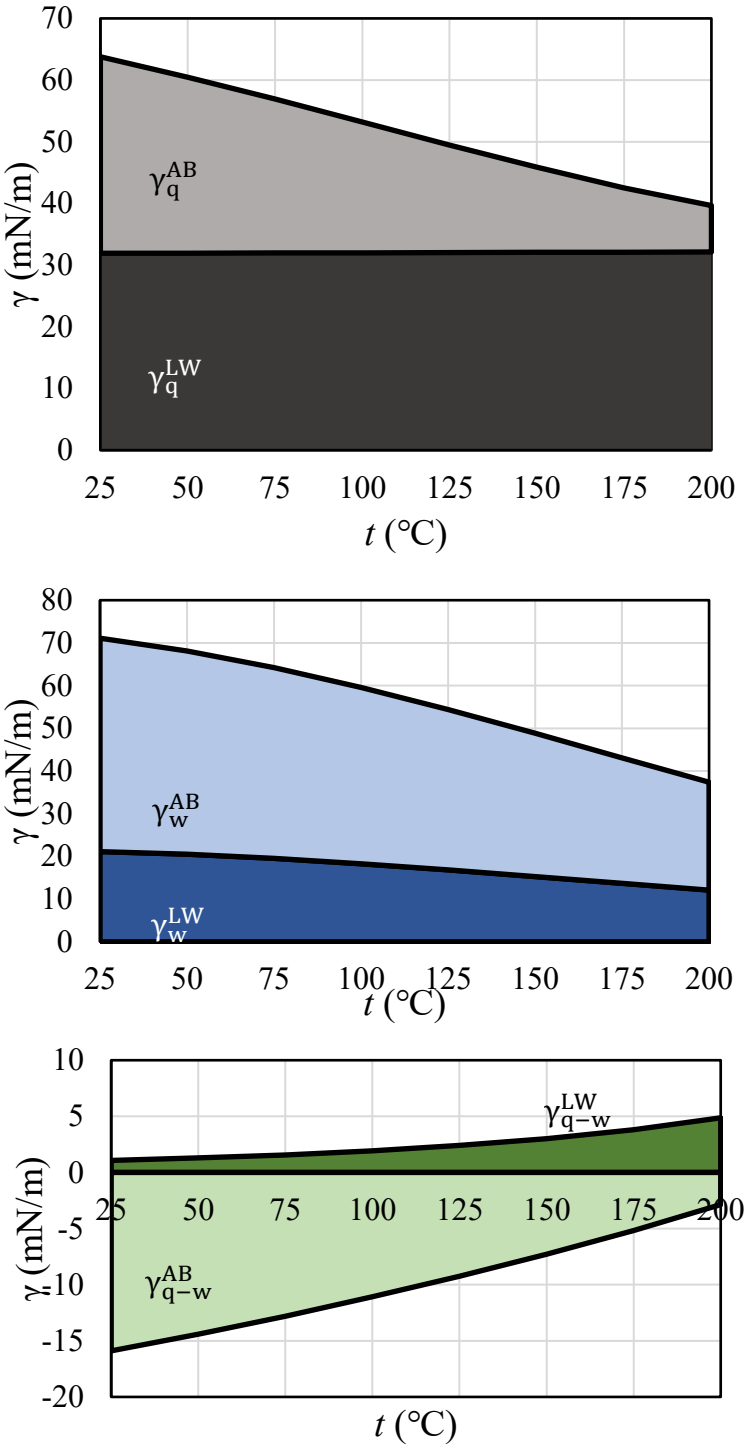

Fig. 7-1-2. Temperature effect on surface tension components. Reproduced based on the results by Duffy et al. (2021).

7.2 pH Effect on γ^{LW} and γ^{AB} at Different Temperatures

In the STC method, the variation in pH leads only to a change in γ^{AB}. The Lifshitz-Van der Waals component is determined by temperature and the distance between two adjacent molecules. In a three-phase system, hydrogen-bonds are formed between the surface group (e.g., silanol groups) and the pH-determined ions in the aqueous phase. Changes in pH alter the number and type of the surface groups (Chapter 5), as well as the concentration of H^+(aq) and OH^-(aq). Therefore, the total polar interaction between the surface and the aqueous phase is varied.

In our experimental system, $\gamma^{AB}_{nC_{10}}$ always equals zero since the n-decane is always non-polar. γ^{AB}_{W} is also independent of pH. For instance, in an acidic solution where HCl(aq) is the only electrolyte, the Gibbs isotherm regarding the water phase can be written as:

$$-\frac{d\gamma_w}{RT} = \Gamma_{OH^-(aq)} d\ln a_{OH^-(aq)} + \Gamma_{H^+(aq)} d\ln a_{H^+(aq)} + \Gamma_{Cl^-(aq)} d\ln a_{Cl^-(aq)}, \quad (7\text{-}2\text{-}1)$$

where $\Gamma_{i(aq)}$ is the surface coverage of the ion *i*, mol m^{-2}. $a_{i(aq)}$ is the activity of the ion *i*.

Beattie et al. (2014) believed that the adsorption of the Cl^-(aq) ion is negligible. In that case, Eq. (7-2-1) can be rewritten as:

$$-\frac{d\gamma_w}{RT} = \Gamma_{OH^-(aq)} d\ln a_{OH^-(aq)} + \Gamma_{H^+(aq)} d\ln a_{H^+(aq)} = \Gamma d\ln K_W. \quad (7\text{-}2\text{-}2)$$

In Eq. (7-2-2), γ_w is defined by water ionization constant K_W, which is a function of temperature instead of pH. Therefore, in our experimental system, γ^+_q and γ^-_q are functions of pH while γ^+_w, γ^-_w, $\gamma^+_{nC_{10}}$, and $\gamma^-_{nC_{10}}$ are not.

The available literature in regards to the pH dependence of γ^+_q and γ^-_q is limited. Arsalan et al. (2013) utilized Ottawa sand (99% quartz) for their sample, and they reported the values of γ^+_q and γ^-_q at 30, 50 and 80 °C. Duffy et al. (2021) reported the following equation based on the results from Arsalan et al. (2013):

$$\sqrt{\gamma_q^+/\gamma_q^-} = 0.453 * 0.990^t. \quad (7\text{-}2\text{-}3)$$

Considering the specificity of different materials, for our system, Eq. (7-2-3) was corrected as:

$$\sqrt{\gamma_q^+/\gamma_q^-} = 0.677 * 0.995^t. \quad (7\text{-}2\text{-}4)$$

Then, based on the experimentally obtained contact angle data given in Section 5.2, using Eq. (7-2-4), we can calculate γ_q^+ and γ_q^- at different pH values and temperatures. The calculated γ_q^+ and γ_q^- values are listed in Table 7-2-1. The following equations are fitted based on the calculated results:

$$\gamma_q^+ \left(\frac{\mathrm{mN}}{\mathrm{m}}\right) = 1.282 \times 10^{-4}\, t^2 - 0.076\, t + 0.014\, \mathrm{pH}^2 - 0.1343\, \mathrm{pH} + 11.72, \quad (7\text{-}2\text{-}5)$$

$$\gamma_q^- \left(\frac{\mathrm{mN}}{\mathrm{m}}\right) = 3.841 \times 10^{-4}\, t^2 + 0.032\, t + 0.065\, \mathrm{pH}^2 - 0.588\, \mathrm{pH} + 26.7. \quad (7\text{-}2\text{-}6)$$

The R^2 values of Eq. (7-2-5) and (7-2-6) are 0.99 and 0.92, respectively. Fig. 7-2-1 shows the contact angles calculated based on the STC method vs. this study's experimentally obtained values.

Table 7-2-1 The calculated γ_q^+ and γ_q^- at different temperatures and pH values.

t (℃)	pH	γ_q^+ (mN/m)	γ_q^- (mN/m)	*t* (℃)	pH	γ_q^+ (mN/m)	γ_q^- (mN/m)
	2.05	9.74	27.07		2.06	4.14	24.60
	4.01	9.41	26.14		4.01	3.71	22.05
25	6.99	9.62	26.73	125	5.94	3.78	22.46
	9.96	9.83	27.32		7.91	4.24	25.18
	11.92	9.87	27.42		9.82	4.39	26.10
	2.05	8.39	27.34		2.06	2.96	21.49
	4.01	8.07	26.28		4.01	2.67	19.37
50	6.62	8.22	26.77	150	5.81	2.75	19.98
	9.23	8.52	27.77		7.60	3.18	23.06
	11.19	8.60	28.01		9.55	3.22	23.41
	2.05	5.42	26.37		2.07	1.58	17.11
	4.01	4.92	23.93		4.01	1.43	15.53
100	6.12	4.96	24.11	200	5.64	1.37	14.88
	8.22	5.50	26.74		7.27	1.71	18.49
	10.18	5.64	27.44		9.21	1.80	19.47

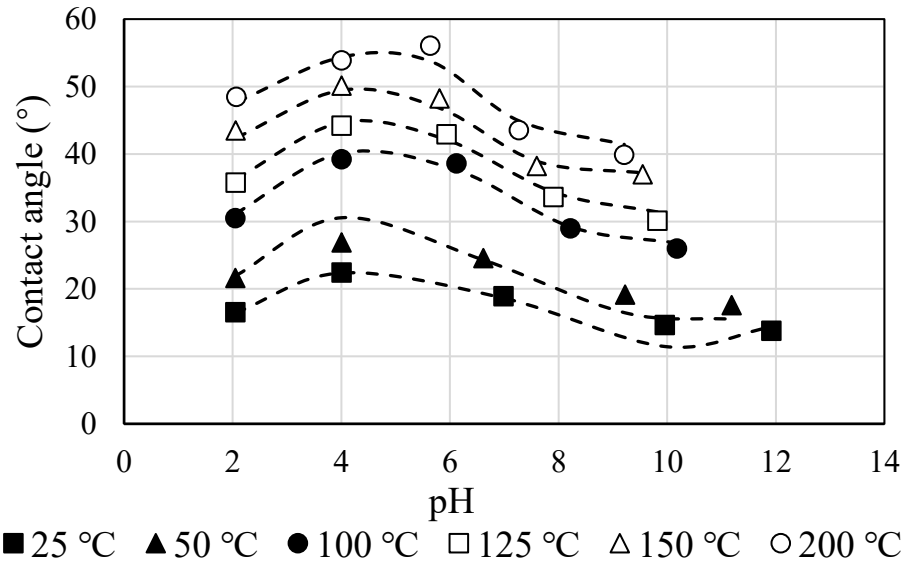

Fig. 7-2-1. Contact angle obtained via the STC method (dashed line) vs. the experimental values (shapes) at different temperatures.

The pH dependence of γ_q^{AB} and γ_{q-w}^{AB} are shown in Fig. 7-2-2 and 7-2-3, respectively. It Note that the pH effect on the hydrogen bonds is much smaller than the temperature effect. The hydrophilicity of the silica surface stems from its hydrogen-donating and hydrogen-accepting ability (Schrader et al., 2017), which is reflected in the pH dependence of γ_q^{AB} in Fig. 7-2-2. Considering the protonation and deprotonation of the surface hydroxyl group introduced in Chapter 5, the number of Si-OH groups reaches its maximum at pH_{iep}. Iler (1978) reported that hydrogen bond formation is irrelevant with SiO^- groups, which may have implications for the $SiOH_2^+$ groups as well. In our experimental system, complex hydrate complexes are formed due to the hydrogen bonds between the quartz surface and water molecules in the aqueous phase. The association can produce several layers of water on the surface or surrounding the solute ion. The strongly hydrated surface will exert a repulsion force between quartz and water because of the energy required for perturbation of the ordered structure of the bound layers of water molecules (Donaldson et al., 2008). Therefore, the magnitude of γ_{q-w}^{AB} drops since the hydration force has increased the repulsion between the quartz surface and the aqueous phase. However, for other mineral surfaces, the functional group may be varied, and a more comprehensive understanding of the polar interactions between the surface (groups) and the aqueous solution is needed. In particular, more studies are needed to obtain the AB components based on the intrinsic properties of materials rather than empirical treatments.

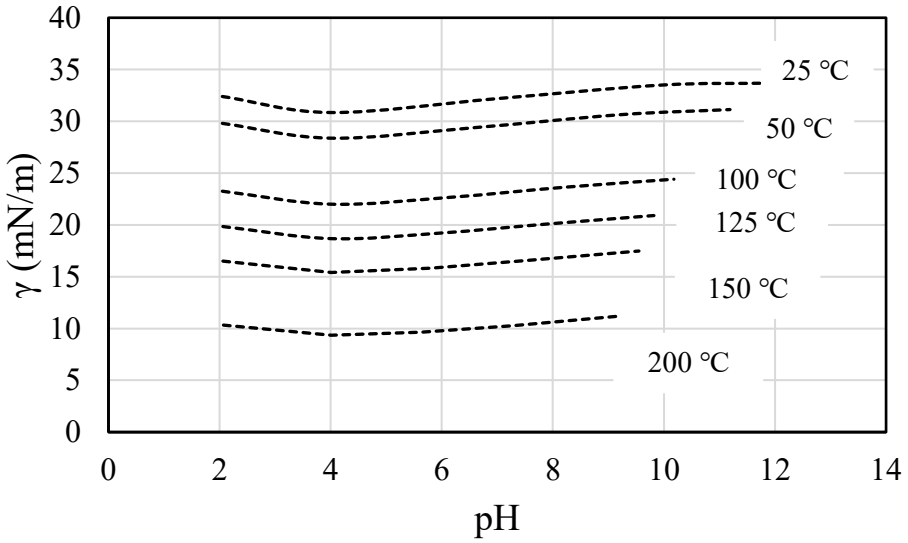

Fig. 7-2-2. pH dependence of the acid-base component of the surface tension on the quartz ($\boldsymbol{\gamma_q^{AB}}$) surface at different temperatures.

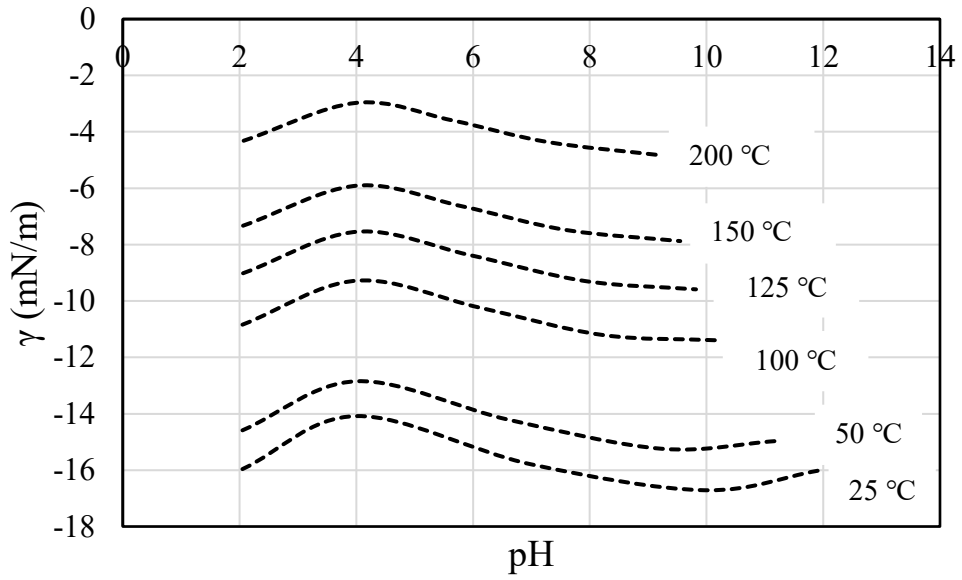

Fig. 7-2-3. pH dependence of the acid-base component of the interfacial tension on the quartz-water ($\boldsymbol{\gamma_{q-w}^{AB}}$) interface at different temperatures.

Chapter 8 Conclusion

In this study, e have developed a new capillary-based system for contact angle measurement. The system is the first capillary-based technique that enables researchers to study dynamic contact angles in a solid/liquid/liquid (e.g. quartz capillary/water/n-decane) system at high temperatures and pressures up to 200 ℃ and 69 bar. The experimental design provides an inexpensive method of studying interfacial phenomena as a function of temperature, pH, pressure, salt type, concentration, and other parameters with controlled flow rate and geometry, thereby opening up new opportunities for fundamental wettability studies. Our work suggests the following conclusions can be generated:

1. The surface roughness of the capillary tube was assumed as 1. The contact angles were measured at three consistent locations on each side of the capillary. Meanwhile, the contact angle at each position were measured several times by injecting DI water and n-decane into the system. The average standard deviation of the measured contact angles at these locations for the entire experiment is around 1.2°.

2. At the neutral pH, the measured capillary/DI water/n-decane contact angle in the new system increased linearly by 1.1° for every 5 °C within the temperature range 25–200 °C. This indicates that the quartz shifted from water-wet (18.9°) to weak water-wet (56.1°) as the temperature increaseed.

3. The temperature dependence of the quartz/water/n-decane contact angles could not be sufficiently explained by viscous forces or interfacial tension (at the n-decane/water interface) changing as a function of temperature. Changes to solid/liquid and solid/oil adhesions, which are influenced by the Van der Waals dispersion type and polar/acid-base type interfacial forces, may also be responsible for the temperature dependence of the contact angles.

4. Except for neutral-pH DI water, we have experimentally studied the contact angle of a single system within a 2-12 pH range at a temperature range from 25 to 200 °C. The temperature and pressure effects on the pH value of the aqueous HCl(aq) and NaOH(aq) were considered. Our calculated results suggest that the pH of the a single aqueous solution drops as the temperature rises. However, this does not indicate that the solution becomes more acidic. In fact, due to the increase in the ionization constant of water at higher temperatures, the scale of the neutral pH moves to a smaller pH value.

5. The obtained results suggest that there is a concave parabolic relation between θ and pH at a constant temperature. The system became less water-wet as the pH increased from the acidic

region. The maximum θ was observed at the isoelectric point of quartz, pH_{iep}. The system became more water-wet as the pH rose.

6. The pH dependence of the contact angles can be explained by the Zeta potential of quartz. The magnitude of Zeta potential is positively correlated with the electrostatic repulsion between the quartz surface and n-decane in bulk due to the fact that the quartz surface is hydrophilic. The magnitude of Zeta potential is related to the quartz surface reactions. Corresponding to the increase in the pH from the acidic region to the basic region, the Zeta potential of quartz changed from slightly positive to significantly negative. pH_{iep} is the pH value at which Zeta potential equals zero. Hence, the weakest repulsion and the maximum θ (θ_{iep}) are found at pH_{iep}.

7. The significant discrepancy between the results calculated using model by Amadu et al. (2019) and the experimentally-measured results in our work suggests that γ_{sw} is not the only pH-dependent terms. The pH effects on both solid/liquid and liquid/liquid interactions should be taken into account. In addition to the previously mentioned pH-independent assumption, the lack of background electrolyte solutions such as NaCl(aq) might be another reason for the inconsistency in our experiment.

8. We used the quadratic fit, the cubic fit, and a general correlation as the analytical equations for our experimental results. The results suggest that the general correlation has a high R^2 value, and the obtained pH_{iep} is in good agreement with the data found in the available literature based on a similar material (fused silica) and method (contact angle measurement). The empirical general correlation considers the effects of pH and temperature simultaneously, which is not commonly found in the theoretical or empirical equations reported in other studies.

9. The contact angles calculated via the STC method are in good agreement with our experimental results. The increase in temperature lowers both polar and nonpolar interactions between quartz and water, and the variation in the polar interactions is more significant because the strength of hydrogen bonds weakens as the temperature increases. The pH only affects the polar interactions, whereas the hydration force increases the repulsion between the quartz surface and the aqueous phase. The calculated results suggest that the pH effect on the polar interactions is slight compared to the effect of the temperature. More research on how to determine the AB components from the intrinsic properties of the material is needed.

Chapter 9 Future Work Recommendation

In this work, we experimentally studied the effects of temperature and pH on the contact angle in a quartz/water/n-decane system. In future research, the system components could be changed, (e.g., from quartz to calcite, from water to NaCl(aq), from n-decane to crude oil). The influences of other parameters including pressure, salt concentration, and the diameter of the capillary could be studied as well.

We employed Young's model in this work. The Young's model might be extended to the disjoining pressure model or surface group model. We also assumed the surface roughness as 1 in this work. In future works, the surface roughness and heterogeneity of different solid surfaces might be taken into consideration by using the Wenzel model or the Cassie-Baxter model.

Using the STC method, we predicted the surface tension components of the different phases in our experiment. The polar acid-base surface tension components were not theoretically obtained from the properties of the materials themselves. Instead, they were treated as empirical constants. Future works might focus on polar interactions at the phase interface (e.g., hydrogen bonds) and develop relevant analytical models that can be used to understand and predict variation in the polar interactions.

Appendix A Calculation of pH at the Experimental Conditions

The association in the HCl(aq) and NaOH(aq) solution can be written as follows:

$$\mathrm{H^+(aq) + Cl^-(aq) \rightarrow HCl(aq)} \quad K_A[\mathrm{HCl(aq)}], \tag{A-1}$$

$$\mathrm{Na^+(aq) + OH^-(aq) \rightarrow NaOH(aq)} \quad K_A[\mathrm{NaOH(aq)}], \tag{A-2}$$

where $K_A[\mathrm{HCl(aq)}]$ and $K_A[\mathrm{NaOH(aq)}]$ are the association constant of HCl(aq) and NaOH(aq), respectively. The association constant indicates the degree of the association of the ion pairs:

$$K_A[\mathrm{HCl(aq)}] = \frac{b_{\mathrm{HCl(aq)}}}{b_{\mathrm{H^+(aq)}} * b_{\mathrm{Cl^-(aq)}}}, \tag{A-3}$$

$$K_A[\mathrm{NaOH(aq)}] = \frac{b_{\mathrm{NaOH(aq)}}}{b_{\mathrm{Na^+(aq)}} * b_{\mathrm{Na^+(aq)}}}. \tag{A-4}$$

As the inverse of dissociation, the degree of the association will be influenced by temperature as well, and it can be reflected by K_A. The following equation was suggested to calculate K_A at different temperatures (Lvov et al., 2018):

$$\Delta \mathrm{G}^0_{j,ionpair}(T,P) = \sum \Delta \mathrm{G}^0_{j,ions}(T,P) + RT \ln K_A, \tag{A-5}$$

where $\Delta \mathrm{G}^0_{j,ionpair}(T,P)$ is the summation of standard Gibbs energy values of ions from the association reaction (J mol^{-1}), $\Delta \mathrm{G}^0_{j,ionpair}(T,P)$ is the standard Gibbs energy values of the resulting ion pair (J mol^{-1}). The relevant $\Delta \mathrm{G}^0_{j,ionpair}(T,P)$ and $\Delta \mathrm{G}^0_{j,ions}(T,P)$ values regarding the association of HCl(aq) and NaOH(aq) solution are listed in Table A-1.

Table A-1 Data of the apparent Gibbs energy of formation for different species at different temperatures and pressures. Reproduced from Table B.2 and Table B.3 by Lvov et al. (2018).

T (K)	P (bar)	$\Delta G^0_{NaOH^0(aq),j}$ (kJ mol^{-1})	$\Delta G^0_{HCl^0(aq),j}$ (kJ mol^{-1})	$\Delta G^0_{Na^+(aq),j}$ (kJ mol^{-1})	$\Delta G^0_{OH^-(aq),j}$ (kJ mol^{-1})	$\Delta G^0_{H^+(aq),j}$ (kJ mol^{-1})	$\Delta G^0_{Cl^-(aq),j}$ (kJ mol^{-1})
298.15	1	-421.9	-134.4	-261.9	-157.3	0	-131.3
323.15	1	-422.5	-137.1	-263.4	-156.9	0	-132.6
373.15	1.0132	-424.3	-140.1	-266.7	-155.6	0	-134.6
398.15	2.3202	-425.5	-140.5	-268.5	-154.6	0	-135.3
423.15	4.7572	-426.9	-140.2	-270.3	-153.5	0	-135.8
473.15	15.5365	-430.3	-137.3	-274.2	-150.5	0	-136.0

According to the same reference, the average ΔG^0_j change with the pressure is -3.26, -11.43, -0.60, -6.62, 0 and -4.02 J mol^{-1} bar $^{-1}$ for NaOH(aq), HCl(aq), Na^+(aq), OH^-(aq), H^+(aq) and Cl^-(aq), respectively. We used linear extrapolations to determine the values of ΔG^0_j under our experimental conditions. In our experiments, the pressure was held constant as 1000 psi.Taking NaOH(aq) at 298.15 K and 69 bar as an example:

$$\Delta G^0_{NaOH(aq),j}(298.15\ \text{K}, 69\ \text{bar}) = \Delta G^0_{NaOH(aq),j}(298.15\ \text{K}, 1\ \text{bar}) - 3.256 \times (69-1) = -421.9 - 3.256 \times 68 = -422.1\ \text{kJ/mol}. \quad \text{(A-6)}$$

Similarly, ΔG^0_j of other species can be calculated, and the obtained results are listed in Table A-2.

Table A-2 The calculated ΔG^0_j for different species at the experimental conditions.

t (°C)	P (bar)	$\Delta G^0_{NaOH^0(aq),j}$ (kJ/mol)	$\Delta G^0_{HCl^0(aq),j}$ (kJ/mol)	$\Delta G^0_{Na^+(aq),j}$ (kJ/mol)	$\Delta G^0_{OH^-(aq),j}$ (kJ/mol)	$\Delta G^0_{H^+(aq),j}$ (kJ/mol)	$\Delta G^0_{Cl^-(aq),j}$ (kJ/mol)
25	69	-422.1	-135.1	-261.9	-157.7	0	-131.6
50	69	-422.7	-137.8	-263.4	-157.4	0	-132.9
100	69	-424.5	-140.7	-266.8	-156.1	0	-134.9
125	69	-425.7	-141.3	-268.5	-155.1	0	-135.6
150	69	-427.1	-140.9	-270.4	-153.9	0	-136.0
200	69	-430.4	-137.9	-274.3	-150.8	0	-136.2

Then, with the calculated values above, the association constants can be obtained with Eq. (A-5), taking $K_A[\mathrm{HCl(aq)}]$ at 298.15 K (25 °C) and 69 bar as an example:

$$K_A[\mathrm{HCl(aq)}, 298.15\ \mathrm{K}, 69\ \mathrm{bar}] = \exp\left[\frac{\Delta G^0_{\mathrm{HCl^0\,(aq)},j}(298.15\ \mathrm{K},69\ \mathrm{bar}) - \Delta G^0_{\mathrm{Cl^-(aq)},f}(298.15\ \mathrm{K},69\ \mathrm{bar}) - \Delta G^0_{\mathrm{H^+(aq)},f}(298.15\ \mathrm{K},69\ \mathrm{bar})}{RT}\right] = \exp\left[\frac{-135135.69-(-131563.12)-0}{8.314\times 298.15}\right] = \exp(-1.441) = 0.237. \quad \text{(A-7)}$$

With the similar approach, we can calculate the values of $K_A[\mathrm{HCl(aq)}]$ and $K_A[\mathrm{NaOH(aq)}]$ at our experimental conditions (Table A-3).

Table A-3 $K_A[\mathrm{HCl(aq)}]$ and $K_A[\mathrm{NaOH(aq)}]$ at the experimental conditions.

t (°C)	P (bar)	k_A[NaOH(aq)]	k_A[HCl(aq)]
25	69	0.369	0.237
50	69	0.499	0.158
100	69	0.582	0.145
125	69	0.532	0.180
150	69	0.447	0.250
200	69	0.258	0.648

The activity coefficient can be calculated based on the Debye-Huckel theory (Lvov, 2014):

$$\ln \gamma_+ = -\frac{A_{DH} z_+^2 I_b^{0.5}}{(1+B_{DH}\mathring{a} I_b^{0.5})}, \quad \text{(A-8)}$$

$$\ln \gamma_- = -\frac{A_{DH} z_-^2 I_b^{0.5}}{(1+B_{DH}\mathring{a} I_b^{0.5})}, \quad \text{(A-9)}$$

$$\ln \gamma_\pm = -\frac{A_{DH} |z_+ z_-| I_b^{0.5}}{(1+B_{DH}\mathring{a} I_b^{0.5})}, \quad \text{(A-10)}$$

where γ_+, γ_- and $\gamma_\pm$ are the activity coefficient of cation, anion, and the mean activity coefficient of the electrolyte, respectively. z_+ and z_- are the valance of cation and anion, respectively. I_b are the ionic strength on the molal concentration scale (mol/kg), å is a model parameter, which can be taken as 4.5 Å, A_{DH} and B_{DH} are model parameters, which depend on water density (ρ_{w}), temperature, and the relative permittivity of water (ε_{w}) by the following equations (Lvov, 2021):

$$A_{\mathrm{DH}} = \frac{2.303\times1.8246\times10^{6}\times\rho_{\mathrm{w}}^{0.5}}{(\varepsilon_{\mathrm{w}}T)^{1.5}}, \tag{A-11}$$

$$B_{\mathrm{DH}} = \frac{50.29\times\rho_{\mathrm{w}}^{0.5}}{(78.44\times T)^{0.5}}. \tag{A-12}$$

According to Eq. (A-8) to (A-10), for 1-1 electrolyte solutions such as HCl(aq) and NaOH(aq), the calculated value of γ_+, γ_- and $\gamma_\pm$ is identical. Using data from Table A-4, A_{DH} and B_{DH} at 298.15 K can be calculated as:

$$A_{\mathrm{DH,298.15\ K}} = \frac{2.303\times1.8246\times10^{6}\times\rho_{\mathrm{w}}^{0.5}}{(\varepsilon_{\mathrm{w}}T)^{1.5}} = \frac{2.303\times1.8246\times10^{6}\times1^{0.5}}{(78.7\times298.15)^{1.5}} = 1.169\ (\mathrm{kg/mol})^{0.5}, \tag{A-13}$$

$$B_{\mathrm{DH,298.15\ K}} = \frac{50.29\times\rho_{w}^{0.5}}{(\varepsilon_{\mathrm{w}}\times T)^{0.5}} = \frac{50.29\times1^{0.5}}{(78.7\times298.15)^{0.5}} = 0.328\ (\mathrm{kg/mol})^{0.5}\ (\text{Å})^{-1}. \tag{A-14}$$

Similarly, we can calculate A_{DH} and B_{DH} at other temperatures; the calculated values are listed in Table A-4.

Table A-4 Different properties of water and the calculated Debye-Huckel model parameters at the experimental conditions.

t (°C)	P (bar)	ρ_w (kg/m^3) [1]	K_w [1]	ε_w	A_{DH} (kg/mol)$^{0.5}$	B_{DH} (kg/mol)$^{0.5}$ (Å)$^{-1}$
25	69	1000	13.97	78.7	1.169	0.328
50	69	991	13.24	70.2	1.224	0.332
100	69	962	12.23	55.8	1.372	0.342
125	69	942	11.88	49.7	1.465	0.347
150	69	921	11.61	44.3	1.571	0.353
200	69	869	11.28	35.0	1.838	0.364

[1] From www.energy.psu.edu/tools/ionization0730/index.php

Then, insert the calculated A_{DH} and B_{DH} values to Eq. (A-10), and we can calculate $\gamma_{\pm,b}$. Taking $\gamma_{\pm,b}$ of 0.01 mol/kg electrolytes as an example:

$$\ln\gamma_{\pm,b=0.01\ \mathrm{mol/kg},298.15\ \mathrm{K}} = -\frac{A_{\mathrm{DH},298.15\ \mathrm{K}}|z_+z_-|I_b^{0.5}}{\left(1+B_{\mathrm{DH},298.15\ \mathrm{K}}\text{å}I_b^{0.5}\right)} = -\frac{1.169\times|1\times1|\times0.01^{0.5}}{(1+0.328\times4.5\times0.01^{0.5})} = -0.10187,$$

$$\gamma_{\pm,b=0.01\ \mathrm{mol/kg},298.15\ \mathrm{K}} = \exp(-0.10187) = 0.903. \quad \text{(A-15)}$$

Similarly, $\gamma_{\pm,b}$ at other temperatures and concentrations can be obtained (Table B-5).

With the obtained K_A and $\gamma_{\pm,b}$ values, we can calculate the molality of H^+(aq) and OH^-(aq) at different temperatures and concentrations. Using 0.01 mol/kg HCl(aq) at 298.15 K as an example: first, we have a mass actions equation based on the association constant:

$$K_A[\mathrm{HCl(aq)}, 298.15\ \mathrm{K}, 69\ \mathrm{bar}] = \frac{\gamma_{\pm,b=0.01\frac{\mathrm{mol}}{\mathrm{kg}}} b_{\mathrm{HCl(aq)}}}{\gamma_{+,b=0.01\frac{\mathrm{mol}}{\mathrm{kg}}} b_{\mathrm{H^+(aq)}} \gamma_{-,b=0.01\frac{\mathrm{mol}}{\mathrm{kg}}} b_{\mathrm{Cl^-(aq)}}} = \frac{b_{\mathrm{HCl(aq)}}}{0.903\times b_{\mathrm{H^+(aq)}} b_{\mathrm{Cl^-(aq)}}} = 0.23663. \quad \text{(A-16)}$$

The second equation is the mass balance of chloride:

$$b_{\mathrm{HCl(aq)}} + b_{\mathrm{Cl^-(aq)}} = 0.01. \quad \text{(A-17)}$$

The last equation shows the charge balance:

$$b_{\mathrm{H^+(aq)}} = b_{\mathrm{Cl^-(aq)}}. \quad \text{(A-18)}$$

Solve the above three equations, and we have: $b_{\mathrm{H^+(aq)}}$=$b_{\mathrm{Cl^-(aq)}}$=9.98×10^{-3} mol/kg, and $b_{\mathrm{HCl(aq)}}$=2.14×10^{-5} mol/kg. With a similar approach, we can calculate the molality of H^+(aq) and OH^-(aq) at different temperatures (Table A-5).

The molality calculations are based on the assumption that b=10^{-2} mol/kg or b=10^{-4} mol/kg in Eq. (B-16) and (B-17). Based on the calculated results in Table B-5, the iteration was not needed. With both the mean activity coefficient and the molality of the pH-determined ions obtained, we can calculate the pH values at different temperatures. Taking 298.15 K as an example, the pH value of the 0.01 mol/kg HCl(aq) can be calculated as:

$$\mathrm{pH} = -\log\left(b_{\mathrm{H^+(aq)}} * \gamma_{\pm,b,=0.01\frac{\mathrm{mol}}{\mathrm{kg}},298.15\ \mathrm{K}}\right) = -\log(9.98 \times 10^{-3} \times 0.903) = 2.05. \quad \text{(A-19)}$$

For the 0.01 mol/kg NaOH(aq),

$$\mathrm{pH} = K_{\mathrm{w},298.5\ \mathrm{K}} - \mathrm{pOH} = K_{\mathrm{w},298.15\ \mathrm{K}} - \log\left(b_{\mathrm{OH^-(aq)}} * \gamma_{\pm,b,=0.01\frac{\mathrm{mol}}{\mathrm{kg}},298.15\ \mathrm{K}}\right) = 13.97 - [-\log(9.97 \times 10^{-3} \times 0.989)] = 11.93. \quad \text{(A-20)}$$

For the neutral pH DI water,

$$\mathrm{pH} = \frac{K_{\mathrm{w},298.15\ \mathrm{K}}}{2} = \frac{13.97}{2} = 6.99. \quad \text{(A-21)}$$

Similarly, the pH values at other temperatures and concentrations can be calculated (Table 5-2-2).

Table A-5 The mean activity coefficient of the different concentration electrolytes and the calculated molality of H^+(aq), OH^-(aq) at different temperatures.

t (℃)	$\gamma_{\pm,b=10^{-2}\ \mathrm{mol/kg}}$	$\gamma_{\pm,b=10^{-4}\ \mathrm{mol/kg}}$	$b_{\mathrm{H^+(aq)}}$ 10^{-3} mol/kg [1]	$b_{\mathrm{H^+(aq)}}$ 10^{-5} mol/kg [2]	$b_{\mathrm{OH^-(aq)}}$ 10^{-3} mol/kg [3]	$b_{\mathrm{OH^-(aq)}}$ 10^{-5} mol/kg [4]
25	0.903	0.989	9.98	10.00	9.97	10.00
50	0.899	0.988	9.99	10.00	9.96	10.00
100	0.887	0.987	9.98	10.00	9.95	10.00
125	0.880	0.986	9.98	10.00	9.95	10.00
150	0.872	0.985	9.98	10.00	9.96	10.00
200	0.852	0.982	9.95	10.00	9.98	10.00

[1] Calculated based on $\gamma_\pm$ and total concentration of 10^{-2} mol/kg HCl(aq).

[2] Calculated based on $\gamma_\pm$ and total concentration of 10^{-4} mol/kg HCl(aq).

[3] Calculated based on $\gamma_\pm$ and total concentration of 10^{-4} mol/kg NaOH(aq).

[4] Calculated based on $\gamma_\pm$ and total concentration of 10^{-2} mol/kg NaOH(aq).

Appendix B Calculate the Contact Angle via the Method by Amadu et al. (2019)

As we briefly introduced in Chapter 5, the following equation was derived by Amadu et al. (2019) to calculate the contact angle in a three-phase system:

$$\cos\theta = \left(\cos\theta_{\mathrm{iep}} + 0.5\xi\ \mathrm{pH}_{\mathrm{iep}}^2\right) - \xi \mathrm{pH}_{\mathrm{iep}}\ \mathrm{pH} + 0.5\xi\ \mathrm{pH}^2. \quad \text{(B-1)}$$

When the concentration is less than 1.5 M, the relative permittivity of the electrolyte solution can be calculated by (Gavish et al., 2016):

$$\varepsilon = \varepsilon_{\mathrm{w}} - ac. \quad \text{(B-2)}$$

According to Molina et al. (2011) and Li et al. (2017), the phenomenological ion-specific parameter, a, was obtained as 4.443 Å and 2.189 Å for HCl(aq) and NaOH(aq), respectively. Then, the molarity of 0.01 mol/kg HCl(aq) at 298.15 K can be calculated as (Lvov, 2014):

$$c_{\mathrm{HCl(aq),298.15\ K}} = \frac{\rho_{\mathrm{HCl(aq),298.15\ K}} b_{\mathrm{HCl(aq)}}}{1000 + M_{\mathrm{HCl(aq)}} b_{\mathrm{HCl(aq)}}} = \frac{1000.269 \times 0.01}{1000 + 36.458 \times 0.01} = 0.01\ \mathrm{mol/L}. \quad \text{(B-3)}$$

The density of HCl(aq) was calculated based on the data reported by Sharygin et al. (1997). $M_{\mathrm{HCl(aq)}}$ is the molar mass of the solute HCl(l), 36.458 g/mol.

Then, we can calculate the dielectric constant of the HCl(aq) solution:

$$\varepsilon_{\mathrm{HCl(aq),298.15\ K}} = \varepsilon_{\mathrm{w,298.15\ K}} - \alpha c = 78.7 - 4.443 \times 0.554 \times 10^{-3} = 78.66. \quad \text{(B-4)}$$

The number density of the HCl(aq) solution can be obtained by the following equation:

$$n = cN_A = 2 \times 0.01 \times 6.02 \times 10^{26} = 1.204 \times 10^{25}\ \mathrm{L}^{-3}. \quad \text{(B-5)}$$

Therefore, the ξ term can be calculated:

$$\xi_{\mathrm{HCl(aq),298.15\ K}} = \frac{e}{k_B T \gamma_{\mathrm{ow}}}\left[\frac{n k_B T \varepsilon_{\mathrm{HCl(aq),298.15\ K}}}{2\pi}\right]^{0.5}\left(\frac{2.303 k_B T}{e}\right)^2 = \frac{1.062\times10^{-19}}{1.38\times10^{-23}\times298.15\times50.0263}\left[\frac{1.204\times10^{25}\times1.381\times10^{-23}\times298.15\times78.66\times8.85\times10^{-12}4}{2\pi}\right]^{0.5}\left(\frac{2.303\times298.15\times50.2514}{1.062\times10^{-19}}\right)^2 = 2.147\times10^{-3}. \quad \text{(B-6)}$$

The calculated $\xi_{\mathrm{NaOH(aq),298.15\ K}}$ is 2.147×10^{-3} for 0.01 mol/kg NaOH(aq) as well. Then, what we need are $\mathrm{pH_{pzc}}$ and θ_{pzc}. For fused SiO_2(s), Gusev et al. (2002) reported it as 4. Based on our investigation, the most similar three-phase system with available contact angle data was from Barranco et al. (1997), and they reported a 27° maximum contact angle for quartz/water/trichloroethylene at 298.15 K, with 0.01 M $NaClO_4$(aq) as background solution.

Thus, we can plug the calculated parameters back to Eq. (B-1):

$$\cos\theta = \left(\cos\theta_{\mathrm{pzc}} + 0.5\xi\,\mathrm{pH_{pzc}^2}\right) - \xi\mathrm{pH_{pzc}}\,\mathrm{pH} + 0.5\xi\,\mathrm{pH}^2 = [\cos(27°) + 2.147\times10^{-3}\times2.147\times10^{-3}\times4^2] - 6.877\times10^{-6}\times4\,\mathrm{pH} + 0.5\times2.147\times10^{-3}\mathrm{pH}^2 = 1.074\times10^{-3}\,\mathrm{pH}^2 - 8.589\times10^{-3}\,\mathrm{pH} + 0.91. \quad \text{(B-7)}$$

The calculated contact angle by Eq. (B-7) are shown in Fig. B-1, and a very poor agreement can be found between the calculated contact angle and the experimentally measured contact angle in our experiments. If we repeat the same process by calculating the parameters above based on 10^{-4} mol/kg HCl(aq) and NaOH(aq), the consistency is still non-ideal. Considering that we didn't utilize background electrolyte solution, if we took a as 0 in Eq. (B-2), unfortunately, the agreement is still poor (not shown in Fig. B-1). This kind of inconsistency occurs from 25 ℃ to 200 ℃.

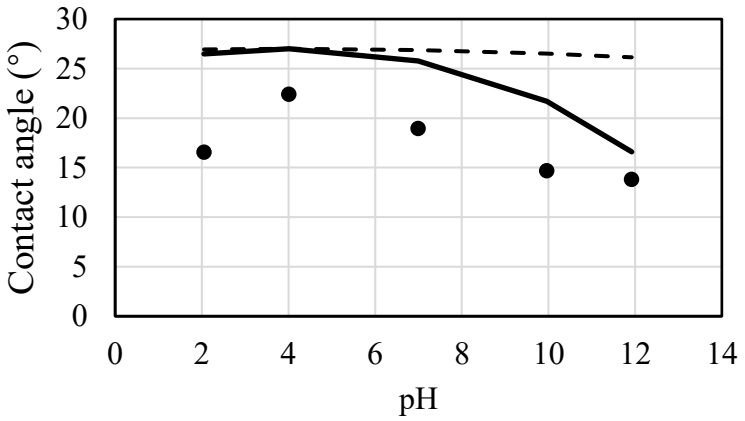

Fig. B-1. The pH dependence of the calculated contact angle based on 0.01 mol/kg (solid line) and 0.0001 mol/kg (dash line) electrolyte solution via Amadu et al. (2019) method, against our experimental results (dots) at 25 ℃.

Appendix C Calculation of pH_{iep} based on method by Bérubé et al. (1968)

According to Rotriguez et al. (2006), the equation to correlate the species at the silica surface can be written as:

$$-9.8 = -\log(H_4SiO_4) + \log(H^+) + \log(H_3SiO_4^-), \quad \text{(C-1)}$$

where $\log(H_4SiO_4) = 0.151 - 1162/T$, and it is independent of pH. Thus, at 298.15 K, the following species calculation can be written:

$$\log(H_3SiO_4^-)_{pzc} = -9.8 + \log(H_4SiO_4)_{293.15\,K} - \log(H^+)_{293.15\,K} = -9.8 + 0.151 - \frac{1162}{298.15} + 4.14 = -9.41. \quad \text{(C-2)}$$

Then, we can calculate the isoelectric point of silica at 318.15 K:

$$-\log(H^+)_{318.15\,K} = pH_{iep,318.15\,K} = -9.8 + \log(H_4SiO_4)_{318.15\,K} - \log(H_3SiO_4^-)_{iep} = -9.8 + 0.151 - \frac{1162}{318.15} + 9.41 = 3.84. \quad \text{(C-3)}$$

To verify the species calculation, we conducted similar calculations, based on the experimentally-obtained silica pH_{iep} at 293.15 K, 2.20, in accordance with Rotriguez et al. (2006). The calculated pH_{iep} at 308.15 K is 2.01, which is the same as the experimental results from the same work.

Back to our work, with the obtained pH_{iep} at 298.15 K and 323.15 K, the following equations can be written:

$$4.6R\left[0.5\ pK_{w,298.15\,K} - pH_{iep,298.15\,K}\right] = 4.6 \times 8.314 \times [0.5 \times\ 13.97 - 4.14] = \frac{\Delta H^*}{298.15} - \Delta S^*, \quad \text{(C-4)}$$

$$4.6R\left[0.5\ \mathrm{p}K_{\mathrm{w,323.15\ K}} - \mathrm{pH_{iep,323.15\ K}}\right] = 4.6 \times 8.314 \times [0.5 \times\ 13.24 - 3.84] = \frac{\Delta H^*}{323.15} - \Delta S^*. \quad \text{(C-5)}$$

Solve Eq. (C-4) and (C-5), and we have: ΔH^*=9580.3 J/mol; ΔS^*=-76.7 J/mol. Therefore, we can calculate $\mathrm{pH_{iep}}$ at other temperatures. Taking 373.15 K as an example:

$$4.6R\left[0.5\ \mathrm{p}K_{\mathrm{w,373.15\ K}} - \mathrm{pH_{iep,373.15\ K}}\right] = 4.6 \times 8.314 \times \left[0.5 \times\ 12.23 - \mathrm{pH_{iep,373.15\ K}}\right] = \frac{9580.3}{373.15} + 76.7,$$

$$\mathrm{pH_{iep,373.15\ K}} = 3.44. \quad \text{(C-6)}$$

Appendix D Table of the Available pH_{iep} of silica from other literature

Author	Solid material	Aqueous solution	Technique	pH	Type
Yukselen-Aksoy et al. (2010)	Quartz powder from Ottawa sand	HCl(aq) and NaOH(aq)	Zeta Meter 3.0+ from Zeta Meter Inc., VA)	<2 if any	iep
Júnior et al. (2014)	Quartz powder form Brazil with *d*50 = 13 µm mesh size	0.1 M KCl(aq) and NaOH(aq)	ELS Analysis Zeta Meter®	2.5	iep
Rodriguez et al. (2006)	Commercial quartz sample	0.1 M HCl(aq) and NaOH(aq)	Zeta Meter 3.0	2.3	iep
Liu et al. (2017)	Commercial quartz sample from Wuxi, China	HCl(aq) and NaOH(aq)	Colloidal Dynamics Zetaprobe (Colloidal Dynamics, USA)	2.11	iep
Zhou et al. (2015)	Quartz from China	0.1 M HCl (aq) and NaOH (aq) 100 mg/L and 1000 mg/L humic acid (HA)	Zetasizer (Malvern ZEN3600)	2.8	iep
Abaka-Wood et al. (2017)	Quartz from Australia	1 M HNO_3(aq) and KOH(aq)	Colloidal Dynamics AcoustoSizer II (Colloidal Dynamics Inc., USA)	2.2	iep
Vidyadhar et al. (2012)	Quartz from India (>99% purity)	0.2 M HCl(aq) and NaOH (aq) 10^{-3} M KNO_3 (aq)	Zeta Probe (Colloidal Dynamics, USA)	2	iep
Cuddy et al. (2013)	SiO_2 layer on QSX 303	HCl(aq) and NaOH(aq)	Contact angle	3.9±0.5	iep
Noh et al. (1988)	Cabot L90 SiO_2	$HClO_4$(aq) and NaOH(aq)	Titration	3.2	pzc
Sabia et al. (2000)	Fused SiO_2	10^{-5} M NaCl(aq) and HCl(aq)	Titration	3.5±0.1	pzc
Simonsson et al. (2018)	Silica sol	0.05-0.2 M NaCl(aq) and $NaNO_3$ (aq)	Malvern ZetaSizer Nano	4	iep
Liang et al. (2017)	Quartz (95% purity) from Geodiscoveries	10^{-4} M NaCl(aq)	ZetaPlus	<4 if any	iep

Kutzner et al. (2018)	Silica gel 60 from Merck	0.00037-3.7 M NaCl(aq)	NA	5.7-6.4	pzc
Kutzner et al. (2018)	Nucleodur 100–50, 50 µm, spherical	0.00037-3.7 M NaCl(aq)	NA	2.3-3.3	pzc
Kutzner et al. (2018)	Nucleodur 300–5, 5 µm, spherical	0.00037-3.7 M NaCl(aq)	NA	2.3-4.3	pzc
Schwarz et al. (2000)	Silica spheres up to size of 2µ	NA	Malvern Zetamaster	3.2	iep
Schwarz et al. (2000)	Sikron from Quartzwerke	NA	Malvern Zetamaster	4.5	iep
Salopek et al. (2017)	Quartz from Sigma Aldrich	HCl(aq)+NaOH(aq) 0.011 M NaCl(aq)	ZetaPlus instrument from Brookhaven	around 4	iep
Farooq et al. (2011)	Quartz aerosol from Evonik	0.5 M HCl(aq)+NaOH(aq) NaCl(aq), $CaCl_2$ $2H_2O$(aq), $MgCl_2$ $6H_2O$(aq)	Malvern Zetasizer Nano ZS	3.3±0.1	iep
Martinovic et al. (2004)	Quartz from Delmas mines	0.01 M HNO3(aq) and KOH(aq)	Malvern Zetasizer 4	<3 if any	iep
Marion et al. (2015)	Quartz from Daubois	10^{-3} M KCl(aq)	Electroacoustic zeta potential measurements	<3 if any	iep
Yang et al. (2018)	Quartz from China (>92% purity)	HCl(aq) and NaOH(aq)	Js94H zeta potential analyzer	2.3	iep
Guhra et al. (2019)	Quartz from Quarzwerke, washed with HCl(aq)	0.01 M NaCl(aq)	Nano ZS, Malvern Instruments	<2 if any	iep
Brown et al. (2016)	Ludox silica	0.01 to 0.1 M NaCl (aq)	NA	<3 if any	iep
Sonn et al. (2018)	12 nm silica from sigma-Aldrich	1 M HNO_3(aq)	ELS-8000 electrophoretic light scattering spectrometer	<1 if any	iep
Szewczuk-Karpisz et al. (2019)	Silica from sigma-Aldrich	0.1 M HCl(aq) and NaOH(aq) 0.01 M NaCl(aq)	Zetasizer 3000, Malvern	3	iep
Lützenkirchen et al. (2013)	Octadecyl-trichlorosilane covered fused silica	1, 10 , and 20 mM HCl(aq)	Streaming current and potential	3-4	iep

Lützenkirchen et al. (2013)	Octadecyl-trichlorosilane covered fused silica substrates	1, 10 , and 20 mM KCl(aq)	Streaming current and potential	3-4	iep
Gusev et al. (2002)	Fused-silica capillary	0.001 M NaCl(aq)	Streaming potential	4	iep
Givens et al. (2017)	SiO_2 from Cabot	1M HCl(aq) and 0.8 M NaOH(aq)	Beckman-Coulter Delsa Nano C	3.1	iep
Zienkiewicz-Strzałka et al. (2018)	Aerosil 300 from Evonik Degussa	0.1 M NaCl(aq)	potentiometric titration	3	iep

References

Aasly K, Malvik T, Myrhaug E (2007) Advanced methods to characterize thermal properties of quartz. Proc INFACON XI. New Dehli, India, February: 18-21

Abaka-Wood, G., Addai-Mensah, J., & Skinner, W. (2017). A study of flotation characteristics of monazite, hematite, and quartz using anionic collectors. *International Journal Of Mineral Processing*, *158*, 55-62. doi: 10.1016/j.minpro.2016.11.012

Abdel-Khalek, N., Selim, K., Yassin, K., & Abdallah, S. (2015). Bio-flotation of Egyptian Phosphate Using Desulfvibrio Desulfuricans Bacteria. *Journal Of Mining World Express*, *4*(0), 19. doi: 10.14355/mwe.2015.04.002

Agbalaka, C., Dandekar, A., Patil, S., Khataniar, S., & Hemsath, J. (2008). The Effect Of Wettability On Oil Recovery: A Review. *All Days*. doi: 10.2118/114496-ms

Al-Rossies AAS, Al-Anazi BD, Paiaman AM. Effect of pH-values on the contact angle and interfacial tension. NAFTA. 2010;61(4):181–6.

Al-Zaidi, E., & Fan, X. (2018). Effect of aqueous electrolyte concentration and valency on contact angle on flat glass surfaces and inside capillary glass tubes. *Colloids And Surfaces A: Physicochemical And Engineering Aspects*, *543*, 1-8. doi: 10.1016/j.colsurfa.2018.01.045

Amadu, M., & Pegg, M. (2019). Analytical derivation of a pH dependent contact angle equation and the relationship to industrial processes of energy concerns. *Journal Of Petroleum Science And Engineering*, *174*, 844-858. doi: 10.1016/j.petrol.2018.11.036

Amott, E. (1959). Observations Relating to the Wettability of Porous Rock. *Transactions Of The AIME*, *216*(01), 156-162. doi: 10.2118/1167-g

Armistead, C., Tyler, A., Hambleton, F., Mitchell, S., & Hockey, J. (1969). Surface hydroxylation of silica. *The Journal Of Physical Chemistry*, *73*(11), 3947-3953. doi: 10.1021/j100845a065

Arsalan, N., Buiting, J., & Nguyen, Q. (2015). Surface energy and wetting behavior of reservoir rocks. *Colloids And Surfaces A: Physicochemical And Engineering Aspects*, *467*, 107-112. doi: 10.1016/j.colsurfa.2014.11.024

Arsalan, N., Palayangoda, S., Burnett, D., Buiting, J., & Nguyen, Q. (2013). Surface energy characterization of sandstone rocks. *Journal Of Physics And Chemistry Of Solids*, *74*(8), 1069-1077. doi: 10.1016/j.jpcs.2013.02.027

Barajas, A., & Panton, R. (1993). The effects of contact angle on two-phase flow in capillary tubes. *International Journal Of Multiphase Flow*, *19*(2), 337-346. doi: 10.1016/0301-9322(93)90007-h

Barranco, F., Dawson, H., Christener, J., & Honeyman, B. (1997). Influence of Aqueous pH and Ionic Strength on the Wettability of Quartz in the Presence of Dense Non-Aqueous-Phase Liquids. *Environmental Science & Technology*, *31*(3), 676-681. doi: 10.1021/es960217m

Beattie, J., Djerdjev, A., Gray-Weale, A., Kallay, N., Lützenkirchen, J., Preočanin, T., & Selmani, A. (2014). pH and the surface tension of water. *Journal Of Colloid And Interface Science*, *422*, 54-57. doi: 10.1016/j.jcis.2014.02.003

Belhaj, A., Elraies, K., Mahmood, S., Zulkifli, N., Akbari, S., & Hussien, O. (2019). The effect of surfactant concentration, salinity, temperature, and pH on surfactant adsorption for chemical enhanced oil recovery: a review. *Journal Of Petroleum Exploration And Production Technology*, *10*(1), 125-137. doi: 10.1007/s13202-019-0685-y

Bérubé, Y., & de Bruyn, P. (1968). Adsorption at the rutile-solution interface. *Journal Of Colloid And Interface Science*, *27*(2), 305-318. doi: 10.1016/0021-9797(68)90038-6

Bigelow, W., Pickett, D., & Zisman, W. (1946). Oleophobic monolayers. *Journal Of Colloid Science*, *1*(6), 513-538. doi: 10.1016/0095-8522(46)90059-1

Blake, T., & Batts, G. (2019). The temperature-dependence of the dynamic contact angle. *Journal Of Colloid And Interface Science*, *553*, 108-116. doi: 10.1016/j.jcis.2019.06.006

Bonn, D., Eggers, J., Indekeu, J., Meunier, J., & Rolley, E. (2009). Wetting and spreading. *Reviews Of Modern Physics*, *81*(2), 739-805. doi: 10.1103/revmodphys.81.739

Brady, P., & Thyne, G. (2016). Functional Wettability in Carbonate Reservoirs. *Energy & Fuels*, *30*(11), 9217-9225. doi: 10.1021/acs.energyfuels.6b01895

Brady, P., Krumhansl, J., & Mariner, P. (2012). Surface Complexation Modeling for Improved Oil Recovery. *All Days*. doi: 10.2118/153744-ms

Briggs, D., Rance, D., & Briscoe, B. (1989). Surface Properties. *Comprehensive Polymer Science And Supplements*, 707-732. doi: 10.1016/b978-0-08-096701-1.00060-4

Brown, M., Goel, A., & Abbas, Z. (2016). Effect of Electrolyte Concentration on the Stern Layer Thickness at a Charged Interface. *Angewandte Chemie International Edition*, *55*(11), 3790-3794. doi: 10.1002/anie.201512025

Butt, H., Graf, K., & Kappl, M. (2003). *Physics and chemistry of interfaces* (1st ed.). Weinheim: Wiley-VCH.

Butt, H., Graf, K., & Kappl, M. (2006). *Physics and Chemistry of Interfaces* (2nd ed.). Weinheim: Wiley-VCH.

Carmeliet, J., Chen, L., Kang, Q., & Derome, D. (2017). Beyond-Cassie Mode of Wetting and Local Contact Angles of Droplets on Checkboard-Patterned Surfaces. *Langmuir*, *33*(24), 6192-6200. doi: 10.1021/acs.langmuir.7b01471

Carré, A., Lacarrière, V., & Birch, W. (2003). Molecular interactions between DNA and an aminated glass substrate. *Journal Of Colloid And Interface Science*, *260*(1), 49-55. doi: 10.1016/s0021-9797(02)00147-9

Cassie, A., & Baxter, S. (1944). Wettability of porous surfaces. *Transactions Of The Faraday Society*, *40*, 546. doi: 10.1039/tf9444000546

Chau, T. (2009). A review of techniques for measurement of contact angles and their applicability on mineral surfaces. *Minerals Engineering*, *22*(3), 213-219. doi: 10.1016/j.mineng.2008.07.009

Cuddy, M., Poda, A., & Brantley, L. (2013). Determination of Isoelectric Points and the Role of pH for Common Quartz Crystal Microbalance Sensors. *ACS Applied Materials & Interfaces*, *5*(9), 3514-3518. doi: 10.1021/am400909g

Deng, W., Zhang, X., Jia, R., Huang, L., Zhang, X., & Jie, J. (2019). Organic molecular crystal-based photosynaptic devices for an artificial visual-perception system. *NPG Asia Materials*, *11*(1). doi: 10.1038/s41427-019-0182-2

Donaldson, A., Everitt, B., Newton, T., Steele, J., Sherriff, M., & Bower, E. (2008). The Effects of Social Class and Dental Attendance on Oral Health. *Journal Of Dental Research*, *87*(1), 60-64. doi: 10.1177/154405910808700110

Donaldson, E., & Alam, W. (2008). Surface Forces. *Wettability*, 57-119. doi: 10.1016/b978-1-933762-29-6.50008-9

Donaldson, E., Thomas, R., & Lorenz, P. (1969). Wettability Determination and Its Effect on Recovery Efficiency. *Society Of Petroleum Engineers Journal*, *9*(01), 13-20. doi: 10.2118/2338-pa

Ducker, W., Xu, Z., & Israelachvili, J. (1994). Measurements of Hydrophobic and DLVO Forces in Bubble-Surface Interactions in Aqueous Solutions. *Langmuir*, *10*(9), 3279-3289. doi: 10.1021/la00021a061

Duffy, T., Gamwo, I., Johns, R., & Lvov, S. (2021). Modeling Contact Angle vs. Temperature for the Quartz-Water-Decane System. *SPE Journal*, 1-13. doi: 10.2118/205518-pa

Dwivedi, C., Pandey, I., Pandey, H., Ramteke, P., Pandey, A., Mishra, S., & Patil, S. (2017). Electrospun Nanofibrous Scaffold as a Potential Carrier of Antimicrobial Therapeutics for Diabetic Wound Healing and Tissue Regeneration. *Nano- And Microscale Drug Delivery Systems*, 147-164. doi: 10.1016/b978-0-323-52727-9.00009-1

Ebnesajjad, S., & Landrock, A. (2015). Surface Tension and Its Measurement. *Adhesives Technology Handbook*, 19-34. doi: 10.1016/b978-0-323-35595-7.00002-4

Enhanced Oil Recovery. (2021). Retrieved from https://www.energy.gov/fe/science-innovation/oil-gas-research/enhanced-oil-recovery

Eral, H., 't Mannetje, D., & Oh, J. (2012). Contact angle hysteresis: a review of fundamentals and applications. *Colloid And Polymer Science*, *291*(2), 247-260. doi: 10.1007/s00396-012-2796-6

Erdlac, Jr., R.J., Trentham, R.C., Armour, L., Lee, R., and Miller, B., 2006, "Adding to the geothermal energy portfolio from deep sedimentary basins", in Pritchett, J., Technical Program Chairman, Geothermal Resources – Securing Our Energy Future: Geothermal Resources Council Transactions, 30, p. 875-883.

Falode, O., & Manuel, E. (2014). Wettability Effects on Capillary Pressure, Relative Permeability, and Irredcucible Saturation Using Porous Plate. *Journal Of Petroleum Engineering*, *2014*, 1-12. doi: 10.1155/2014/465418

Farooq, U., Tweheyo, M., Sjöblom, J., & Øye, G. (2011). Surface Characterization of Model, Outcrop, and Reservoir Samples in Low Salinity Aqueous Solutions. *Journal Of Dispersion Science And Technology*, *32*(4), 519-531. doi: 10.1080/01932691003756936

Faucher, M., Gravel, O., & Larachi, F. (2020). A continuous-flow surface flotation cell for the separation of scanty mineral samples based on wettability contrast. *The Canadian Journal Of Chemical Engineering*. doi: 10.1002/cjce.23844

Frequently Asked Questions (FAQs) - U.S. Energy Information Administration (EIA). (2021). Retrieved from https://www.eia.gov/tools/faqs/faq.php?id=709&t=6

Gaikwad, V., Choudhari, P., Bhatia, N., & Bhatia, M. (2019). Characterization of pharmaceutical nanocarriers: in vitro and in vivo studies. *Nanomaterials For Drug Delivery And Therapy*, 33-58. doi: 10.1016/b978-0-12-816505-8.00016-3

Gao, L., & McCarthy, T. (2006). Contact Angle Hysteresis Explained. *Langmuir*, *22*(14), 6234-6237. doi: 10.1021/la060254j

Gao, L., & McCarthy, T. (2007). How Wenzel and Cassie Were Wrong. *Langmuir*, *23*(7), 3762-3765. doi: 10.1021/la062634a

Gao, W., & Li, Z. (2010). Nanostructured transition metal oxides and their applications in composites. *Physical Properties And Applications Of Polymer Nanocomposites*, 723-742. doi: 10.1533/9780857090249.4.723

Gavish, N., & Promislow, K. (2016). Dependence of the dielectric constant of electrolyte solutions on ionic concentration: A microfield approach. *Physical Review E*, *94*(1). doi: 10.1103/physreve.94.012611

Givens, B., Diklich, N., Fiegel, J., & Grassian, V. (2017). Adsorption of bovine serum albumin on silicon dioxide nanoparticles: Impact of pH on nanoparticle–protein interactions. *Biointerphases*, *12*(2), 02D404. doi: 10.1116/1.4982598

Godin, B., Touitou, E., Krishnan, R., Heller, M., Green, N., & Nili, H. et al. (2012). Disjoining Pressure and Capillary Adhesion. *Encyclopedia Of Nanotechnology*, 572-577. doi: 10.1007/978-90-481-9751-4_212

Gong, B., Liang, H., Xin., S., and Li, K., 2011: "EFFECT OF WATER INJECTION ON RESERVOIR TEMPERATURE DURING POWER GENERATION IN OIL FIELDS", Thirty-Six Workshop on Geothermal Reservoir Engineering, Stanford, CA.

Gong, H., Li, Y., Dong, M., Ma, S., & Liu, W. (2016). Effect of wettability alteration on enhanced heavy oil recovery by alkaline flooding. *Colloids And Surfaces A: Physicochemical And Engineering Aspects*, *488*, 28-35. doi: 10.1016/j.colsurfa.2015.09.042

Graue, A., Viksund, B., Eilertsen, T., & Moe, R. (1999). Systematic wettability alteration by aging sandstone and carbonate rock in crude oil. *Journal Of Petroleum Science And Engineering*, *24*(2-4), 85-97. doi: 10.1016/s0920-4105(99)00033-9

Guancheng, J. (2018). *Gas wettability of reservoir rock surfaces with porous media* (1st ed.).

Guhra, T., Ritschel, T., & Totsche, K. (2019). Formation of mineral-mineral and organo-mineral composite building units from microaggregate-forming materials including microbially produced extracellular polymeric substances. *European Journal Of Soil Science*, *70*(3), 604-615. doi: 10.1111/ejss.12774

Gusev, I., & Horváth, C. (2002). Streaming potential in open and packed fused-silica capillaries. *Journal Of Chromatography A*, *948*(1-2), 203-223. doi: 10.1016/s0021-9673(01)01450-9

Haagh, M., Schilderink, N., Duits, M., Siretanu, I., Mugele, F., & Collins, I. (2018). Salinity-dependent contact angle alteration in oil/brine/silicate systems: The effect of temperature. *Journal Of Petroleum Science And Engineering*, *165*, 1040-1048. doi: 10.1016/j.petrol.2017.11.068

Hamouda, A., & Rezaei Gomari, K. (2006). Influence of Temperature on Wettability Alteration of Carbonate Reservoirs. *All Days*. doi: 10.2118/99848-ms

Hansen, G., Hamouda, A., & Denoyel, R. (2000). The effect of pressure on contact angles and wettability in the mica/water/n-decane system and the calcite+stearic acid/water/n-decane system. *Colloids And Surfaces A: Physicochemical And Engineering Aspects*, *172*(1-3), 7-16. doi: 10.1016/s0927-7757(99)00498-7

Hebbar, R., Isloor, A., & Ismail, A. (2017). Contact Angle Measurements. *Membrane Characterization*, 219-255. doi: 10.1016/b978-0-444-63776-5.00012-7

Henseler, J., Ringle, C., & Sinkovics, R. (2009). The use of partial least squares path modeling in international marketing. *Advances In International Marketing*, 277-319. doi: 10.1108/s1474-7979(2009)0000020014

Hilpert, M. (2009). Effects of dynamic contact angle on liquid infiltration into horizontal capillary tubes: (Semi)-analytical solutions. *Journal Of Colloid And Interface Science*, *337*(1), 131-137. doi: 10.1016/j.jcis.2009.04.013

Hirasaki, G. (1991). Wettability: Fundamentals and Surface Forces. *SPE Formation Evaluation*, *6*(02), 217-226. doi: 10.2118/17367-pa

Hjelmeland, O., & Larrondo, L. (1986). Experimental Investigation of the Effects of Temperature, Pressure, and Crude Oil Composition on Interfacial Properties. *SPE Reservoir Engineering*, *1*(04), 321-328. doi: 10.2118/12124-pa

Hunter, R. (2001). *Foundations of colloid science*. Oxford: Oxford University Press.

Hurwitz, G., Guillen, G., & Hoek, E. (2010). Probing polyamide membrane surface charge, zeta potential, wettability, and hydrophilicity with contact angle measurements. *Journal Of Membrane Science*, *349*(1-2), 349-357. doi: 10.1016/j.memsci.2009.11.063

Iler, R. (1978). Hydrogen-Bonded Complexes of Silica with Organic Compounds. *Biochemistry Of Silicon And Related Problems*, 53-76. doi: 10.1007/978-1-4613-4018-8_2

Israelachvili, J. (2011). *Intermolecular and surface forces* (3rd ed.). Amsterdam: Elsevier Academic.

Jadhunandan, P P, & Morrow, N R. Spontaneous imbibition of water by crude oil/brine/rock systems. United States.

Jadhunandan, P., & Morrow, N. (1995). Effect of Wettability on Waterflood Recovery for Crude-Oil/Brine/Rock Systems. *SPE Reservoir Engineering*, *10*(01), 40-46. doi: 10.2118/22597-pa

Jennings, H. (1967). The effect of temperature and pressure on the interfacial tension of benzene-water and normal decane-water. *Journal Of Colloid And Interface Science*, *24*(3), 323-329. doi: 10.1016/0021-9797(67)90257-3

Jeon, D. (2019). Wettability in electrodes and its impact on the performance of lithium-ion batteries. *Energy Storage Materials*, *18*, 139-147. doi: 10.1016/j.ensm.2019.01.002

Johnson, D., Miles, N., & Hilal, N. (2006). Quantification of particle–bubble interactions using atomic force microscopy: A review. *Advances In Colloid And Interface Science*, *127*(2), 67-81. doi: 10.1016/j.cis.2006.11.005

Kakati, A., & Sangwai, J. (2018). Wettability Alteration of Mineral Surface during Low-Salinity Water Flooding: Role of Salt Type, Pure Alkanes, and Model Oils Containing Polar Components. *Energy & Fuels*, *32*(3), 3127-3137. doi: 10.1021/acs.energyfuels.7b03727

Kaliakin, V. (2017). Example Problems Involving In Situ Stresses Under Hydrostatic Conditions. *Soil Mechanics*, 205-242. doi: 10.1016/b978-0-12-804491-9.00005-7

Kamal, M., Adewunmi, A., Sultan, A., Al-Hamad, M., & Mehmood, U. (2017). Recent Advances in Nanoparticles Enhanced Oil Recovery: Rheology, Interfacial Tension, Oil Recovery, and Wettability Alteration. *Journal Of Nanomaterials*, *2017*, 1-15. doi: 10.1155/2017/2473175

Kayama, M., Nagaoka, H., & Niihara, T. (2018). Lunar and Martian Silica. *Minerals*, *8*(7), 267. doi: 10.3390/min8070267

Kondiparty, K., Nikolov, A., Wu, S., & Wasan, D. (2011). Wetting and Spreading of Nanofluids on Solid Surfaces Driven by the Structural Disjoining Pressure: Statics Analysis and Experiments. *Langmuir*, *27*(7), 3324-3335. doi: 10.1021/la104204b

Korrani, A., & Jerauld, G. (2019). Modeling wettability change in sandstones and carbonates using a surface-complexation-based method. *Journal Of Petroleum Science And Engineering*, *174*, 1093-1112. doi: 10.1016/j.petrol.2018.12.016

Kosmulski, M. (2016). Isoelectric points and points of zero charge of metal (hydr)oxides: 50years after Parks' review. *Advances In Colloid And Interface Science*, *238*, 1-61. doi: 10.1016/j.cis.2016.10.005

Krainer, S., Saes, L., & Hirn, U. (2020). Predicting inkjet dot spreading and print through from liquid penetration- and picoliter contact angle measurement. *Nordic Pulp & Paper Research Journal*, *35*(1), 124-136. doi: 10.1515/npprj-2019-0088

Kulinič, V. (2015). The influence of wettability on oil recovery. *AGH Drilling, Oil, Gas*, *32*(3), 493. doi: 10.7494/drill.2015.32.3.493

Kumar, A., & Dixit, C. (2017). Methods for characterization of nanoparticles. *Advances In Nanomedicine For The Delivery Of Therapeutic Nucleic Acids*, 43-58. doi: 10.1016/b978-0-08-100557-6.00003-1

Kutzner, S., Schaffer, M., Licha, T., Worch, E., & Börnick, H. (2018). Sorption of cationic organic substances onto synthetic oxides: Evaluation of sorbent parameters as possible predictors. *Science Of The Total Environment*, *643*, 632-639. doi: 10.1016/j.scitotenv.2018.05.393

Lager, A., Webb, K., Collins, I., & Richmond, D. (2008). LoSal Enhanced Oil Recovery: Evidence of Enhanced Oil Recovery at the Reservoir Scale. *All Days*. doi: 10.2118/113976-ms

Lewis, R., Makurat, A., & Pao, W. (2003). Fully coupled modeling of seabed subsidence and reservoir compaction of North Sea oil fields. *Hydrogeology Journal*, *11*(1), 142-161. doi: 10.1007/s10040-002-0239-z

Li, L., Xu, Z., Sun, W., Chen, J., Dai, C., Yan, B., & Zeng, H. (2020). Bio-inspired membrane with adaptable wettability for smart oil/water separation. *Journal Of Membrane Science*, *598*, 117661. doi: 10.1016/j.memsci.2019.117661

Li, X., Fan, X., & Brandani, S. (2014). Difference in pore contact angle and the contact angle measured on a flat surface and in an open space. *Chemical Engineering Science*, *117*, 137-145. doi: 10.1016/j.ces.2014.06.024

Li, Y., Pham, J., Johnston, K., & Green, P. (2007). Contact Angle of Water on Polystyrene Thin Films: Effects of CO2 Environment and Film Thickness. *Langmuir*, *23*(19), 9785-9793. doi: 10.1021/la0636311

Liang, L., Wang, L., Nguyen, A., & Xie, G. (2017). Heterocoagulation of alumina and quartz studied by zeta potential distribution and particle size distribution measurements. *Powder Technology*, *309*, 1-12. doi: 10.1016/j.powtec.2016.12.054

Licari, J., & Dale W. Swanson. (2011). *Adhesives Technology for Electronic Applications*. Elsevier Science.

Liu, C., Min, F., Liu, L., Chen, J., & Du, J. (2017). Mechanism of hydrolyzable metal ions effect on the zeta potential of fine quartz particles. *Journal Of Dispersion Science And Technology*, *39*(2), 298-304. doi: 10.1080/01932691.2017.1316205

Liu, Z., Yu, X., & Wan, L. (2014). Capillary rise method for the measurement of the contact angle of soils. *Acta Geotechnica*, *11*(1), 21-35. doi: 10.1007/s11440-014-0352-x

Lou, X. (2019). *EXPERIMENTAL STUDY OF GAS-LIQUID DIFFUSION IN POROUS ROCKS AND BULK FLUIDS* (Master of Science). The Pennsylvania State University.

Lützenkirchen, J., & Richter, C. (2012). Zeta-potential measurements of OTS-covered silica samples. *Adsorption*, *19*(2-4), 217-224. doi: 10.1007/s10450-012-9443-x

Lvov, S. (2014). *Introduction to electrochemical science and engineering* (1st ed.). CRC Press.

Lvov, S. (2021). *Introduction to electrochemical science and engineering* (2nd ed.). CRC Press. Manuscript submitted for publication.

Lvov, S., Hall, D., Bandura, A., & Gamwo, I. (2018). A semi-empirical molecular statistical thermodynamic model for calculating standard molar Gibbs energies of aqueous species above and below the critical point of water. *Journal Of Molecular Liquids*, *270*, 62-73. doi: 10.1016/j.molliq.2018.01.074

Mahani, H., Keya, A., Berg, S., & Nasralla, R. (2016). Electrokinetics of Carbonate/Brine Interface in Low-Salinity Waterflooding: Effect of Brine Salinity, Composition, Rock Type, and pH on ?-Potential and a Surface-Complexation Model. *SPE Journal*, *22*(01), 53-68. doi: 10.2118/181745-pa

Marion, C., Jordens, A., McCarthy, S., Grammatikopoulos, T., & Waters, K. (2015). An investigation into the flotation of muscovite with an amine collector and calcium lignin sulfonate depressant. *Separation And Purification Technology*, *149*, 216-227. doi: 10.1016/j.seppur.2015.04.025

Marmier, N., Delisée, A., & Fromage, F. (1999). Surface Complexation Modeling of Yb(III), Ni(II), and Cs(I) Sorption on Magnetite. *Journal Of Colloid And Interface Science*, *211*(1), 54-60. doi: 10.1006/jcis.1998.5968

Martinez, N. (2009). *WETTABILITY OF SILICON, SILICON DIOXIDE, AND ORGANOSILICATE GLASS* (MASTER OF SCIENCE). UNIVERSITY OF NORTH TEXAS.

MARTINOVIC, J., 2004. Investigation of the Surface Properties of Gangue Minerals in PGM Bearing Ores. University of Cape Town.

Masoud, M., 2015. Comparing Carbon Dioxide Injection in Enhanced Oil Recovery With other Methods. Austin Chem Eng. 2015; 2(2):1019.

Mathur, A., Sharma, P., & Cammarata, R. (2005). Negative surface energy — clearing up confusion. *Nature Materials*, *4*(3), 186-186. doi: 10.1038/nmat1336a

McCafferty, E. (1999). A Surface Charge Model of Corrosion Pit Initiation and of Protection by Surface Alloying. *Journal Of The Electrochemical Society*, *146*(8), 2863-2869. doi: 10.1149/1.1392021

McHale, G. (2007). Cassie and Wenzel: Were They Really So Wrong?. *Langmuir*, *23*(15), 8200-8205. doi: 10.1021/la7011167

Miller, J. (2020). In simple words, what is the difference between Isoelectric Point (IEP) and Point of Zero Charge (PZC)?. Retrieved from https://www.researchgate.net/post/In-simple-words-what-is-the-difference-between-Isoelectric-Point-IEP-and-Point-of-Zero-Charge-PZC

Morel, B., Autissier, L., Autissier, D., Lemordant, D., Yrieix, B., & Quenard, D. (2009). Pyrogenic silica ageing under humid atmosphere. *Powder Technology*, *190*(1-2), 225-229. doi: 10.1016/j.powtec.2008.04.049

Morrow, N. (1975). The Effects of Surface Roughness On Contact: Angle With Special Reference to Petroleum Recovery. *Journal Of Canadian Petroleum Technology*, *14*(04). doi: 10.2118/75-04-04

Morrow, N. (1990). Wettability and Its Effect on Oil Recovery. *Journal Of Petroleum Technology*, *42*(12), 1476-1484. doi: 10.2118/21621-pa

Morrow, N. (1990). Wettability and Its Effect on Oil Recovery. *Journal Of Petroleum Technology*, *42*(12), 1476-1484. doi: 10.2118/21621-pa

Mulqueen, M., & Huibers, P. (2020). Measuring Equilibrium Surface Tensions,surface tension measurement, surface tension meter,interface tensiometer, surface tensiometer, how to measuring surface tension-KINO Scientific Instrument Inc. Retrieved from http://www.surface-tension.org/articleshow_56.html

Muster, T., Prestidge, C., & Hayes, R. (2001). Water adsorption kinetics and contact angles of silica particles. *Colloids And Surfaces A: Physicochemical And Engineering Aspects*, *176*(2-3), 253-266. doi: 10.1016/s0927-7757(00)00600-2

Nasralla, R., Bataweel, M., & Nasr-El-Din, H. (2013). Investigation of Wettability Alteration and Oil-Recovery Improvement by Low-Salinity Water in Sandstone Rock. *Journal Of Canadian Petroleum Technology*, *52*(02), 144-154. doi: 10.2118/146322-pa

Neumann, A. (1974). Contact angles and their temperature dependence: thermodynamic status, measurement, interpretation and application. *Advances In Colloid And Interface Science*, *4*(2-3), 105-191. doi: 10.1016/0001-8686(74)85001-3

Nguyen, A., Nalaskowski, J., & Miller, J. (2003). The dynamic nature of contact angles as measured by atomic force microscopy. *Journal Of Colloid And Interface Science*, *262*(1), 303-306. doi: 10.1016/s0021-9797(03)00123-1

Noh, J., & Schwarz, J. (1989). Estimation of the point of zero charge of simple oxides by mass titration. *Journal Of Colloid And Interface Science*, *130*(1), 157-164. doi: 10.1016/0021-9797(89)90086-6

Oss, C. (2006). *Interfacial forces in aqueous media*. Boca Raton: Taylor and Francis.

Pal, S., Mushtaq, M., Banat, F., & Al Sumaiti, A. (2017). Review of surfactant-assisted chemical enhanced oil recovery for carbonate reservoirs: challenges and future perspectives. *Petroleum Science*, *15*(1), 77-102. doi: 10.1007/s12182-017-0198-6

Park, J., & Pas, M. (1995). Effects of Drying Methods and Wettability of Silicon on the Formation of Water Marks in Semiconductor Processing. *Journal Of The Electrochemical Society*, *142*(6), 2028-2031. doi: 10.1149/1.2044235

Pinnock, S. and Dutton, D., 2021. *The Golden Eagle, Peregrine and Solitaire fields, Blocks 14/26a and 20/01, UK North Sea*.

Plevachuk, Y., Hoyer, W., Kaban, I., Köhler, M., & Novakovic, R. (2009). Experimental study of density, surface tension, and contact angle of Sn–Sb-based alloys for high temperature soldering. *Journal Of Materials Science*, *45*(8), 2051-2056. doi: 10.1007/s10853-009-4120-5

Qin Jun, Zhang Zongbin, Cui Zhisong, Ba Zhongchen, Yu Qi. Effect of temperature on oil/water relative permeability of heavy oil reservoirs in Well J7, Changji oilfield[J]. China Petroleum Exploration, 2018, 23(6): 107-112.

Rallini, M., & Kenny, J. (2017). Nanofillers in Polymers. *Modification Of Polymer Properties*, 47-86. doi: 10.1016/b978-0-323-44353-1.00003-8

Ralston, J., Fornasiero, D., & Hayes, R. (1999). Bubble–particle attachment and detachment in flotation. *International Journal Of Mineral Processing*, *56*(1-4), 133-164. doi: 10.1016/s0301-7516(98)00046-5

Rao, D. (1999). Wettability Effects in Thermal Recovery Operations. *SPE Reservoir Evaluation & Engineering*, *2*(05), 420-430. doi: 10.2118/57897-pa

Rao, D., & Girard, M. (1996). A New Technique For Reservoir Wettability Characterization. *Journal Of Canadian Petroleum Technology*, *35*(01). doi: 10.2118/96-01-05

Rodríguez, K., & Araujo, M. (2006). Temperature and pressure effects on zeta potential values of reservoir minerals. *Journal Of Colloid And Interface Science*, *300*(2), 788-794. doi: 10.1016/j.jcis.2006.04.030

Ruan, Y., Zhang, Z., Luo, H., Xiao, C., Zhou, F., & Chi, R. (2018). Effects of Metal Ions on the Flotation of Apatite, Dolomite and Quartz. *Minerals*, *8*(4), 141. doi: 10.3390/min8040141

Salopek, J., Sadžak, A., Kuzman, D., Požar, J., & Kovačević, D. (2017). Polyelectrolyte Multilayers on Silica Surfaces: Effect of Ionic Strength and Sodium Salt Type. *Croatica Chemica Acta*, *90*(2). doi: 10.5562/cca3179

Sanaei, A., Tavassoli, S., & Sepehrnoori, K. (2019). Investigation of modified Water chemistry for improved oil recovery: Application of DLVO theory and surface complexation model. *Colloids And Surfaces A: Physicochemical And Engineering Aspects*, *574*, 131-145. doi: 10.1016/j.colsurfa.2019.04.075

Sandersen, S. B. (2012). Enhanced Oil Recovery with Surfactant Flooding. Technical University of Denmark.

Sarmadivaleh, M., Al-Yaseri, A., & Iglauer, S. (2015). Influence of temperature and pressure on quartz–water–CO2 contact angle and CO2–water interfacial tension. *Journal Of Colloid And Interface Science*, *441*, 59-64. doi: 10.1016/j.jcis.2014.11.010

Sato, E., Tamura, H., & Matsumoto, A. (2010). Cohesive Force Change Induced by Polyperoxide Degradation for Application to Dismantlable Adhesion. *ACS Applied Materials & Interfaces*, *2*(9), 2594-2601. doi: 10.1021/am1004392

Schoonen, M. (1994). Calculation of the point of zero charge of metal oxides between 0 and 350°C. *Geochimica Et Cosmochimica Acta*, *58*(13), 2845-2851. doi: 10.1016/0016-7037(94)90118-x

Schrader, A., Monroe, J., Sheil, R., Dobbs, H., Keller, T., & Li, Y. et al. (2018). Surface chemical heterogeneity modulates silica surface hydration. *Proceedings Of The National Academy Of Sciences*, *115*(12), 2890-2895. doi: 10.1073/pnas.1722263115

Schwarz, S., Lunkwitz, K., Keßler, B., Spiegler, U., Killmann, E., & Jaeger, W. (2000). Adsorption and stability of colloidal silica. *Colloids And Surfaces A: Physicochemical And Engineering Aspects*, *163*(1), 17-27. doi: 10.1016/s0927-7757(99)00426-4

Seo, K., Kim, M., & Kim, D. (2015). Re-derivation of Young's Equation, Wenzel Equation, and Cassie-Baxter Equation Based on Energy Minimization. *Surface Energy*. doi: 10.5772/61066

Sharma, B., Maerefat, N.L., and Crocker, M.E.: ''Geoscience Application to the Prediction of Reservoir Variations,'' US-DOE Contracts for Field Projects and Supporting Research on Enhanced Oil Recovery, Vol. 44, p. 85 ~September 1985

Sheng, J. (2013). Alkaline Flooding. *Enhanced Oil Recovery Field Case Studies*, 143-167. doi: 10.1016/b978-0-12-386545-8.00006-3

Siemons, N., Bruining, H., Castelijns, H., & Wolf, K. (2006). Pressure dependence of the contact angle in a CO2–H2O–coal system. *Journal Of Colloid And Interface Science*, *297*(2), 755-761. doi: 10.1016/j.jcis.2005.11.047

Simonsson, I., Sögaard, C., Rambaran, M., & Abbas, Z. (2018). The specific co-ion effect on gelling and surface charging of silica nanoparticles: Speculation or reality?. *Colloids And Surfaces A: Physicochemical And Engineering Aspects*, *559*, 334-341. doi: 10.1016/j.colsurfa.2018.09.057

Singh, K., Menke, H., Andrew, M., Lin, Q., Rau, C., Blunt, M., & Bijeljic, B. (2017). Dynamics of snap-off and pore-filling events during two-phase fluid flow in permeable media. *Scientific Reports*, *7*(1). doi: 10.1038/s41598-017-05204-4

Skauge, A., Sørvik, A., Vik, B., & Spildo, K. (2006). EFFECT OF WETTABILITY ON OIL RECOVERY FROM CARBONATE MATERIAL REPRESENTING DIFFERENT PORE CLASSES.

Song, J., Zeng, D., & Fan, L. (2020). Temperature dependence of contact angles of water on a stainless steel surface at elevated temperatures and pressures: In situ characterization and thermodynamic analysis. *Journal Of Colloid And Interface Science*, *561*, 870-880. doi: 10.1016/j.jcis.2019.11.070Li, X., Fan, X., & Brandani, S. (2014). Difference in pore contact angle and the contact angle measured on a flat surface and in an open space. *Chemical Engineering Science*, *117*, 137-145. doi: 10.1016/j.ces.2014.06.024

Sonia, T., & Sharma, C. (2014). Experimental techniques involved in the development of oral insulin carriers. *Oral Delivery Of Insulin*, 169-217. doi: 10.1533/9781908818683.169

Sonn, J., Lee, J., Jo, S., Yoon, I., Jung, C., & Lim, J. (2018). Effect of surface modification of silica nanoparticles by silane coupling agent on decontamination foam stability. *Annals Of Nuclear Energy*, *114*, 11-18. doi: 10.1016/j.anucene.2017.12.007

Spitze, L., & Richards, D. (1947). Surface Studies of Glass. Part I. Contact Angles. *Journal Of Applied Physics*, *18*(10), 904-911. doi: 10.1063/1.1697565

Stavi, I., Barkai, D., Knoll, Y., & Zaady, E. (2016). Livestock grazing impact on soil wettability and erosion risk in post-fire agricultural lands. *Science Of The Total Environment*, *573*, 1203-1208. doi: 10.1016/j.scitotenv.2016.03.126

Szewczuk-Karpisz, K., & Wiśniewska, M. (2019). Adsorption layer structure at soil mineral/biopolymer/supporting electrolyte interface – The impact on solid aggregation. *Journal Of Molecular Liquids*, *284*, 117-123. doi: 10.1016/j.molliq.2019.03.172

Teletzke, G., Patel, P., & Chen, A. (2005). Methodology for Miscible Gas Injection EOR Screening. *All Days*. doi: 10.2118/97650-ms

Thomas, S. (2007). Enhanced Oil Recovery - An Overview. *Oil & Gas Science And Technology - Revue De L'ifp*, *63*(1), 9-19. doi: 10.2516/ogst:2007060

Treiber, L., & Owens, W. (1972). A Laboratory Evaluation of the Wettability of Fifty Oil-Producing Reservoirs. *Society Of Petroleum Engineers Journal*, *12*(06), 531-540. doi: 10.2118/3526-pa

Trevino, K., Shearer, J., McCurdy, P., Pease-Dodson, S., Okegbe, C., & Fisher, E. (2010). Isoelectric points of plasma-modified and aged silicon oxynitride surfaces measured using contact angle titrations. *Surface And Interface Analysis*, *43*(9), 1257-1270. doi: 10.1002/sia.3707

U.S. Energy Information Administration. Utica Shale Play Geology review. April 2017.

van Oss, C. (1993). Acid—base interfacial interactions in aqueous media. *Colloids And Surfaces A: Physicochemical And Engineering Aspects*, *78*, 1-49. doi: 10.1016/0927-7757(93)80308-2

Vander Wal, R. (2020). *Chps 1 & 2* [PDF] (pp. 3-4). Retrieved from https://psu.instructure.com/courses/2055188/pages/lecture-slides?module_item_id=30324642

Vidyadhar, A., Kumari, N., & Bhagat, R. (2012). Adsorption mechanism of mixed collector systems on hematite flotation. *Minerals Engineering*, *26*, 102-104. doi: 10.1016/j.mineng.2011.11.005

Villagrán Zaccardi, Y., Alderete, N., & De Belie, N. (2018). Lucas-Washburn vs Richards equation for the modelling of water absorption in cementitious materials. *MATEC Web Of Conferences*, *199*, 02019. doi: 10.1051/matecconf/201819902019

Virga, E., Spruijt, E., de Vos, W., & Biesheuvel, P. (2018). Wettability of Amphoteric Surfaces: The Effect of pH and Ionic Strength on Surface Ionization and Wetting. *Langmuir*, *34*(50), 15174-15180. doi: 10.1021/acs.langmuir.8b02875

Vishnyakov, V., Suleimanov, B., Salmanov, A., & Zeynalov, E. (2020). Oil recovery stages and methods. *Primer On Enhanced Oil Recovery*, 53-63. doi: 10.1016/b978-0-12-817632-0.00007-4

Wang, Y., Xu, H., Yu, W., Bai, B., Song, X., & Zhang, J. (2011). Surfactant induced reservoir wettability alteration: Recent theoretical and experimental advances in enhanced oil recovery. *Petroleum Science*, *8*(4), 463-476. doi: 10.1007/s12182-011-0164-7

Wang, Z., Chen, Y., Sun, X., Duddu, R., & Lin, S. (2018). Mechanism of pore wetting in membrane distillation with alcohol vs. surfactant. *Journal Of Membrane Science*, *559*, 183-195. doi: 10.1016/j.memsci.2018.04.045

Wasan, D., & Nikolov, A. (2003). Spreading of nanofluids on solids. *Nature*, *423*(6936), 156-159. doi: 10.1038/nature01591

Wei, B., Ning, J., He, J., Lu, L., Wang, Y., & Sun, L. (2018). Relation between brine-crude oil-quartz contact angle formed on flat quartz slides and in capillaries with brine composition:

Implications for low-salinity waterflooding. *Colloids And Surfaces A: Physicochemical And Engineering Aspects*, *555*, 660-667. doi: 10.1016/j.colsurfa.2018.07.051

Wenzel, R. (1936). RESISTANCE OF SOLID SURFACES TO WETTING BY WATER. *Industrial & Engineering Chemistry*, *28*(8), 988-994. doi: 10.1021/ie50320a024

Wiśniewska, M. (2010). The temperature effect on electrokinetic properties of the silica–polyvinyl alcohol (PVA) system. *Colloid And Polymer Science*, *289*(3), 341-344. doi: 10.1007/s00396-010-2341-4

Xie, P., Li, Y., Zhu, L., Shi, D., & Duan, X. (2016). Supplementary automatic generation control using controllable energy storage in electric vehicle battery swapping stations. *IET Generation, Transmission & Distribution*, *10*(4), 1107-1116. doi: 10.1049/iet-gtd.2015.0167

Xie, Q., Sari, A., Pu, W., Chen, Y., Brady, P., Al Maskari, N., & Saeedi, A. (2018). pH effect on wettability of oil/brine/carbonate system: Implications for low salinity water flooding. *Journal Of Petroleum Science And Engineering*, *168*, 419-425. doi: 10.1016/j.petrol.2018.05.015

Yang, S., Xie, B., Lu, Y., & Li, C. (2018). Role of magnesium-bearing silicates in the flotation of pyrite in the presence of serpentine slimes. *Powder Technology*, *332*, 1-7. doi: 10.1016/j.powtec.2018.03.049

Young, T. (1805). III. An essay on the cohesion of fluids. *Philosophical Transactions Of The Royal Society Of London*, *95*, 65-87. doi: 10.1098/rstl.1805.0005

Yuan, Y., & Lee, T. (2013). Contact Angle and Wetting Properties. *Surface Science Techniques*, 3-34. doi: 10.1007/978-3-642-34243-1_1

Yukselen-Aksoy, Y., & Kaya, A. (2010). A study of factors affecting on the zeta potential of kaolinite and quartz powder. *Environmental Earth Sciences*, *62*(4), 697-705. doi: 10.1007/s12665-010-0556-9

Zhang, Y., Zeng, J., Qiao, J., Feng, X., & Dong, Y. (2018). Investigating the Effect of the Temperature and Pressure on Wettability in Crude Oil–Brine–Rock Systems. *Energy & Fuels*, *32*(9), 9010-9019. doi: 10.1021/acs.energyfuels.8b01404

Zhou, X., Wei, X., Fedkin, M., Strass, K., & Lvov, S. (2003). Zetameter for microelectrophoresis studies of the oxide/water interface at temperatures up to 200°C. *Review Of Scientific Instruments*, *74*(4), 2501-2506. doi: 10.1063/1.1556957

Zhou, Y., Zhang, Y., Li, G., Wu, Y., & Jiang, T. (2015). A further study on adsorption interaction of humic acid on natural magnetite, hematite and quartz in iron ore pelletizing process: Effect of the solution pH value. *Powder Technology*, *271*, 155-166. doi: 10.1016/j.powtec.2014.10.045

Zienkiewicz-Strzałka, M., Deryło-Marczewska, A., & Kozakevych, R. (2018). Silica nanocomposites based on silver nanoparticles-functionalization and pH effect. *Applied Nanoscience*, *8*(7), 1649-1668. doi: 10.1007/s13204-018-0837-2